Dissertation

submitted to the

Combined Faculties of the Natural Sciences and Mathematics

of the Ruperto-Carola-University of Heidelberg. Germany

for the degree of

Doctor of Natural Sciences

Put forward by

Iwona Mochol

born in Bielsko-Biała, Poland

Oral examination: 7th November 2012

Nonlinear waves in Poynting-flux dominated outflows

Referees: Prof. John G. Kirk

Prof. Matthias Bartelmann

Abstract

Rotating, compact objects power some of the most spectacular phenomena in astrophysics, e.g., gamma-ray bursts, active galactic nuclei and pulsar winds. The energy is carried by Poynting flux, and the system is usually modelled using relativistic magnetohydrodynamics (MHD). However, in the relatively low density medium expected around some of these objects, the MHD approximation breaks down, allowing new, large-amplitude waves to propagate. We discuss the role of these waves in two astrophysical contexts:
In blazar jets, we show that a magnetic shear, launched together with a plasma from the black hole magnetosphere, begins to accelerate particles at a large distance from its source. The resulting non-thermal emission can, nevertheless, be modulated on very short timescales, which can explain the rapid variability of the TeV gamma-ray flux observed from some blazars.
In pulsar winds, we analyze the radial propagation of superluminal modes, including their damping by radiation reaction and by interaction with an external photon field. We discuss their effect on the structure of the pulsar wind termination shock, presenting new solutions in which the non-linear wave is asymptotically matched to the constant pressure surroundings. The observational implications of these solutions are discussed for both isolated pulsars, and pulsars in binary systems.

Zusammenfassung

Rotierende kompakte Objekte treiben einige der spektakulärsten Prozesse in der Astrophysik an, beispielsweise Gammastrahlenblitze, aktive Galaxienkerne oder Pulsarwinde. Der Energieaustausch wird durch elektromagnetische Felder („Poynting flux“) vermittelt und über relativistische Magnetohydrodynamik modelliert. Diese Beschreibung ist jedoch ungeeignet für ein Medium mit relativ geringer Dichte, welches um solche Objekte erwartet wird und in dem sich Wellen mit grosser Amplitude ausbreiten können. Die Rolle dieser Wellen wird in zwei astrophysikalischen Zusammenhängen diskutiert:
Erstens wird gezeigt, dass magnetische Scherwellen in Blazar Jets, welche zusammen mit Plasma aus der Magnetosphäre eines Schwarzen Loches erzeugt werden, in grossem Abstand zur Quelle Teilchen zu beschleunigen beginnen. Nichtsdestotrotz kann die resultierende nicht-thermische Emission auf sehr kurzen Zeitskalen moduliert werden, was die schnelle Änderung des TeV Gammastrahlenflusses erklärt, welche bei einigen Blazaren beobachtet wird.
Zweitens wird die radiale Ausbreitung von superluminalen Moden in Pulsarwinden analysiert, inklusive der Strahlungsdämpfung und Abschwächung durch Wechselwirkung mit einem externen Photonfeld. Der Effekt der Wellen auf die Struktur des Terminationshocks eines Pulsarwindes wird diskutiert und neue Lösungen präsentiert, in denen die nichtlineare Welle an die Umgebung mit konstanten Druck asymptotisch angepasst wird. Die Implikationen für Beobachtungen dieser Lösungen werden sowohl für isolierte Pulsare, als auch für Pulsare in binären Systemen diskutiert.

To my parents, and Gosia

Contents

List of Figures

Part I

Chapter 1

Introduction

The mechanism underlying the most energetic phenomena in the Universe is thought to be the extraction of the rotational energy of a central, compact object by a relativistic outflowing wind. The energy transfer is mediated by the electromagnetic fields that are launched together with a plasma, and, presumably, are responsible for the outflow collimation and acceleration of the particles that radiate nonthermal photons.

Theoretical and numerical investigations suggest that such an outflowing wind is rather dense close to the central object, since the magnetospheres around rapidly spinning neutron stars or black holes are prone to avalanche pair production processes. The electromagnetic cascades are started by primary particles, ripped out of the stellar surface or supplied by the accretion flow around a black hole, and are sustained by the radiation these particles emit when accelerating in the curved, extremely strong magnetic fields in the magnetosphere. Even though the created plasma has a density high enough to screen out any electric field component along the magnetic field lines, the particles are thought to contribute mainly through their charges and currents they carry, and not through their inertia. This view is motivated by the fact that close to the compact object the magnetic field dominates the energetics in the wind. The absence of an electric field in the proper plasma frame validates the use of equations of relativistic magnetohydrodynamics (MHD), which, in the limit of vanishing particle mass, is referred to as force-free electrodynamics (FFE) [75].

This approach breaks down when the wind propagates to large distances. In radial expansion, the particle density, and thus the conduction current, drops as $1/r^2$ with radius, but the toroidal component of the field diminishes more slowly, as $1/r$. As a consequence, there exists a critical distance beyond which the flow becomes charge-starved [200, 151]. To increase the current the particles accelerate, but the relativistic drift-speed implies that the particle inertia becomes dynamically important, i.e., it begins to affect the plasma conductivity. In this case, a more general description of a plasma is needed than that of ideal MHD. The simplest such model that connects the current to the inertia of the plasma constituents is that of two cold fluids. A big advantage of this model is its ability to describe the propagation of electromagnetic or Alfvén waves of large amplitudes [140, 142, 43, 93], a property highly desirable in astrophysical contexts [17, 97, 10], since the outflows from the rotating, magnetized objects are thought to propagate outwards as waves. In black hole jets that emerge in the polar regions they resemble magnetic twists, whereas in the pulsar case the equatorial striped wind is described as an entropy wave. Their fully nonlinear description, beyond the MHD approximation, is therefore an important next step towards understanding the nature and the properties of the Poynting-flux dominated outflows.

In the following we take a closer look at two relevant astrophysical environments, in which propagation of the nonlinear waves can be manifested: blazars and pulsars.

1.1 Blazars

Active galactic nuclei (AGN) are among the most spectacular objects in the Universe. About 10% of them are classified as radio-loud, and these launch large-scale outflows that are observed as collimated jets. The enormous energy which they carry is thought to be stored in an electromagnetic field, and gradually (or impulsively) released to a plasma as it propagates outwards to large distances. The energy supply is provided by a powerful engine, which is thought to be a central compact object, maintaining the overall source activity by accretion of material from its host galaxy. This supermassive (typically $10^6 - 10^{9.5}\mathrm{M}_\odot$) nucleus is almost certainly a black hole, a picture strongly supported by the observations of the Milky Way center.[1]

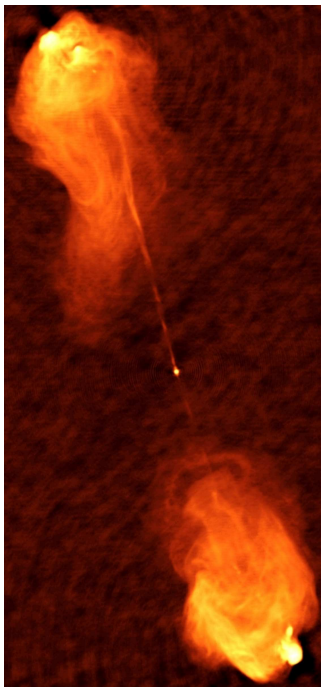

Figure 1.1: Collimated jets from Cygnus A. Image courtesy of NRAO AUI (1.4 GHz).

One of the most intriguing open questions is the bimodality of radio-loud AGNs. Outflows from the most powerful sources are extremely well collimated, they can extend up to megaparsecs, and finally terminate in extended lobes with bright "hot spots"(see Fig. 1.1). Jets from less powerful ones usually exhibit more complex structure, they are laterally wider, less collimated, with visible edge-darkening, i.e., gradual fading away with the distance from the central source to end "nowhere" (see Fig. 1.2).

The underlying cause of these differences is not clear, but two kinds of models are proposed: "extrinsic" ones associate it with the environment in which a jet propagates; the "intrinsic" models point rather to the distinct jet formation processes or different properties of the driving source (e.g., [186]). In the latter case, it was suggested that the spin of a central black hole may play a role, being close to the maximal for the most powerful sources [30, 207]. However, the X-ray observations of iron emission lines, which are used to constrain the last stable orbit in the disk around rotating black holes, indicate that at least some radio-quiet sources may harbor very rapidly spinning holes $a > 0.94$, thus the "spin paradigm" may not hold for all the objects[2], or something else may be there. A more global picture of radio-loudness, with the question why some sources launch the jets at all, whereas other do not, points toward the accretion mode, so that the combination of both the spin and the disc effects may play a role [183]. In particular, at high accretion rates, the ability of an outflow to collimate has been questioned [183], and at lower accretion rates different kinds of flows onto the center have been proposed: radiatively efficient in quasar-mode, and advection dominated (ADAF) in radio-mode, for powerful and less energetic sources, respectively [24]. Fast rotation, however, seems to be a necessary condition for launching of a jet.

In AGNs two energy sources to power the outflows are thought to play a role: liberation of gravitational energy of an accretion disk [131, 29, 31], or electromagnetic extraction of the

[1] The most compelling argument was given by [181], who used high-resolution infrared imaging to track the proper motion of the stars in the very center of the Milky Way. Kepler's law has been measured there down to 17 light hours, which corresponds to the distance 1.8×10^{15} cm, and the unseen central object's mass determined from the pericenter of the closest orbit is $3.7 \times 10^6 \mathrm{M}_\odot$, which implies the gravitational radius $r_\mathrm{g} = 5.5 \times 10^{11}$ cm. This, even though it does not confirm the existence of a central black hole with certainty, excludes on a high confidence level the possibility of a cluster of astrophysical objects, and most of the more exotic models, such as that of massive, degenerate fermions.

[2] It should be mentioned, however, that this method of measuring spins suffers from some subtleties and uncertainties. The most serious one is the underlying assumption that the reflection of the coronal X-rays by disk material does not occur within the plunging region between the black hole horizon and the last stable orbit. In the case of MCG-6-30-15, for which this high spin was determined, a slowly spinning black hole hypothesis would require extreme conditions and seems rather improbable (see exhaustive review by [175]).

rotational energy of a Kerr black hole (Blandford-Znajek mechanism) [32]. The physics of the extraction process can be very different in each case, and is manifested in distinct outflow features.

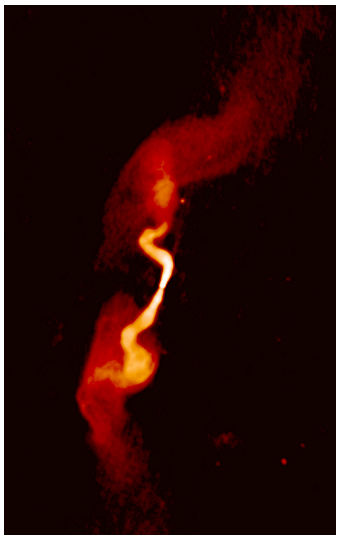

Figure 1.2: Radio Galaxy 3C31 with edge-darkened jets. Image courtesy of NRAO AUI.

In unified models, jets have both components: the one originating in the disk and the other launched in the black hole magnetosphere. The latter is a fast, highly Poynting-flux dominated core, and the former is a slower, heavier matter-loaded and more dissipative sheath [185, 39]. The model of two-composite (stratified) jets is consistent with general relativistic MHD simulations of an accreting, rotating black hole. The time evolution of the system reveals the formation of a low density funnel along the rotational axis, in which a highly ordered magnetic field topology is established. Accreting matter does not penetrate into this region, so the mass-loading of the funnel is determined only by the pair production rate in the black hole magnetosphere. The outer layer of the jet, on the other hand, is the disk driven wind, loaded by the accreting matter. If both mechanisms work simultaneously, then, depending on the physical conditions in the source, one of them can be dominant. It was proposed that if accretion proceeds in the ADAF regime, the source luminosity can be largely due to the BZ process [11], which can easily account for the power output of the low and medium strength radio sources [67]. In the opposite case, a radiatively efficient disk allows for disk-driven and/or rotation driven outflows [130].

In both disk and magnetospheric launching mechanisms a special role is played by the magnetic field, supported externally by an accretion flow. In fact, the field is thought to have importance not only in launching, but also in accelerating and collimating the outflowing plasma beam. This field, frozen into the disk or magnetospheric plasma, is thought to be dragged by its rotation, so that it becomes twisted and this twist propagates outwards as a jet. The energy extracted by electromagnetic fields, and carried by the Poynting flux in a wound magnetic field, is deposited in relativistic particles that radiate in synchrotron and inverse Compton processes. Emission is observed along the large-scale jets, across the entire electromagnetic spectrum, often with the dominant component in the very high energy (VHE) range.

Blazars constitute one class of AGN. Their name is a collective term for BL Lac objects and Flat Spectrum Radio Quasars (FSRQ). These objects exhibit broad-band variability, and high polarization. The non-thermal continuum is featureless in BL Lacs, but in the case of FSRQ reveals broad emission lines in the optical band, e.g., [202]. In a unification scheme, blazars are radio-loud AGNs with a visible outflow directed close to the line of sight of an observer, so that we actually look down the jet. In this case the emission becomes significantly Doppler beamed. This affects not only the luminosity, but also the spectral characteristics of their radiation. This is what makes blazars so special – their spectra are completely dominated by the jet contribution, both synchrotron and inverse Compton. The most energetic, jet phenomena can, therefore, be directly probed by emission measurements. BL Lacs are likely to operate in the ADAF regime, and in unification models are associated with low-luminosity radio galaxies. Quasars are their powerful counterparts, working in a radiatively efficient regime of accretion. Since jets are unlikely to be homogeneous, stationary flows, the outlined unification scheme can potentially explain blazar variability on intraday scales. Really puzzling, however, are fluctuations of TeV γ-ray fluxes, exhibited by some sources. The timescale on which the emission changes, as revealed by observations of HESS and MAGIC, can be as short as few minutes [3, 5, 6], which is much less than the light crossing time of the event horizon of the central black hole (around an hour). The amplitude of these fluctuations is large, a factor of a few in comparison to the steady flux.

Neither the mechanism of emission, nor the location of the emitting region is known, but it is likely to occur far from the central object, so that the VHE photons can escape unattenuated by $\gamma\gamma$ scattering on the soft photons from the disk, torus and broad line region (BLR). Alternatively, small-scale structures that modulate the emission can be imprinted on the jet as it launched close to the black hole, and further transported to large distances, where they show up.

Disk-driven jets are often modelled using an MHD description. However, in the low-density medium that is expected in the aforementioned, inner-jet funnel around the rotational axis, ideal MHD models break down and non-ideal MHD effects are likely to intervene. In particular, particle inertia becomes dynamically important. As a consequence, initially frozen-in fields, launched with a bunch of particles created in the magnetosphere, cannot maintain a steady flow and try to release themselves from the charge-starving plasma. This leads to the acceleration phase of the jet at large distance from the central source. The magnetic twist enters a nonlinear regime, and this is where the fully nonlinear analysis is required to understand the evolution of the system. In particular, it opens the way to investigation of new phenomena, that are not included within standard approaches, but may explain ultra-fast, large-amplitude variability of blazar emission.

1.2 Pulsars

Pulsars (pulsating radio sources) are rapidly spinning neutron stars. They owe their name to their characteristic lightcurves, exhibiting pulses of emission in very accurate time intervals that are attributed to the rotational periods. The pulsating signal is attributed to the "lighthouse effect", a beam of radiation inclined to the rotational axis, that sweeps the observer's field of view once (or twice) every period. However, an explanation how this beam is created turned out to be much more difficult to find than an explanation how it is observed. Many complex phenomena are involved in an underlying emission mechanism, which makes it hard to model and now, 45 years after their discovery, it is still not understood how pulsars shine. In radio frequencies the pulses exhibit finer structure, like subpulses and microstructures, superimposed on the main peaks; every object has a unique lightcurve, sometimes exhibiting nulling (disappearance of pulsations for a specific time) or periodic drifting of subpulses through the pulse.

Pulsar periods, known from measurements of the pulsating signal, increase extremely slowly. For the Crab pulsar, the implied loss of rotational energy is $\sim 10^{38}$ erg s^{-1}. However, the radio luminosity in its pulses is $\sim 10^{30}$ erg s^{-1}, only a small fraction of this power, implying that different mechanisms are responsible for the radio emission and the slow-down of a pulsar. The latter is attributed to the large-amplitude electromagnetic radiation of a rotating – as often assumed – magnetic dipole. One of the first models of pulsar emission was that of an orthogonal rotator [76], based on the fact that a magnetic dipole rotating in a vacuum losses its rotational energy due to magnetic dipole radiation if the rotation and magnetic axes are misaligned. This radiation is emitted beyond the light cylinder distance $r_L = c/\omega$, where the corotation velocity exceeds the speed of light. Beyond the light cylinder information about a change in the field configuration arrives with retardation and an electromagnetic wave is emitted to adjust the far-field region to the changes. However, if the pulsar surroundings were vacuum, a huge electric field acting on the star surface would be generated in analogy to a unipolar inductor. It was quickly realized that this field would accelerate particles from the stellar surface and lead to cascade pair production and, in turn, to a plasma-filled magnetosphere (see Sect. 5.1 for details). Thus, large-amplitude electromagnetic radiation propagating in a plasma is in fact a wave, a mixture of fields and particles.

Such a wave can be quantified by its strength parameter. It expresses the ability of a vacuum, electromagnetic wave to accelerate particles, i.e., it is the Lorentz factor that a particle would gain if it was accelerated in the wave fields in one wavelength, $a = eE\lambda/mc^2$. For a general

(nonvacuum) wave one can define it in analogy, and express it in terms of the total luminosity of the source that would be carried by the wave at the light cylinder, $a = (e^2L/m^2c^5)^{1/2} = 3.4 \times 10^{10} L_{38}^{1/2}$, where L_{38} is the isotropic source luminosity in units 10^{38} erg/s (for details see Sect. 5.2.2). For pulsars this implies $a \sim 10^{10}$ at the light cylinder, for blazars $a \sim 10^{14}$ at one gravitational radius of a supermassive black hole of mass $10^9 M_\odot$. The strength parameter expresses also the ratio of the particle Larmor frequency to the wave frequency. It is clear that any outflow originating from such conditions is extremely Poynting-flux dominated, and the waves that potentially are launched in these environments are very strong. For comparison, the next generation of laser facilities on the earth will reach $a \sim 10^2 - 10^4$ [54].

Inside the light cylinder, in the near-zone close to the stellar surface, the field is much stronger. If during the supernova collapse the angular momentum of a star and the poloidal magnetic flux are conserved, the resulting neutron star can rotate with frequency 10^3 Hz and would have a magnetic field of enormous magnitude, of the order 10^{12} G near the surface [92]. The fastest, millisecond pulsars must have slightly weaker fields, up to 10^9 G (if their fields were stronger, the spin-down due to dipole radiation would be too rapid). Magnetars, on the other hand, have a field which can exceed the Schwinger critical magnetic field $B_{cr} = m^2c^3/e\hbar = 4.4 \times 10^{13}$ G. In such an extreme field, exotic processes become possible: transitions between Landau quantized states and resonant Compton scattering, magnetic one-photon decay resulting from nonconservation of perpendicular momentum, spin-dependent phenomena [78]. In the spectra of X-ray and γ-ray pulsars, direct measurements of cyclotron absorption lines, generated when particles change their Landau states, confirm the strength of the field to be indeed of the order of a few $\times 10^{12}$ G. For comparison, the strongest magnetic fields generated in the laboratory reach 45 T (hybrid magnet in the National High Magnetic Field Laboratory, Florida). Stronger fields for fusion purposes, were obtained by magnetic-flux compression using laser beams and reached 30-40 MG (Omega facility) [72][3].

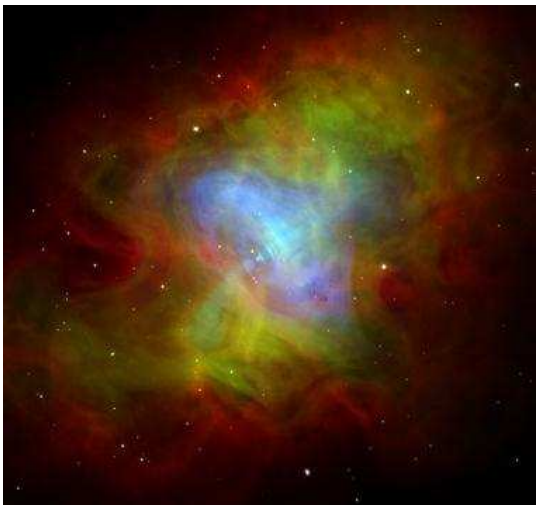

Figure 1.3: Crab pulsar (central point) and nebula, and darker regions in between. Red: radio, green: visible, blue: X-ray. Credit: J. Hester (ASU), CXC, HST, NRAO, NSF, NASA.

The energy stored in superstrong electromagnetic fields, when released, can lead to very violent and complex phenomena, from which many are still not understood. In recent years a big puzzle related to the violent release of energy, and conversion of this energy into radiation, is the γ-ray flaring observed from Crab. The three bright flares above 100 MeV were observed by AGILE and Fermi-LAT between 2007 and 2010 [1, 194]. During the flare an unpulsed high-energy flux was enhanced by a factor of ≈ 10 in $\sim$12h, but the pulsed emission and pulsar period were stable. In April 2011 Fermi reported a fourth flare, where the flux was enhanced by a factor ~ 30 [37]. The isotropic luminosity at the peak was about 1% of the total spin down power of the pulsar. However, the angular resolution of current gamma-ray telescopes is not sufficient to specify the location of the flaring region.

A pulsar itself, in optical and X-rays is a point-like source, well resolved from the nebular emission, embedded in a dark region that extends between the pulsar and the nebula. This dark region is at-

[3]For research purposes, however, it is expected that in the near future "artificial" fields will be accessible, strong enough to simulate in laser-irradiated optical lattices some quantum processes unique for the strong-field regime, such as quantum Hall effect, which may be of importance for quantum computing, e.g., [154].

tributed to the relativistically moving, cold pulsar wind. The emission site of the synchrotron optical and X-rays cannot be determined unambiguously: in some models, photons are produced in the pulsar's inner magnetosphere, and an alternative scenario is that the emission originates from the pulsar wind itself, which – if the wind is ultrarelativistic – would also appear as pulsed and point-like [100]. Emission from the wind is attributed to the radiation processes in the alternating magnetic field, frozen into, and transported outwards with the plasma. However, since its density decreases with the distance as the wind propagates, at sufficiently large radius, charge starvation allows the displacement current to take over, and the propagation of electromagnetic, relativistically strong waves becomes possible. This is a different scenario than that in blazars. In general, pulsar winds can be less magnetized than blazar jets, because pulsar cascades are thought to have higher multiplicities. In this case, before charge-starvation changes the behavior of the MHD wave, a conversion to the newly allowed electromagnetic modes is possible. Such an electromagnetic wave can be regarded as a transition layer between the striped, MHD wind and the surroundings. It arises in a confined flow, whose structure is determined by both inner and outer boundary conditions. The latter are specified by the properties of the external medium, which let us think of a conversion process as being a consequence of the boundary conditions, imposed by the surroundings. Thus, in pulsar environments nonlinear waves can be manifested as precursors to termination shocks. This possibility of conversion of an MHD wind to an electromagnetic wave is very attractive, because it may solve one of the puzzles posed by pulsar winds: it provides a way to transfer an enormous amount of energy stored in the electromagnetic fields to the particles, a process that cannot be explained within ideal MHD [146, 97, 10]. Thus, in pulsar environments nonlinear waves can be manifested as precursors, and whenever their launching is possible, they can provide a generic solution to the problem of conversion of energy from the Poynting flux to the particles.

1.3 Structure of the thesis

The thesis contains three parts:

Part I, which includes this Chapter, is introductory. It continues with *Chapter 2*, in which we first discuss nonlinear Thomson scattering of a test particle by a strong electromagnetic wave. Then we focus on self-consistent, nonlinear waves propagating in cold pair plasmas. Two modes are of interest: large-amplitude Alfvén wave with subluminal phase velocity $\beta < 1$, and strong electromagnetic waves with superluminal phase speed $\beta > 1$, but subluminal group speed $\beta_* = 1/\beta < 1$. In the superluminal mode synchro-Compton radiation is emitted by accelerated particles, and we review the physics of radiation reaction in this case.

Part II is focused on nonlinear waves in Poynting-flux dominated jets, launched from the black hole magnetospheres.

Chapter 3. We review the electrodynamics of rotating black holes, immersed in an externally supported magnetic field. We derive equations of particle/cold fluid motion, and Maxwell equations in a frame of physical, locally nonrotating observers, that have vanishing angular momentum with respect to a central black hole, but move with respect to the distant stars. We discuss models of launching, collimation and acceleration of Poynting-flux dominated jets, and recent observations of very rapid variability of γ-ray TeV flux from some blazars, which are difficult to accommodate in standard approaches.

Chapter 4. We present our model that can account for the observed fluctuations of blazar VHE emission. In it, the short-scale modulations are associated with the wavelength of a nonlinear

Alfvén-like mode which propagates in the direction of the jet, and modulates the particle emission with the frequency of the wave. This chapter is based on work published in the Astrophys. J. [101].

Part III is dedicated to strong waves in magnetized pulsar winds.

Chapter 5. We review the physics of pulsar magnetospheres, from where relativistic winds are launched, and also the properties and propagation characteristics of these winds. We emphasize the "σ-problem", the failure of an ideal MHD wind to transfer Poynting flux into particle energy flux before reaching the termination shock. A solution for this problem must go beyond the MHD description and this provides a motivation for the investigation of strong electromagnetic waves as shock precursors.

Chapter 6. We present our contribution to the modelling of pulsar wind termination shocks. In particular, we investigate the radial evolution of electromagnetic waves that are launched from the MHD pulsar wind, and we show that there exists a unique, self-consistent solution that can be matched to the external pressure. We investigate how this solution is affected by radiation damping, and we discuss the formation of shocks for both isolated pulsars and those in binary systems.

Chapter 2

Beyond MHD: nonlinear waves in plasmas

In black hole and pulsar environments electromagnetic waves can propagate with large amplitudes. To understand the underlying physics and the behavior of plasma constituents when the strong fields are applied, we start from a test particle approach in Sect. 2.1, where we describe particle trajectories in a vacuum strong wave. Further we consider an exact, self-consistent solution of the nonlinear plasma-wave system. A general, two-fluid description of a plasma coupled to the electromagnetic fields via Maxwell's equations, is shown in Sect. 2.2, where we also discuss some special solutions of these equations: the subluminal mode that describes a magnetic shear, and the superluminal mode that resembles more an electromagnetic wave. We also make a few remarks on the linearized theory, to explain better how the superluminal phase velocity arises in a plasma medium, and how it is related to the subluminal group velocity of the wave. At the end, Sect. 2.3, we summarize radiation processes that are of relevance for superluminal, strong modes.

In our convention, throughout the thesis, the metric has a signature +2.

2.1 Motion of a particle in an electromagnetic wave

In the nonrelativistic physics interaction of a particle with an incident electromagnetic wave is treated within the framework of Thomson scattering. However, when the wave is strong, it imparts relativistic velocity on the particle, so that in every frame the particle becomes relativistic at some point of its periodic trajectory, leading to the nonlinear regime of the scattering. We discuss this regime in the following section.

Equations of motion

The equations of motion of a particle with charge e, mass m, momentum $p = mc(\gamma, u^i)$ and 4-velocity $u = \gamma(1, \boldsymbol{v}/c)$, in an external electromagnetic field $F^{\mu\nu}$ are given by

$$\frac{dp^\alpha}{d\tau} = eF^{\alpha\beta}u_\beta \tag{2.1}$$

or equivalently

$$mc\frac{d\gamma}{d\tau} = e\,\boldsymbol{u}\cdot\boldsymbol{E}\ , \tag{2.2}$$

$$mc\frac{d\boldsymbol{u}}{d\tau} = e\,(\gamma\boldsymbol{E} + \boldsymbol{u}\times\boldsymbol{B}) \tag{2.3}$$

where $\gamma d\tau = dt$. In the nonrelativistic limit $v \ll c$ the contribution from the magnetic part of the force is much smaller than that from the electric force. As we want to investigate the interaction

of particles with strong waves, which are able to accelerate them to relativistic velocities, we consider the full dynamics, following Gunn & Ostriker [77]. Consider a monochromatic plane wave moving in an arbitrary direction $\hat{\boldsymbol{k}}$, $|\hat{\boldsymbol{k}}| = 1$. Without loss of generality we can choose this direction to be x. The electric and magnetic fields have equal magnitude, they are mutually orthogonal, and they oscillate in the plane perpendicular to the direction of motion $\boldsymbol{B} = \hat{\boldsymbol{k}} \times \boldsymbol{E}$. Hence

$$\boldsymbol{u} \times \boldsymbol{B} = \boldsymbol{u} \times \left(\hat{\boldsymbol{k}} \times \boldsymbol{E}\right) = (\boldsymbol{u} \cdot \boldsymbol{E})\, \hat{\boldsymbol{k}} - (\boldsymbol{u} \cdot \hat{\boldsymbol{k}})\, \boldsymbol{E} \tag{2.4}$$

and the parallel component of (2.3) immediately gives

$$mc \frac{du_x}{d\tau} = e\, \boldsymbol{u} \cdot \boldsymbol{E} \tag{2.5}$$

From (2.2) and (2.5)

$$\frac{d}{d\tau}(\gamma - u_x) = 0 \qquad \Rightarrow \qquad \gamma - u_x = \alpha \tag{2.6}$$

where α denotes a constant of motion. From (2.3) and (2.4) we also get

$$\frac{1}{\alpha\omega} \frac{d\boldsymbol{u}_\perp}{d\tau} = \frac{e\boldsymbol{E}}{mc\omega} \tag{2.7}$$

Since for a moving plane wave all the quantities are functions of only one variable $\phi = x_\mu k^\mu = \omega t - kx = \omega(t - x/c)$, we can express the time and space derivatives in terms of it

$$\frac{\partial}{\partial t} = \omega \frac{d}{d\phi}, \qquad \frac{\partial}{\partial x} = -k \frac{d}{d\phi} = -\frac{\omega}{c} \frac{d}{d\phi}, \qquad \gamma \frac{d}{dt} = \omega\,(\gamma - u_x)\, \frac{d}{d\phi} = \omega\alpha \frac{d}{d\phi} \tag{2.8}$$

Then

$$\boldsymbol{u}_\perp = \boldsymbol{u}_{\perp \boldsymbol{0}} + \int_0^\phi d\phi'\, \frac{e\boldsymbol{E}(\phi')}{mc\omega} \tag{2.9}$$

Linear polarization

Assume that the particle is initially at rest. In the special case of a linear polarization we can choose

$$\boldsymbol{E} = E_0 \cos\phi\, \hat{\boldsymbol{y}} \tag{2.10}$$

From (2.9)

$$u_y = a \sin\phi \tag{2.11}$$

$$u_z = 0 \tag{2.12}$$

and the equations for the parallel component of velocity and the Lorentz factor give

$$\frac{du_x}{d\phi} = \frac{d\gamma}{d\phi} = \frac{a^2}{\alpha} \sin\phi \cos\phi \tag{2.13}$$

The solution is straightforward and given by

$$u_x = \frac{a^2}{2} \sin^2\phi \tag{2.14}$$

$$\gamma = 1 + \frac{a^2}{2} \sin^2\phi \tag{2.15}$$

Here we also introduced the wave strength parameter

$$a = \frac{eE_0}{mc\omega} \tag{2.16}$$

In the nonrelativistic limit $a \ll 1$ the motion in x direction is negligible, given by the second order expression in a small parameter a. The charge oscillates in the plane perpendicular to the direction of wave motion. The oscillation velocity is nonrelativistic, hence the magnetic force on the charge is negligible. The situation changes dramatically when $a \gg 1$. The particle achieves relativistic perpendicular velocity in half the wave period and the magnetic force influences the motion. It bends the particle trajectory in the direction of the wave propagation, resulting in a non-planar motion. It can be decomposed into the "figure-eight" motion and a uniform translation in the x-direction. The solution in the "guiding center" frame, in which the phase-averaged parallel velocity of the particle vanishes, is found from (2.13) with the condition $\langle u_x \rangle = 0$, which determines the constant of integration. This gives

$$u_y = a \sin\phi \tag{2.17}$$

$$u_x = -\frac{a^2}{4\sqrt{1+\frac{1}{2}a^2}} \cos 2\phi \tag{2.18}$$

$$\langle \gamma \rangle = \sqrt{1+\frac{a^2}{2}} \tag{2.19}$$

Circular polarization

When the wave is circularly polarized

$$\boldsymbol{E} = E_0 \sin\phi\, \hat{\boldsymbol{y}} + E_0 \cos\phi\, \hat{\boldsymbol{z}} \tag{2.20}$$

and $\boldsymbol{u}\cdot\boldsymbol{E} = 0$. In the guiding center frame the condition $\langle u_x \rangle = 0$ implies $u_x = 0$ and $\gamma = \sqrt{1+a^2}$. Since the amplitude of the parallel motion vanishes, the particle moves entirely in the plane perpendicular to the direction of the wave propagation. The trajectory is a circular helix, as in the case of a uniform magnetic field.

2.2 Large-amplitude waves in cold pair plasmas

The electromagnetic structure of a wave propagating in a vacuum is supported by displacement currents; in a plasma, also the conduction current contributes. The simplest model that captures the physics connected with the finite inertia of the charge-carriers is that of two cold, oppositely charged fluids – in particular, here these are the electron and the positron ones, denoted by suffices "$-$" and "$+$". The method of solving self-consistently two-fluid and Maxwell's equations in the case of large wave amplitudes was introduced by Akhiezer & Polovin [4], and used by Max & Perkins [140], Max [142], Clemmow [42], Kennel & Pellat [93].

Since the fluids are cold, their equations of motion are the same as the 1-particle Eq. 2.1, but 4-velocity is now that of the fluid.

Here we change the notation: for waves in a plasma p^α formally will denote the 4-velocity of the fluid (i.e., the momentum normalized to mc). The fluid equations of motion take a form

$$mc\frac{d\gamma}{d\tau} = e\,\boldsymbol{p}\cdot\boldsymbol{E} \tag{2.21}$$

$$mc\frac{d\boldsymbol{p}}{d\tau} = e\,(\gamma\boldsymbol{E} + \boldsymbol{p}\times\boldsymbol{B}) \tag{2.22}$$

They are complemented by the continuity equation for each fluid

$$\frac{\partial}{\partial t}\rho + \nabla\cdot\boldsymbol{j} = 0 \tag{2.23}$$

and by Maxwell equations, which govern the propagation of light waves in a medium

$$\nabla \cdot \boldsymbol{E} = 4\pi\rho \tag{2.24}$$

$$\nabla \cdot \boldsymbol{B} = 0 \tag{2.25}$$

$$\nabla \times \boldsymbol{E} = -\frac{1}{c}\frac{\partial \boldsymbol{B}}{\partial t} \tag{2.26}$$

$$\nabla \times \boldsymbol{B} = \frac{4\pi}{c}\boldsymbol{j} + \frac{1}{c}\frac{\partial \boldsymbol{E}}{\partial t} \tag{2.27}$$

where

$$\rho = e(n_+\gamma_+ - n_-\gamma_-) \tag{2.28}$$

$$\boldsymbol{j} = ec(n_+\boldsymbol{p}_+ - n_-\boldsymbol{p}_-) \tag{2.29}$$

As in the previous section, we consider a plane wave moving in the x direction with phase velocity $v = c\beta$. Changing the time and space variables to the phase ϕ, which now is

$$\phi = \omega\left(t - \frac{x}{c\beta}\right) \ , \tag{2.30}$$

we can express their derivatives by

$$\frac{\partial}{\partial t} = \omega\frac{d}{d\phi} \qquad \frac{\partial}{\partial x} = -\frac{\omega}{c\beta}\frac{d}{d\phi} \qquad \gamma\frac{d}{dt} = \omega\left(\gamma - \frac{p_x}{\beta}\right)\frac{d}{d\phi} = \omega\Delta\frac{d}{d\phi} \tag{2.31}$$

Here we introduced

$$\Delta = \gamma - p_x/\beta \tag{2.32}$$

When $\Delta = 0$ the particles move with the wave phase speed in the direction of propagation. This case is possible only for the subluminal mode. The equations of motion are

$$\Delta\frac{d\gamma}{d\phi} = \boldsymbol{p} \cdot \boldsymbol{\nu} \tag{2.33}$$

$$\Delta\frac{d\boldsymbol{p}}{d\phi} = \gamma\boldsymbol{\nu} + (\boldsymbol{p} \times \boldsymbol{\Omega}) \tag{2.34}$$

where $\boldsymbol{\nu} = e\boldsymbol{E}/mc\omega$ is a normalized electric field, and $\boldsymbol{\Omega} = e\boldsymbol{B}/mc\omega$ is a normalized magnetic field. From the continuity equation one gets

$$\frac{d}{d\phi}(n\Delta) = 0 \tag{2.35}$$

and from (2.25) and the x component of (2.26)

$$\frac{d}{d\phi}\Omega_x = 0 \tag{2.36}$$

Expressing transverse fields as $E = E_y + iE_z$, $B = B_y + iB_y$, and transverse velocity as $p_\perp = p_y + ip_z$, one obtains Faraday's law in a form

$$\frac{d}{d\phi}\left(\Omega - i\frac{\nu}{\beta}\right) = 0 \tag{2.37}$$

and Ampère's law

$$\frac{d}{d\phi}\left(\nu + i\frac{\Omega}{\beta}\right) + \frac{\omega_\mathrm{p}^2}{\omega^2}p_\perp = 0 \tag{2.38}$$

where we used $\boldsymbol{j} = 2enc\boldsymbol{p}$. In a cold pair plasma neutrality $\rho = 0$ implies $n_+\gamma_+ = n_-\gamma_-$. The waves are purely transverse, since (2.24) implies vanishing of the longitudinal component of an electric field $\nu_x = 0$, and therefore, vanishing of the longitudinal current $j_x = 0$. From (2.28) being 0, and from (2.29), one gets $\boldsymbol{p}_{\perp+} = -\boldsymbol{p}_{\perp-}$, or $p_{y+} = p_{y-}$ and $p_{z+} = -p_{z-}$ (or the other way round). Since both particle species have the same dynamics, the equations can be solved for only one of them, say the positron fluid, and a solution for electrons can be obtained by analogy.

In our notation equations of motion take a form

$$\Delta\frac{d\gamma}{d\phi} = \mathrm{Re}\,(p_\perp\nu^*) \tag{2.39}$$

$$\Delta\frac{dp_\parallel}{d\phi} = -\mathrm{Im}\,(p_\perp\Omega^*) \tag{2.40}$$

$$\Delta\frac{dp_\perp}{d\phi} = -i\Delta\Omega\beta - i\Omega_x p_\perp \tag{2.41}$$

2.2.1 Special frames

The Lorentz transformation of variables t and x from the laboratory frame to that moving with 4-velocity U, parallel to the wave velocity, leads to the transformed phase variable [42, 93]

$$\phi = \omega\left[t'\left(\Gamma - c\frac{U}{\beta}\right) + \frac{x'}{c}\left(U - \frac{\Gamma}{\beta}\right)\right] \tag{2.42}$$

Faraday's law (2.37) takes a form [93]

$$\frac{d}{d\phi}\left[\Omega'\left(\Gamma - \frac{U}{\beta}\right) + i\nu'\left(U - \frac{\Gamma}{\beta}\right)\right] = 0 \tag{2.43}$$

When phase velocity β is subluminal, one can choose $U = \Gamma\beta$. In a frame moving with this speed, the phase variable is purely spatial, and (2.43) implies that the electric field in this frame is constant.

When phase speed β is superluminal, a convenient choice is $U = \Gamma/\beta$, which defines the frame moving with the speed $c/\beta = c\beta_*$. The phase ϕ becomes just a time variable and all the spatial dependence vanishes. (2.43) implies that the magnetic field in the special frame is constant. To keep the analysis tractable analytically, we choose this constants to be 0, i.e., there is no phase-averaged magnetic field in the special frame of the superluminal mode. In pulsars it is justified in the equatorial plane of a rotating neutron star, where the alternating magnetic field in a striped wind changes polarity every half a wavelength – thus, over one phase period, it averages to 0. For higher latitudes, the averaged field does not vanish and a more general, numerical treatment is needed.

2.2.2 Subluminal mode: magnetic shear

Let us outline here the solution discussed by Clemmow [42]. (2.36) implies that $\Omega_x = \mathrm{const}$. Clemmow derives a general solution for $\Omega_x = \Omega_0$, and in this case the nontrivial solutions have $\Delta \neq 0$. In both pulsar and black hole cases, the radial magnetic field drops as r^{-2} with the distance, hence far from the object $\Omega_0 \to 0$, and a solution has $\Delta = 0$. This condition implies that the particles move in resonance with the wave, i.e., $p_\parallel = \gamma\beta$. In a frame moving with this speed Faraday's law (2.43) implies that the electric field is constant and special solution can be found with this constant being 0 (this corresponds to the vanishing phase average of the field). In this case equations of motion imply that the particle energy is constant and thus also $p_\parallel$ is constant. The continuity equation (2.35) is trivially satisfied for any dependence of n on ϕ, but

further we take the simplest solution with the proper density independent of the phase $n = \text{const}$. Substitution of $p_\perp$ from Ampère's law

$$\frac{d\Omega}{d\phi} = i\beta\gamma_\mathrm{w}^2 \frac{\omega_\mathrm{p}^2}{\omega^2} p_\perp \tag{2.44}$$

to (2.40) implies that the magnetic field has constant magnitude

$$0 = \mathrm{Im}\left(p_\perp \Omega^*\right) = -\frac{\omega^2}{\omega_\mathrm{p}^2}\frac{1}{\beta\gamma_\mathrm{w}^2}\left(\frac{d\Omega}{d\phi}\Omega^*\right) = -\frac{\omega^2}{\omega_\mathrm{p}^2}\frac{1}{\beta\gamma_\mathrm{w}^2}\frac{1}{2}\frac{d|\Omega|^2}{d\phi} \tag{2.45}$$

Taking into account 2π-periodicity of the solution, one obtains the simplest monochromatic wave that describes a magnetic shear

$$\Omega = \Omega_0 e^{i\phi}, \qquad p_\perp = \frac{\Omega}{\beta\gamma_\mathrm{w}^2}\frac{\omega^2}{\omega_\mathrm{p}^2} \tag{2.46}$$

In the frame moving with β, the wave speed is 0, so is the wave frequency. At each point the conduction currents are parallel to the magnetic field, which is static in that frame and its direction rotates through a full angle in one wavelength. The rate at which the vector rotates is arbitrary, in general it is determined by the dependence of the proper density n on the phase.

2.2.3 Superluminal mode: linearized theory

Before considering a fully nonlinear, superluminal mode, let us first remark on a small-amplitude, plane wave, propagating in an unmagnetized plasma $B_x = 0$. In addition, we require that the phase-averaged transverse components vanish $\langle B_y \rangle = 0 = \langle B_z \rangle$ such that $\Omega_z - \nu_y/\beta = 0 = \Omega_y + \nu_z/\beta$. By calculating a partial time derivative of Ampère's law, and using $\partial \boldsymbol{B}/\partial t$ from Faraday's law, together with $\nabla \times (\nabla \times \boldsymbol{E}) = \nabla(\nabla \cdot \boldsymbol{E}) - \nabla^2 \boldsymbol{E}$, one arrives at the wave equation for the transverse electric field

$$c^2 \nabla^2 \boldsymbol{E} - \partial_t^2 \boldsymbol{E} - 4\pi \partial_t \boldsymbol{j} = 0 \tag{2.47}$$

Let us substitute the usual ansatz $\boldsymbol{E} = \boldsymbol{E_0} e^{i(\omega t - kx)} = \boldsymbol{E_0} e^{i\phi}$, where $k = \omega/c\beta$. Such a wave is described as a small perturbation of the medium density δn, and a small perturbation of the medium velocity $\boldsymbol{u}$. To the first order in small quantities, one arrives at

$$\partial_t \boldsymbol{j} = \partial_t (2nec\boldsymbol{u}) = 2\frac{ne^2}{m}\boldsymbol{E} \tag{2.48}$$

We also change the derivatives according to (2.8), and finally

$$\left(-c^2k^2 + \omega^2 - \omega_\mathrm{p}^2\right)\boldsymbol{E} = 0 \tag{2.49}$$

where we defined the proper plasma frequency in a pair plasma

$$\omega_\mathrm{p}^2 = \frac{8\pi n e^2}{m} \tag{2.50}$$

Nontrivial solutions of (2.49) can be found if

$$\omega^2 = c^2k^2 + \omega_\mathrm{p}^2 \tag{2.51}$$

This condition defines the dispersion relation for an electromagnetic wave in an unmagnetized plasma. Phase velocity then is given by

$$v_\mathrm{ph} = \frac{\omega}{k} = \frac{c}{\sqrt{1 - \frac{\omega_\mathrm{p}^2}{\omega^2}}} > c \tag{2.52}$$

and is greater than c, since $\omega > \omega_{\rm p}$, as seen from (2.51). The energy is carried with the group velocity of the wave, which is subluminal as required

$$v_{\rm g} = \frac{d\omega}{dk} = c\sqrt{1 - \frac{\omega_{\rm p}^2}{\omega^2}} < c \tag{2.53}$$

Note that

$$\beta = \frac{v_{\rm ph}}{c} = \frac{c}{v_{\rm g}} \equiv \frac{1}{\beta_*} \tag{2.54}$$

hence the dispersion relation (2.51) can be written equivalently as

$$\frac{1}{\gamma_*^2} = \frac{\omega_{\rm p}^2}{\omega^2} \tag{2.55}$$

An electromagnetic wave in a plasma propagates only if its frequency ω is above the plasma frequency $\omega_{\rm p}$. Since the latter defines the characteristic response time for the electrons, the wave electric field that oscillates more slowly, is shielded out. It follows that the condition $\omega = \omega_{\rm p}$ defines the maximum plasma density that can support a given electromagnetic wave. In the nonrelativistic regime $\gamma \approx 1$, hence the proper plasma frequency given by (2.50) and the laboratory one $\omega_{\rm p}^{\rm lab} = 8\pi e^2 N/m$ are almost equal.

This condition is relaxed for nonlinear large-amplitude waves, which are able to accelerate electrons to ultrarelativistic Lorentz factors of the order of the wave strength parameter a. In comparison to the nonrelativistic case the laboratory plasma density $N = \gamma n$ is now increased by the factor of $\gamma = \sqrt{1 + a^2} \approx a$, which follows from Eq. (2.1). The electron response time defined by $t \sim 1/\omega_{\rm p}^{\rm lab}$ is now increased and waves with lower frequencies can propagate. Under these circumstances, the condition for propagation of strong waves in plasmas is less stringent than the one applicable to the linear electromagnetic waves, and it reads

$$\omega^{\rm lab} \gtrsim \frac{\omega_{\rm p}^{\rm lab}}{\sqrt{a}} \tag{2.56}$$

2.2.4 Superluminal nonlinear waves

Here we investigate the more general solution that describes the electromagnetic waves propagating with large amplitudes. In this case a perturbation analysis is not applicable, and fully nonlinear equations have to be solved exactly. Since they simplify in the special frame, we perform the appropriate Lorentz transformation, and search for the solutions in that frame. This approach reveals the specialty of a self-consistent solution: in the frame, in which a superluminal wave has zero group velocity, the displacement current is exactly balanced by the conduction current. Here we review this method for both circular and linear wave polarizations.

For large-amplitude superluminal waves we change the notation, denoting now by p not a momentum, but a 4-velocity of a fluid.

Independently of the wave polarization, (2.35) and (2.34) can be integrated immediately. Since in the special frame $\Delta = \gamma$, the continuity equation gives

$$n\gamma = \text{const} \equiv n_0\gamma_0 \tag{2.57}$$

Also, in this frame the magnetic field vanishes and, as we treat only the transverse waves $\boldsymbol{\nu}_\parallel = 0$, the equation of motion for the parallel momentum reads

$$p_\parallel = \text{const} \equiv p_{\parallel 0} \tag{2.58}$$

Circular polarization

The simplest solution is that with the constant density

$$n = n_0 \tag{2.59}$$

which implies that also the particle Lorentz factor is constant

$$\gamma = \gamma_0 \tag{2.60}$$

Together with (2.33), this implies that the transverse particle momentum is everywhere perpendicular to the electric field. Since $\gamma^2 = 1 + p_\parallel^2 + p_\perp^2$, also $p_\perp^2 = \text{const}$ and we can choose a monochromatic solution

$$p_\perp = p_{\perp 0} e^{iA_1\phi} \tag{2.61}$$

We require it to be $2\pi-$periodic in ϕ, which constrains the integration constant

$$A_1 = 1 \tag{2.62}$$

Substituting this solution into Ampère's law, and into the equation of motion for the transverse momentum (2.34), we get

$$\omega = \omega_\mathrm{p} \tag{2.63}$$

i.e., in the special frame the wave frequency coincides with the plasma frequency – in analogy to the linear theory. Moreover,

$$E = i\frac{mc\omega}{e} p_\perp \tag{2.64}$$

and hence

$$|p_\perp| = \frac{e|E|}{mc\omega} \equiv a \tag{2.65}$$

Linear polarization

When a wave is linearly polarised, the proper density and the particle Lorentz factor are both phase dependent. Combining (2.33) with (2.38) and (2.37), we get

$$\gamma_0 \frac{d\gamma}{d\phi} = -\frac{\omega^2}{\omega_\mathrm{p}^2}\,\nu \frac{d\nu}{d\phi} \tag{2.66}$$

We see that it is convenient to express the phase dependence in terms of a new variable $y = E/E_0$, where E_0 is the maximal electric field, for which we choose the phase to be 1. Then it takes a form

$$mc^2 n_0 \gamma_0 \frac{d\gamma}{dy} = -\frac{E_0^2}{8\pi} y \tag{2.67}$$

Choosing also $\gamma = \gamma_0$ for the phase $y = 1$ we get

$$\begin{aligned} \gamma &= \gamma_0 + \frac{E_0^2}{16\pi mc^2 n_0 \gamma_0}(1 - y^2) \\ &= \gamma_0 + \frac{2\gamma_0}{q}\left(1 - y^2\right) \end{aligned} \tag{2.68}$$

where, following [93], we defined the nonlinearity parameter

$$\begin{aligned} q &= \frac{32\pi mc^2 n_0 \gamma_0^2}{E_0^2} \\ &= \frac{4\gamma_0^2}{a^2}\frac{n_0}{\tilde{n}} \end{aligned} \tag{2.69}$$

and

$$\tilde{n} = \frac{m\omega^2}{8\pi e^2} \tag{2.70}$$

Since the electrons and positrons have the same $p_{\parallel 0}$ and γ_0, we must choose $p_{\perp 0} = 0$ at the phase $y = 1$ in order to fulfill $p_{\perp +} = -p_{\perp -}$. Hence

$$\gamma_0 = \sqrt{1 + p_{\parallel 0}^2} \tag{2.71}$$

and

$$p_\perp = \frac{2\gamma_0}{q}\sqrt{(1-y^2)(1-y^2+q)} \tag{2.72}$$

From Ampère's law

$$\frac{dy}{d\phi} = -\frac{8\pi n e c p_\perp}{\omega E_0} \tag{2.73}$$

$$\left(\frac{\tilde{n}}{n_0}\frac{a}{\gamma_0}\frac{dy}{d\phi}\right)^2 = \frac{p_\perp^2}{\gamma^2} = \frac{(1-y^2)(1-y^2+q)}{(1-y^2+\frac{q}{2})^2} \tag{2.74}$$

the dispersion relation takes a form

$$\begin{aligned} 1 &= \frac{2}{\pi}\int_0^1 \frac{dy}{|dy/d\phi|} \\ &= \frac{2}{\pi}\frac{\tilde{n}}{n_0}\frac{a}{\gamma_0}F_1(q), \end{aligned} \tag{2.75}$$

where we defined

$$F_1(q) = \int_0^1 dy \frac{(1-y^2+\frac{q}{2})}{\sqrt{(1-y^2)(1-y^2+q)}} \tag{2.76}$$

This also defines the procedure of averaging over the phase – for a quantity X it is given by

$$\langle X \rangle = \frac{1}{F_1(q)}\int_0^1 dy \frac{X(y)(1-y^2+\frac{q}{2})}{\sqrt{(1-y^2)(1-y^2+q)}} \tag{2.77}$$

After averaging over the phase, only two independent variables are left in the special frame. We choose them to be q and $p_{\parallel 0}$. The third one is β_*, which defines the Lorentz transformation from the special to the lab frame. Using (2.69) and (2.75) we express the other quantities in terms of these:

$$\frac{n_0}{\tilde{n}} = \frac{16}{\pi^2}\frac{F_1^2(q)}{q} \tag{2.78}$$

$$a = \frac{8\gamma_0}{\pi}\frac{F_1(q)}{q} \tag{2.79}$$

where γ_0 is given by (2.71).

Note that linearly polarized strong waves are not monochromatic. The waveform is a sawtooth, since the electric field changes approximately linearly with the phase. The Lorentz factor of the particles has an approximately parabolic dependence on the phase, while the wave velocity is phase-independent by definition. All these suggest that the solution is obtained by a precise phasing between the particles and the fields. It is interesting is to see how this equilibrium behaves when it is perturbed.

2.3 Radiation processes

Perturbations in the system may appear due to interactions of particles with photons, which may come from external sources or be emitted by the accelerated particles themselves. In the first case, the photons will be upscattered by the relativistic particles in the external inverse Compton (EC) process. In the second case, we talk about the nonlinear inverse Compton (NIC) mechanism, since the particle motion is described by the nonlinear equations [77, 173, 15]. Resulting spectrum is neither inverse-Compton, nor standard synchrotron, but, depending on the strength parameter of the wave, it may resemble one or the other. If an incident wave is weak $a \ll 1$ and a particle initially is at rest, it undergoes only small amplitude oscillations, emitting the scattered radiation in the Thomson regime. If initially a particle moves relativistically, the interaction with the incident wave is the inverse Compton scattering. When, on the other hand, the wave is strong $a \gg 1$, it imparts relativistic speeds to a particle such that in any chosen frame the particle becomes relativistic in one wave period, and the particle emission is always in this sense "inverse Compton". However, despite the fact that the particle trajectory in the wave fields is very different from that of a particle in a static electromagnetic field, radiation emitted by a particle is synchrotron-like. As explained by Rees [173], the reason is that during the fast emission process a relativistically oscillating charge indeed sees the wave field as quasi-static. Therefore, the NIC process is also called "synchro-Compton". In this work we focus on strong waves, and relevant analysis of radiation reaction is discussed in more details.

Let us mention briefly that perturbations in the system can also arise as geometrical effects in the radial propagation. Waves emitted by a pulsar are spherical, but in a short wavelength approximation $\epsilon = (c/\omega)/r \ll 1$ (r is a radius at which the wave is investigated) plane wave approximation is also valid, at least in the lowest order in ϵ. At large wave amplitudes one expects a wavefront to be perturbed by the spherical first-order terms, leading to a slow radial evolution of all the wave quantities. This is the subject discussed in Chapters 4 and 6.

2.3.1 Radiation reaction

In this section we consider the case of a particle interacting with the radiation it emits. The photons exert a recoil force, which makes the particle brake. This effect of radiative dragging is described by an additional force term g^α in the equations of motion

$$m\frac{du^\alpha}{d\tau} = eF^{\alpha\beta}u_\beta + g^\alpha \tag{2.80}$$

where

$$g^\alpha = \frac{2e^2}{3c^2}\left(\frac{d^2u^\alpha}{d\tau^2} + u^\alpha u^\beta \frac{d^2u_\beta}{d\tau^2}\right) \tag{2.81}$$

As already remarked, in the case of a cold fluid, the equation of motion of the fluid is the same as the one-particle Eq. 2.80, but u^α is change for p^α – the 4-velocity of the fluid. The fact that the radiation reaction force (2.81) satisfies the condition $p_\mu g^\mu = 0$ means that there is no heating due to the dragging force, and the cold fluid approach is consistent.
In the Landau-Lifshitz (L-L) [115] approximation the second derivative of 4-velocity is expressed by the equations of motion (2.1) without the radiation reaction force

$$\frac{d^2u^\alpha}{d\tau^2} = \frac{e}{mc}\frac{d}{d\tau}\left(F^{\alpha\beta}u_\beta\right) = \frac{e}{m}\frac{\partial F^{\alpha\beta}}{\partial x^\sigma}u^\sigma u_\beta + \frac{e^2}{m^2c^2}F^{\alpha\beta}F_{\beta\sigma}u^\sigma \tag{2.82}$$

This leads to

$$g^\alpha = \frac{2e^3}{3mc^2}\frac{\partial F^{\alpha\beta}}{\partial x^\sigma}u^\sigma u_\beta + \frac{2e^4}{3m^2c^4}F^{\alpha\beta}F_{\beta\sigma}u^\sigma - \frac{2e^4}{3m^2c^4}u^\alpha F^{\beta\sigma}u_\sigma F_{\beta\lambda}u^\lambda \tag{2.83}$$

When the motion is ultrarelativistic $u \gg 1$ the last term is dominant, because it contains the highest power of the 4-velocity. In this approximation

$$\begin{aligned} g^\alpha &= -\frac{2e^4}{3m^2c^4} u^\alpha F^{\beta\sigma} u_\sigma F_{\beta\lambda} u^\lambda \\ &= -\frac{2e^4}{3m^2c^4} u^\alpha \left[-(\boldsymbol{u}\cdot\boldsymbol{E})^2 + (\gamma\boldsymbol{E} + \boldsymbol{u}\times\boldsymbol{B})^2 \right] \end{aligned} \tag{2.84}$$

The Classical description of radiation damping in L-L approximation is appropriate only if any inhomogeneities of an electromagnetic field are large compared to the classical electron radius $r_0 = e^2/(mc^2)$. Also, in the particle rest frame, the fields must be small in comparison to the critical field of classical electrodynamics $E_{\rm cr} = m^2c^4/e^3$, which would be able to accelerate a particle from rest to the relativistic energy mc^2 over the distance of the classical electron radius r_0. However, quantum effects become important for already weaker fields, of the order of the critical (Schwinger) field of QED $E_{\rm S} = m^2c^3/(e\hbar) = \alpha_{\rm f} E_{\rm cr}$. This field is able to accelerate an electron from rest to the energy mc^2 over one Compton wavelength $\lambda\!\!\!^{-}_{\rm c} = \hbar/mc = r_0/\alpha_{\rm f}$. Such energy would be sufficient to rip virtual e^+e^- pairs out of a vacuum, leading to its breakdown much before the classical limit of validity of the L-L approximation is approached. The importance of the quantum effects is quantified by a Lorentz-invariant parameter η, small in the classical limit

$$\eta = \frac{1}{E_{\rm S}} \sqrt{\left(u_\mu F^{\mu\nu}\right)^2} \ll 1 \tag{2.85}$$

When $\eta \geq 1$ the probability of pair production in trident process[1] is significant. For an ultrarelativistic particle this situation may arise even if $E \ll E_{\rm S}$.

One may note that the ratio of the radiation reaction force to the external electromagnetic force is of the order $e^3/(m^2c^4)\gamma^2|\boldsymbol{F}| = \alpha_{\rm f}\eta\gamma$, hence for an ultrarelativistic particle might be large even though (2.85) holds; in this case radiation reaction is a dominant force acting on the particle.

Let us now apply this analysis to the system we consider, in particular to a circularly polarized self-consistent wave (here, again, p^α is the fluid 4-velocity). As discussed, for a plasma oscillating in the fields of this wave, $\boldsymbol{p}\cdot\boldsymbol{E} = 0$. Simplification also comes from (2.37), for which we have already chosen the averaged magnetic field to vanish, implying $\Omega_z = \nu_y\beta_*$, $\Omega_y = -\nu_z\beta_*$; hence

$$\eta = \frac{e\hbar}{m^2c^3}\Delta|\boldsymbol{E}| \tag{2.86}$$

$$g^\alpha = -\frac{2}{3}\frac{m^2c^3}{\hbar}\alpha_{\rm f}\eta^2 p^\alpha \tag{2.87}$$

where we used the definition of Δ (2.32).

There is an important point to mention. In a self-consistent unperturbed solution $\boldsymbol{p}_\perp$ is always perpendicular to the electric field $\boldsymbol{E}$. Radiation reaction perturbs this equilibrium, making the momentum lag behind the field, which in turn generates a velocity component along the field and thus a particle accelerates. As $\boldsymbol{p}_\perp$ is also not parallel to the magnetic field $\boldsymbol{B}$ any more, a Lorentz force is induced in the direction of the wave motion. As the wave loses the energy for acceleration of the particles, it slows down. Particle motion is determined by interplay between the damping and acceleration forces. Similar situation arises for particles in vacuum strong waves [77].

2.3.2 Inverse Compton scattering on an external photon field

As discussed above, a radiating particle feels a dragging force g^α from the emitted photons, which is given by (2.81). However, when a particle does not radiate itself, but is embedded in

[1] Direct pair production via a virtual photon by an electron or positron in a strong field.

an external (uncorrelated) photon field, a statistical treatment is useful. We assume that the radiation field can be described by the energy-momentum tensor $T_{\mu\nu}$, following next description of the inverse Compton scattering given by Landau & Lifshitz [115] and Phinney [166], and discussed by Padmanabhan [160].

In the electron rest frame the drag force should have a form $\sigma_T \bar{T}^i_0$, where $\bar{T}^i_0$ is the momentum flux of the radiation in the particle rest frame. In an invariant way this force would be given by $\sigma_T T^\mu{}_\nu p^\nu$. Since any force g^μ must satisfy the condition $p_\mu g^\mu = 0$ (as there is no heating due to the force) the final expression is

$$g^\alpha = \sigma_T \left(T^\alpha{}_\beta p^\beta + p^\alpha T_{\mu\nu} p^\mu p^\nu \right) \tag{2.88}$$

When the gradient terms are unimportant, (2.88) reproduces the radiation reaction force in the L-L approximation (2.81). In this case the electromagnetic stress-energy tensor

$$T^{\mu\nu} = \frac{1}{4\pi} \left(F^{\mu\alpha} F^\nu{}_\alpha - \frac{1}{4} g^{\mu\nu} F_{\alpha\beta} F^{\alpha\beta} \right) \tag{2.89}$$

is substituted. Moreover, also a formula for the energy emitted in the synchrotron radiation can be obtained for a particle moving in a uniform magnetic field [160], for which

$$T^\mu{}_\nu = \frac{B^2}{8\pi} \,\mathrm{diag}(1, -1, -1, 1) \tag{2.90}$$

In this case

$$\begin{aligned} g^0 &= \sigma_\mathrm{T} \frac{B^2}{8\pi} \gamma \left[1 - \gamma^2 \left(1 + \beta^2 - 2\beta_z^2 \right) \right] \\ &= \sigma_\mathrm{T} \frac{B^2}{8\pi} \gamma \left(-2\beta^2 \gamma^2 \sin^2 \alpha \right) \end{aligned} \tag{2.91}$$

where $\beta = v/c$ is the particle normalized velocity, α is the pitch angle.

For isotropic, external photon field

$$T^\mu{}_\nu = U_\mathrm{rad} \,\mathrm{diag} \left(1, -\frac{1}{3}, -\frac{1}{3}, -\frac{1}{3} \right) \tag{2.92}$$

one gets the radiation drag force

$$g^\alpha = -\frac{4}{3} \sigma_T U_\mathrm{rad} \, \gamma^2 \left(\frac{\gamma^2 - 1}{\gamma}, p_\parallel, p_\perp \right) \tag{2.93}$$

In Sect. 6.3 we discuss the EC scattering as a damping mechanism of a strong wave, launched from a pulsar wind. This may be of relevance in binary systems, where the energy density of the photons from the companion star can be very high. The EC process, together with the NIC, may be responsible for the formation of the shock between the pulsar and the stellar winds.

Part II

Chapter 3

Rotating black holes and jet launching

Both stellar mass black holes and those which are thought to reside in the centers of galaxies, in a generic case are rotating. The former – because a dying star has typically nonvanishing angular momentum, conserved during the collapse. On the other hand, the spin evolution history of the supermassive holes is richer, as both accretion events and merger encounters can lead to their spinning up or spinning down. Black hole rotation can provide an energy source, which potentially can be exploited in the astrophysically relevant scenarios. As noted by Blandford & Znajek (BZ) [32], braking of the spinning, supermassive black holes by electromagnetic torques, would be able to account for the power of large-scale jets from AGNs. They formulated a theory of the jet launching mechanism, in which the energy transport is mediated by the magnetic field that threads the black hole event horizon. This field is external in origin, possibly dragged into the black hole neighborhood by infalling matter from an accretion disk. Nowadays this is the ergosphere (or rather its "effective" counterpart), not the event horizon, that is thought to play a major role in the energy extraction. A curved spacetime is compared to an electromagnetically active medium, which induces an electric field, driving outwards the current that constitutes the jet outflow.

First, in Sect. 3.1 we summarize briefly the geometry around a rotating black hole, described by the Kerr metric, §3.1.1, and further, in §3.1.2, the formulation of physical laws in the frame of locally nonrotating observers. The mechanical (Penrose) process of the extraction of the black hole rotational energy is described in §3.1.3. However, this picture changes dramatically, when a black hole is immersed in a magnetic field, and new processes become of interest. First in Sect. 3.2 we describe the vacuum magnetosphere, given by Wald's solution. Charge-depleted regions, if maintained in some limited space around black holes, would contain the fields that could be efficient accelerators for any stray particle from t accretion disk. The astrophysics of these processes we describe in Sect. 3.3. Given that the particle acceleration can lead to avalanche pair production, Blandford & Znajek envisaged the formation of a force-free magnetosphere, in analogy with pulsars. The BZ process, in its original version, is described in §3.4, and its recently formulated interpretation in §3.4.2 and §3.4.3. This section is closed by the discussion of the expected efficiency of this process §3.4.4. In Sect. 3.5 we briefly discuss the relevance of accretion disks in the context of the launching of jets, and proposed mechanisms of their collimation and acceleration, §3.5.3. The last subsection §3.5.4 summarizes some recent observations of the extremely rapid TeV variability in blazars, and the proposed models that could potentially explain it.

Here we use geometrized units $c = G = 1$.

3.1 Kerr black holes

3.1.1 The metric

The spacetime around a rotating black hole is given by the Kerr solution of Einstein's equations [94]. In Boyer-Lindquist coordinates (t, r, θ, ϕ), in which cartesian ones are given by

$$\begin{aligned} x &= \sqrt{r^2 + a^2} \sin\theta \cos\phi \\ y &= \sqrt{r^2 + a^2} \sin\theta \sin\phi \\ z &= r \cos\theta, \end{aligned} \tag{3.1}$$

the metric components are expressed by, e.g. [204],

$$g_{tt} = -\left(1 - \frac{2Mr}{\Sigma}\right), \quad g_{t\phi} = -\frac{2Mar\sin^2\theta}{\Sigma}, \quad g_{\phi\phi} = \frac{\tilde{B}}{\Sigma}\sin^2\theta, \quad g_{rr} = \frac{\Sigma}{\Delta}, \quad g_{\theta\theta} = \Sigma \tag{3.2}$$

where

$$\Sigma = r^2 + a^2\cos^2\theta, \qquad \Delta = r^2 + a^2 - 2Mr, \qquad \tilde{B} = (r^2 + a^2)^2 - \Delta a^2 \sin^2\theta \tag{3.3}$$

Here $a = J/M$ is the Kerr parameter, J is the angular momentum of a black hole. This metric has several characteristic radii:

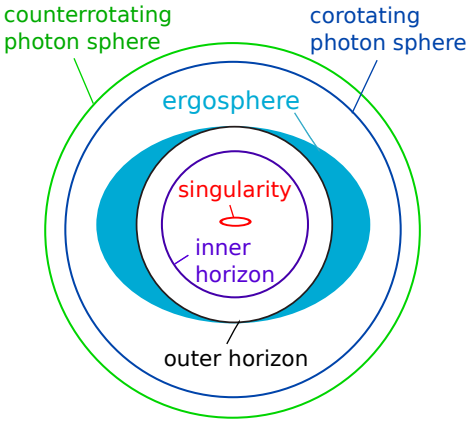

Figure 3.1: Kerr spacetime.

(1) photon spheres (co- and counterrotating) – surfaces defined by unstable orbits of the photons that circulate around a black hole,

(2) innermost stable circular orbit (ISCO) – defined by a radius of marginal stability, inside which no stable rotation of test particles around a black hole is possible,

(3) ergosphere/static limit (see below): $r_e = M + \sqrt{M^2 - a^2\cos^2\theta}$; the name comes from the fact that the energy of a rotating black hole can be extracted mechanically in the region (ergoregion) inside this surface (see §3.1.3),

(4) event horizons: $r_\pm = M \pm \sqrt{M^2 - a^2}$; r_+/r_- is the outer/inner horizon; it is a surface, where the redshift factor vanishes, $g^{rr} = 0$; the existence of the horizons requires $|a| \leq M$, i.e., a black hole is maximally rotating when $a = \pm M$ (extreme black hole)[1],

(5) ring singularity: given by $r = 0$, $\theta = \pi/2$; since in Kerr geometry r defines a disk, not a point in space, the singularity is a ring, located in the equatorial plane.

This stationary, axisymmetric spacetime has a timelike $\eta^\mu = \partial_t$ and an axial $\psi^\mu = \partial_\phi$ Killing vector.[2] Since any timelike vector, when normalized, can be interpreted as a 4-velocity n^μ of some test observer, the timelike Killing vector defines the static observers. Their existence, in turn, defines the static limit, a surface, where the timelike Killing vector becomes null, i.e., $g_{tt} = 0$. Inside this surface all the observers have to rotate with a black hole. A stationary observer has a world line of constant (r, θ) with angular velocity given by

$$\Omega = \frac{d\phi}{dt} = \frac{d\phi/d\tau}{dt/d\tau} = \frac{u^\phi}{u^t} \tag{3.5}$$

[1] In the presence of an accretion disk, photon capture limits this maximal value to 0.998 [196].

[2] Killing vector ξ^μ is a generator of spacetime isometry, i.e., the Lie derivative of a metric tensor in the direction of this vector vanishes, which leads to the Killing equation

$$0 = L_\xi g_{\mu\nu} = \xi^\alpha \nabla_\alpha g_{\mu\nu} + g_{\mu\alpha}\nabla_\nu \xi^\alpha + g_{\alpha\nu}\nabla_\nu \xi^\alpha = \nabla_\nu \xi_\mu + \nabla_\mu \xi_\nu \tag{3.4}$$

Of particular interest are zero angular momentum observers (ZAMO), for whom $L = -\psi^\mu u_\mu = -u_\phi = 0$, i.e., they have no angular momentum with respect to the black hole. Their angular velocity, relative to the distant stars, is given by

$$\Omega_{\rm zamo} = \left.\frac{u^\phi}{u^t}\right|_{\rm zamo} = \frac{g^{t\phi}}{g^{tt}} \tag{3.6}$$

Writing $\chi = \eta + \Omega\psi$, we get ZAMO's 4-velocity

$$n^\mu = \frac{\chi^\mu}{(-\chi\cdot\chi)^{1/2}} = e^{-\Phi}\chi^\mu, \qquad \Phi = \frac{1}{2}\ln\left(-\chi\cdot\chi\right) \tag{3.7}$$

ZAMO is locally nonrotating, but they are not inertial. The acceleration of their worldline[3], e.g., [161]

$$a_\mu = n^\nu\nabla_\nu n_\mu = e^{-\Phi}\chi^\nu\nabla_\nu\left(e^{-\Phi}\chi_\mu\right) = e^{-2\Phi}\left[-\frac{1}{2}\nabla_\mu\left(\chi^\nu\chi_\nu\right) + \frac{\chi^\nu\chi_\mu\chi^\sigma}{-\chi\cdot\chi}\nabla_\nu\chi_\sigma\right] = \nabla_\mu\Phi \tag{3.8}$$

where we used the fact that the second term in the bracket is 0, since an antisymmetric derivative of the Killing field is contracted with the symmetric Killing field.

3.1.2 Spacetime splitting and physics in ZAMO's frame

Splitting of a metric into the spacelike and timelike components allows one to investigate physics in the special frames of test observers. One can measure time at a fixed point of space (i.e., the local time direction is fundamental) or one can look at space at a fixed moment (i.e., the space is fundamental). Thus, there are two different categories of spacetime splittings (for detailed discussion see, e.g., [87, 26, 27] and references therein). The first approach has a unit timelike vector tangent to the "threading" congruence, and this defines the spatial hypersurfaces, to which this vector is normal. In the second approach a unit timelike vector is defined as normal to the chosen space "slices". In the case of Kerr metric, the first approach is characterized by congruences of Killing observers, whereas the second approach defines the frames of locally nonrotating observers. Since they have nonvanishing acceleration, inertial forces enter into their description of physics.

Abramowicz et al. [2] argued that such inertial forces can be interpreted as a result of the deviation of motion from the uniform motion along the trajectories of light, which define dynamically "straight lines" in spacetime. In particular, this formulation gives a physical interpretation of many general relativistic effects that are not explained easily by other approaches. They discuss a static Schwarzschild spacetime, which has some special properties at the radius $r = 3M$: (1) photons have there a circular orbit, (2) all the massive particles need the same thrust, regardless of their orbital speed, to move on this trajectory, (3) gyroscopes carried along this trajectory do not precess with respect to the direction of motion, (4) there is no radiation damping acting on the charges, moving along this trajectory. They interpret it as the consequence of the fact that along this trajectory particles move along "straight lines" of the geometry. Thus, they do not experience centrifugal forces but only speed-independent gravity, the same as in the case of straight-line motion in Minkowski spacetime.

In the studies of Kerr black holes, of particular interest is the formulation of physics in the frame of locally nonrotating observers. Historically, however, first was the "threading" approach formulated by Landau & Lifshitz [115]. Here we discuss briefly both these approaches, "threading" and "slicing", particularly focusing on the latter.

[3]The integral curve of a timelike vector is a worldline/congruence.

1+3 "threading"

As discussed by Landau & Lifshitz (L-L) [115] a metric of the form

$$ds^2 = g_{tt}dt^2 + 2g_{ti}dx^t dx^i + g_{ij}dx^i dx^j \tag{3.9}$$

can be written as

$$\begin{aligned} ds^2 &= g_{tt}\left(dt + \frac{g_{t\phi}}{g_{tt}}d\phi\right)^2 + \left(g_{\phi\phi} - \frac{g_{t\phi}^2}{g_{tt}}\right)d\phi^2 \\ &= -h^2(dt - g_i dx^i)^2 + \gamma_{ab}dx^a dx^b \end{aligned} \tag{3.10}$$

where

$$g_a = -\frac{g_{ta}}{g_{tt}}, \qquad h^2 = -g_{tt} \tag{3.11}$$

and γ_{ab} parameterizes the spatial metric. One can choose new coordinates as

$$\tilde{x}^i = x^i, \qquad \tilde{t} = t - g_i x^i, \tag{3.12}$$

and new basis vectors

$$\tilde{X}^i = \partial_i + g_i\partial_t, \quad \tilde{X}\cdot\tilde{X} = \gamma_{xx}, \qquad \tilde{T} = \partial_t, \quad \tilde{T}\cdot\tilde{T} = -h^2 \tag{3.13}$$

These coordinates are comoving with the observer, whose 4-velocity is $u^\mu = h^{-1}\delta^\mu{}_0$. From (3.13) one can see that the observer worldline coincides with the coordinate time line, and the lapse function h relates the coordinate time to the observer proper time. Thus, the threading congruences that define the spatial hypersurfaces, serve both as the observer congruences, as well as those along which the evolution of spacetime is described.

3+1 "slicing"

In the black hole physics the more popular approach was that of Arnowitt et al. [12] and described by Misner et al. [152] and Thorne et al. [197]. Since these results are crucial in the sense that they are widely used in black hole electrodynamics studies, here we show their derivation from first principles. Although physically intuitive, the derivation is mathematically involved, and precise formulation is discussed by Gourgoulhon [73].

In Thorne's approach the spacetime splitting is different than that of L-L, i.e., the metric (3.9) is written as

$$\begin{aligned} ds^2 &= \left(g_{tt} - \frac{g_{t\phi}^2}{g_{\phi\phi}}\right)dt^2 + g_{\phi\phi}\left(d\phi + \frac{g_{t\phi}}{g_{\phi\phi}}dt\right)^2 \\ &= -\alpha^2 dt^2 + \tilde{g}_{ij}(dx^i + \beta^i dt)(dx^j + \beta^j dt) \end{aligned} \tag{3.14}$$

A family of spacelike hypersurfaces has a unit normal n^μ, which is 4-velocity of a test observer

$$n^\mu = \frac{1}{\alpha}\left(\delta^\mu{}_0 - \beta^i\delta^\mu_i\right) \tag{3.15}$$

New coordinates can be chosen as

$$\bar{x}^i = x^i + \beta^i t, \qquad \bar{t} = t, \tag{3.16}$$

and new basis vectors

$$\bar{X}^i = \partial_i, \quad \bar{X}\cdot\bar{X} = g_{xx}, \qquad \bar{T} = \partial_t - \beta^i\partial_i, \quad \bar{T}\cdot\bar{T} = -\alpha^2 \tag{3.17}$$

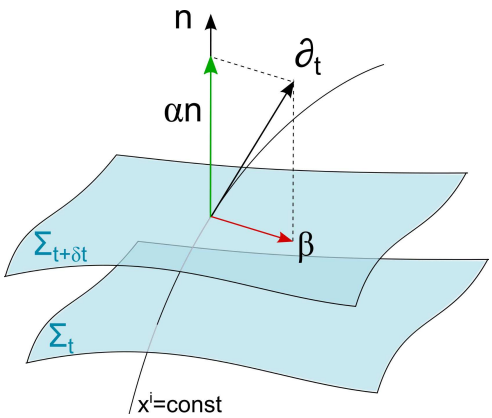

Figure 3.2: Spacetime slicing. Lines $x^i = \text{const}$ across Σ_t define ∂_t and β of the coordinates t, x^i.

Now the shift vector β^i is spatial and determines the shift of the coordinate time line away from the observer worldline (see Fig. 3.2). The lapse function α, similar as before, relates the coordinate time along the observer worldline to the observer proper time. This shows that now the observer worldline does not coincide with the coordinate time line. There is a need for a new temporal derivative along the threading curves that would act as an evolution operator. One defines the normal evolution vector that is perpendicular to the spatial hypersurfaces, i.e., $m^\mu = \alpha n^\mu$ [73], and drags the hypersurfaces along the threading curves. For any spatial vector A^μ on the spatial hypersurface, its shift is expressed by the Lie derivative in the direction of m:

$$\mathcal{L}_m A^\nu = m^\mu \nabla_\mu A^\nu - A^\mu \nabla_\mu m^\nu \qquad \mathcal{L}_m A_\nu = m^\mu \nabla_\mu A_\nu + A_\mu \nabla_\nu m^\mu \tag{3.18}$$

Using this, one can write equations of motion of a free particle. The particle 4-velocity can be decomposed into the component parallel to the observer's velocity, and to the orthogonal component, which belongs to a spatial hypersurface

$$u^\mu = \gamma \left(n^\mu + v^i \delta_i{}^\mu \right) \tag{3.19}$$

The equation of motion is given by

$$0 = u^\mu \nabla_\mu u_\nu = \gamma \left(n^\mu + v^i \delta_i^\mu \right) \nabla_\mu u_\nu \tag{3.20}$$

and its first term

$$n^\mu \nabla_\mu u_\nu = \frac{1}{\alpha} m^\mu \nabla_\mu u_\nu = \frac{1}{\alpha} \left(\mathcal{L}_m u_\nu - u_\mu \nabla_\nu m^\mu \right) \tag{3.21}$$

One obtains

$$\frac{1}{\alpha} \mathcal{L}_m u_\nu - \frac{1}{\alpha} u_\mu \nabla_\nu m^\mu + v^i \delta_i^\mu \nabla_\mu u_\nu = 0 \tag{3.22}$$

Using the definition of the shift vector $\boldsymbol{\beta}$

$$\partial_t = m + \boldsymbol{\beta} \tag{3.23}$$

one can express the Lie derivative along m^μ by the Lie derivative along the timelike Killing vector and the orthogonal shift (on the spatial surface) along $\boldsymbol{\beta}$

$$\begin{aligned} \mathcal{L}_m &\to \mathcal{L}_{\partial_t} - \mathcal{L}_{\boldsymbol{\beta}} \\ &= \frac{\partial}{\partial t} - \mathcal{L}_{\boldsymbol{\beta}} \end{aligned} \tag{3.24}$$

Taking into account the definition of Lie derivative and denoting the particle momentum measured by ZAMO as $p_i = m\gamma v_i$ one arrives at

$$\frac{1}{\alpha}\left(\frac{\partial}{\partial t} - \boldsymbol{\beta}\cdot\tilde{\nabla} + \alpha\boldsymbol{v}\cdot\tilde{\nabla}\right)p_i = m\gamma g_i \tag{3.25}$$

where we denoted by $\tilde{\nabla}$ a spatial covariant derivative, acting on the spatial hypersurfaces (obtained by restriction of 4D metric to its 3D spatial part), and

$$g_i = -\frac{1}{\alpha}\tilde{\nabla}_i\alpha = -\tilde{\nabla}_i \ln\alpha \tag{3.26}$$

For the covariant components one has to rise an index but this involves multiplying by the 3-metric $\tilde{g}^{ij}$. It does not commute with the Lie derivative $\mathcal{L}_m$ and a new term appears $\mathcal{L}_m\tilde{g}^{ij} = 2\alpha H^{ij}$ [73], where

$$H_{ij} = \frac{1}{\alpha}\tilde{\nabla}_i\beta_j \tag{3.27}$$

so that we finally get

$$\frac{1}{\alpha}\left(\frac{\partial}{\partial t} - \boldsymbol{\beta}\cdot\tilde{\nabla} + \alpha\boldsymbol{v}\cdot\tilde{\nabla}\right)p^i = m\gamma g^i + H^i{}_j p^j \tag{3.28}$$

Maxwell equations can be also written in the ZAMO frame [115, 73]. It is instructive to obtain explicitly at least one example, say Faraday's law. It reads

$$\nabla_\mu {}^*F^{\nu\mu} = 0 \tag{3.29}$$

where

$$F_{\mu\nu} = n_\mu E_\nu - E_\mu n_\nu + \epsilon_{\sigma\rho\mu\nu}n^\sigma B^\rho \tag{3.30}$$

and thus, by replacing $\boldsymbol{E}\to -\boldsymbol{B}$ and $\boldsymbol{B}\to\boldsymbol{E}$ one gets

$${}^*F_{\mu\nu} = -n_\mu B_\nu + B_\mu n_\nu + \epsilon_{\sigma\rho\mu\nu}n^\sigma E^\rho \tag{3.31}$$

The first two terms, when substituted to Faraday's law, give

$$\nabla_\mu\left(-n^\nu B_\mu + B_\nu n_\mu\right) = n^\mu\nabla_\mu B^\nu - B^\mu\nabla_\mu n^\nu - n^\nu\nabla_\mu B^\mu + B^\nu\nabla_\mu n^\mu \tag{3.32}$$

In this equation the last term vanishes, since $\nabla_\mu n^\mu = \sqrt{-g}^{-1}\partial_\mu(\sqrt{-g}n^\mu)$ and the metric is independent of t and ϕ, which could give the only nonvanishing components of n. The first two terms give the Lie derivative of B along n

$$\mathcal{L}_n B^\nu = n^\mu\nabla_\mu B^\nu - B^\mu\nabla_\mu n^\nu \tag{3.33}$$

However, since all the quantities evolve with the normal evolution vector defined as $m^\mu = \alpha n^\mu$ one should rather express the Lie derivative along this vector. It is

$$\mathcal{L}_n B^\nu = \frac{1}{\alpha}\left(\mathcal{L}_m B^\nu + B^\mu n^\nu\nabla_\mu\alpha\right) \tag{3.34}$$

Thus,

$$\nabla_\mu\left(-n^\nu B_\mu + B_\nu n_\mu\right) = \frac{1}{\alpha}\mathcal{L}_m B^\nu - n^\nu\left(\nabla_\mu B^\mu - B^\mu\nabla_\mu\ln\alpha\right) = \frac{1}{\alpha}\mathcal{L}_m B^\nu - n^\nu\tilde{\nabla}_\mu B^\mu \tag{3.35}$$

where $\tilde{\nabla}$ is the derivative, restricted only to the spatial hypersurface. In the last equation we used the fact that for any two vectors u and v tangent to the spatial hypersurface [73]

$$\begin{aligned} u^\mu\tilde{\nabla}_\mu v^\alpha = u^\sigma\tilde{g}^\nu{}_\sigma\tilde{g}^\alpha{}_\mu\nabla_\nu v^\mu = u^\nu\left(\delta^\alpha_\mu + n^\alpha n_\mu\right)\nabla_\nu v^\mu = u^\nu\nabla_\nu v^\alpha + n^\alpha u^\nu n_\mu\nabla_\nu v^\mu \\ = u^\nu\nabla_\nu v^\alpha - n^\alpha\left(u^\nu v^\mu\nabla_\nu n_\mu\right) \end{aligned} \tag{3.36}$$

where we used $n_\nu v^\nu = 0$ (n is orthogonal to the spatial hypersurfaces). Taking $v^\alpha = B^\alpha$ and $\alpha = \nu = \mu$, we have $B^\nu n^\mu \nabla_\mu n_\nu = -B^i n^\mu \Gamma^\sigma_{\mu i} n_\sigma = -B^i \nabla_i \ln \alpha$, and finally we arrive at (3.35).

Further, since the covariant derivative of the Levi-Civita tensor vanishes,

$$\nabla_\mu \left(\epsilon^{\rho\sigma\nu\mu} n_\rho E_\sigma\right) = \epsilon^{\rho\sigma\nu\mu} \left(\tilde{m}_\rho E_\sigma \nabla_\mu \alpha + \alpha E_\sigma \nabla_\mu \tilde{m}_\rho + n_\rho \nabla_\mu E_\sigma\right) \tag{3.37}$$

where we defined auxiliary vector $\tilde{m}_\rho = n_\rho/\alpha$. The second term in the bracket vanishes, because in $\nabla_\mu \tilde{m}_\rho = \partial_\mu \tilde{m}_\rho - \Gamma^\eta_{\mu\rho} \tilde{m}_\eta$ the partial derivative of $\tilde{m}_\mu = (-1, 0, 0, 0)$ gives 0 and symmetric Christoffel symbols, contracted with antisymmetric Levi-Civita tensor, also give a vanishing term. Finally we get

$$\nabla_\mu \left(\epsilon^{\rho\sigma\nu\mu} n_\rho E_\sigma\right) = -\epsilon^{0\sigma\nu\mu} \tilde{\nabla}_\mu \left(\alpha E_\sigma\right) \tag{3.38}$$

Faraday's law takes a form

$$\frac{1}{\alpha} \mathcal{L}_m B^\nu - n^\nu \tilde{\nabla}_\mu B^\mu - \epsilon^{0\sigma\nu\mu} \tilde{\nabla}_\mu \left(\alpha E_\sigma\right) = 0 \tag{3.39}$$

where we note that $\det g_{\mu\nu} = -\alpha^2 \det \tilde{g}_{\mu\nu}$ and thus $\epsilon^{0ijk} = -\epsilon^{ijk}/\alpha$. This equation can be projected along the threading curve by multiplying by n_ν. One can notice that, since the Lie derivative of tangent, spatial vectors along m^μ leaves them in the spatial surface, $\mathcal{L}_m B^\mu$ remains tangent to the threading curve and, thus, one gets

$$\tilde{\nabla}_i B^i = 0 \tag{3.40}$$

Projection on spatial hypersurface (i.e., multiplying by $n_\nu n^\lambda + \delta^\lambda_\nu$), gives

$$\mathcal{L}_m B^i + \epsilon^{ijk} \tilde{\nabla}_j \left(\alpha E_k\right) = 0 \tag{3.41}$$

Using the definition of the shift vector $\boldsymbol{\beta}$

$$\partial_t = m + \boldsymbol{\beta} \tag{3.42}$$

one can express the Lie derivative along m^μ by the Lie derivative along the coordinate time line and the orthogonal shift (on the spatial surface) along $\boldsymbol{\beta}$

$$\begin{aligned} \mathcal{L}_m &\to \mathcal{L}_{\partial_t} - \mathcal{L}_{\boldsymbol{\beta}} \\ &= \frac{\partial}{\partial t} - \mathcal{L}_{\boldsymbol{\beta}} \end{aligned} \tag{3.43}$$

Faraday's law reads

$$\left(\frac{\partial}{\partial t} - \mathcal{L}_{\boldsymbol{\beta}}\right) B^i + \epsilon^{ijk} \tilde{\nabla}_j \left(\alpha E_k\right) = 0 \tag{3.44}$$

The remaining Maxwell equations are obtained in the same manner. Gauss law is given by

$$\tilde{\nabla}_i E^i = 4\pi\rho \tag{3.45}$$

and Ampère's law

$$\left(\frac{\partial}{\partial t} - \mathcal{L}_{\boldsymbol{\beta}}\right) E^i - \epsilon^{ijk} \tilde{\nabla}_j \left(\alpha B_k\right) + 4\pi\alpha j^i = 0 \tag{3.46}$$

where $\rho = -n_\mu j^\mu$ is the charge density and $j^\mu = \rho n^\mu + J^i \delta^\mu_i$ is the current density measured by ZAMO, which satisfies the continuity equation

$$\left(\frac{\partial}{\partial t} - \boldsymbol{\beta} \cdot \nabla\right) \rho + \tilde{\nabla}_i \left(\alpha j^i\right) = 0 \tag{3.47}$$

Gravitoelectromagnetism

In the Newtonian limit of a weak gravitational field, i.e., far from a black hole $r \gg M$,

$$\alpha \simeq 1, \qquad |\boldsymbol{\beta}| \ll |\boldsymbol{v}| \tag{3.48}$$

so that the equations of motion of a particle (3.28) take a form [197]

$$m\frac{d^2x^i}{dt^2} \simeq mg^i + m\left(H^i{}_k - H_k{}^i\right)\frac{dx^k}{dt} \tag{3.49}$$

which may be written as

$$m\frac{d^2\boldsymbol{x}}{dt^2} \simeq m\left(\boldsymbol{g} + \frac{d\boldsymbol{x}}{dt} \times \boldsymbol{H}\right), \qquad \boldsymbol{H} = \nabla \times \boldsymbol{\beta} \tag{3.50}$$

This weak gravity limit of the force measured by ZAMO looks like a Lorentz force, with charge e replaced by mass m, $\boldsymbol{E}$ replaced by $\boldsymbol{g}$, $\boldsymbol{B}$ replaced by $\boldsymbol{H}$, and vector potential $\boldsymbol{A}$ replaced by $\boldsymbol{\beta}$. For that reason, the shift function $\boldsymbol{\beta}$ is called gravitomagnetic potential, and $\boldsymbol{g}$ – gravitoelectric acceleration. This analogy with electrodynamics is, in fact, even deeper. The Einstein field equations that govern the gravitational field of a rotating mass, in a weak gravity limit, and in a time-independent case, look like Maxwell's equations for electromagnetism [197]

$$\nabla \times \boldsymbol{H} = -16\pi G\rho_{\mathrm{m}}\boldsymbol{v}, \quad \nabla \times \boldsymbol{g} = 0, \quad \nabla \cdot \boldsymbol{g} = -4\pi G\rho_{\mathrm{m}}, \quad \nabla \cdot \boldsymbol{H} = 0 \tag{3.51}$$

A difference is made by minus signs, which means that gravity is rather attractive than repulsive. For time dependent objects (pulsating, collapsing etc.) the direct analogy is valid unless velocities become comparable to the speed of light, or gravity becomes too strong to use linearizing techniques (even in that case, however, the analogy is not completely disrupted) [35].

3.1.3 Energy extraction from Kerr black holes – the Penrose process

Penrose [163] showed that the energy can be extracted from a rotating black hole in a simple mechanical process. Consider a particle A, moving with the energy at infinity E_A along the geodesics. Its energy is conserved during the motion

$$E_A = -\eta^\mu p_{(A)\mu} \tag{3.52}$$

Suppose that when it enters the ergosphere, we arrange its splitting into two particles B and C (e.g., by some explosive, timing devices), B falls into the black hole and C escapes to radial infinity. The 4-momentum conservation reads

$$p^\alpha_{(A)} = p^\alpha_{(B)} + p^\alpha_{(C)} \tag{3.53}$$

and, when contracted with η_α,

$$E_{(A)} = E_{(B)} + E_{(C)} \tag{3.54}$$

However, in the ergosphere η^μ is spacelike, so for certain choices of a timelike momentum vector, $E = -\eta \cdot p$ can be negative (those are negative energy at infinity states). Thus, in the ergosphere it is possible that $E_{(B)} < 0$ ($p_{(B)t} > 0$). If C escapes to infinity on a geodesics, the energy conservation implies that its energy is greater than that of the infalling particle A.

In the ergosphere ZAMO velocity is $u = \xi + \Omega_{\mathrm{zamo}}\psi$ (assuming normalization), and the energy of the particle B which they measure is

$$E^{\mathrm{zamo}}_{(B)} = -\xi^\mu p_{(B)\mu} - \Omega_{\mathrm{zamo}}\psi^\mu p_{(B)\mu} = -p_{(B)t} - \Omega_{\mathrm{zamo}}p_{(B)\phi} \tag{3.55}$$

This locally measured energy has to be positive, hence

$$-p_{(B)t} - \Omega_{\rm zamo} p_{(B)\phi} > 0 \tag{3.56}$$

$$\Omega_{\rm zamo} p_{(B)\phi} < -p_{(B)t} \tag{3.57}$$

Thus, for negative energy at infinity states, the local observer sees that $p_{(B)\phi} < 0$, i.e., that a particle falls into the black hole in the direction opposite to its rotation, braking it. That is, the ergosphere supports the negative energy at infinity orbits of particles provided that their angular momentum is directed opposite to the angular momentum of the black hole. As a consequence, the escaping particle C has larger energy than the infalling particle A, and this occurs at the expense of the rotational energy of a black hole.

3.2 Wald's solution and the vacuum magnetosphere

No-hair theorem says that an uncharged black hole, which we considered above, cannot generate its own magnetic field, because this would require a well defined distribution of currents behind the horizon. However, a rotating black hole can be immersed in a magnetic field that is supported externally by, e.g., an accretion disc.

An interesting, special solution for an electromagnetic field in the vicinity of a rotating black hole, placed in an originally uniform, aligned magnetic field, was given by Wald [203]. To obtain it, he used the fact that a Killing vector ξ^α in a vacuum spacetime generates a solution of Maxwell equations in that spacetime, i.e., the field $F_{\mu\nu} = \nabla_\mu \xi_\nu - \nabla_\nu \xi_\mu$ satisfies the source-free Maxwell equations $\nabla_\mu F^{\mu\nu} = 0$. It is straightforward to show it, taking the definition of the Riemann tensor

$$\nabla_\alpha \nabla_\beta \xi_\gamma - \nabla_\beta \nabla_\alpha \xi_\gamma = -\xi^\lambda R_{\lambda\gamma\alpha\beta} \tag{3.58}$$

permuting indices cyclically, adding these three permuted equations, and finally using the Riemann tensor symmetry $R_{\lambda[\alpha,\beta,\gamma]} = 0$. One obtains

$$\begin{aligned} \nabla_\alpha \nabla_\beta \xi_\gamma &= \nabla_\gamma \nabla_\beta \xi_\alpha - \nabla_\beta \nabla_\gamma \xi_\alpha \\ &= R_{\lambda\alpha\gamma\beta} \xi^\lambda \end{aligned} \tag{3.59}$$

and after contraction of indices α and β,

$$\nabla_\alpha \nabla^\alpha \xi^\gamma = R_{\lambda\alpha}{}^{\gamma\alpha} \xi^\lambda = R^\gamma{}_\lambda \xi^\lambda \tag{3.60}$$

For a vacuum spacetime the Einstein field equations are $R_{\alpha\beta} = 0$ (note that in a general case this condition does not imply that the components of the Riemann tensor vanish), hence $\nabla_\alpha \nabla^\alpha \xi^\gamma = 0$. On the other hand, $\nabla_\mu F^{\mu\nu} = \nabla_\mu (\nabla^\mu \xi^\nu - \nabla^\nu \xi^\mu) = 2 \nabla_\mu \nabla^\mu \xi^\nu$, which proves that Maxwell equations are satisfied.

In a flat space there are 10 independent Killing vectors: rotational ones generate uniform magnetic fields, boost ones generate uniform electric fields and the field generated by the four translational Killing vectors vanishes [203]. In a stationary axisymmetric spacetime there exists the timelike $\eta^\mu = \partial_t$ and the axial $\psi^\mu = \partial_\phi$ Killing vector, hence the field tensor F is a combination of $F_\psi = d\psi$ and $F_\eta = d\eta$. At large distances F_ψ becomes a uniform magnetic field B_0 and the charge of F_ψ is associated with the angular momentum J of the spacetime [44].

$$4\pi q_\psi = \int {}^*F_\psi = \int {}^*d\psi = 16\pi J \tag{3.61}$$

On the other hand, F_η, determining an electric field, vanishes asymptotically and its charge is associated with the mass of the original vacuum spacetime

$$4\pi q_\eta = \int {}^*F_\eta = \int {}^*d\eta = -8\pi M \tag{3.62}$$

Wald noted that these properties are satisfied by the general solution

$$F = \frac{1}{2} B_0 \left(d\psi + \frac{2J}{M} d\eta \right). \tag{3.63}$$

Explicitly, for a Kerr spacetime in the orthonormal tetrad

$$\begin{aligned} \omega^0 &= \sqrt{\frac{\Delta}{\Sigma}} \left(dt - a \sin^2\theta d\phi \right), & \omega^1 &= \sqrt{\frac{\Sigma}{\Delta}} dr, \\ \omega^2 &= \sqrt{\Sigma} d\theta, & \omega^3 &= \frac{\sin\theta}{\sqrt{\Sigma}} \left[-a dt + (r^2 + a^2) d\phi \right] \end{aligned} \tag{3.64}$$

the components of the Wald electromagnetic tensor defined by $F = F_{\mu\nu} \omega^\mu \wedge \omega^\nu$, are given by

$$F_{10} = \frac{B_0}{\Sigma} \left(ar \sin^2\theta - \frac{aM}{\Sigma} (r^2 - a^2 \cos^2\theta)(1 + \cos^2\theta) \right) \tag{3.65}$$

$$F_{13} = \frac{B_0}{\Sigma} \Delta^{1/2} r \sin^2\theta \tag{3.66}$$

$$F_{20} = \frac{B_0}{\Sigma} \Delta^{1/2} a \sin\theta \cos\theta \tag{3.67}$$

$$F_{23} = \frac{B_0}{\Sigma} \cos\theta \left(r^2 + a^2 - \frac{2a^2 M}{\Sigma} r (1 + \cos^2\theta) \right) \tag{3.68}$$

The Wald solution shows that due to the spacetime rotation, an electric field is generated close to the black hole. The components of the Wald field can be transformed to the ZAMO frame. Using definitions of the magnetic and electric fields, as measured by an observer with 4-velocity u^α (e.g. [204]),

$$B_i = -\frac{1}{2} \epsilon_{i\alpha\mu\nu} F^{\mu\nu} u^\alpha, \qquad E_i = F_{i\alpha} u^\alpha \tag{3.69}$$

one obtains the result shown in Fig. 3.3 for two different values of a, which we have chosen to be 0.5 and 1. The electric field induced by the black hole rotation has a quadrupole geometry. However, it diminishes as $1/r^2$ at large distances, whereas the true quadrupole has $1/r^4$ dependence. An interesting property of the Wald's solution is that the faster a black hole rotates, the more magnetic field lines are expelled from the horizon. For a maximally rotating hole, there are no lines threading it. This is called the Meissner effect for black holes.

The topology of an electromagnetic field determines the structure of a magnetosphere (here a vacuum one), and the trajectories of the test particles that may enter it. The Wald magnetosphere contains two force-free surfaces, where $\boldsymbol{E} \cdot \boldsymbol{B} = 0$. The first one is the equatorial plane, and the second one is a hollow cone around the rotational axis, with an inclination angle defined by the cusp of an electric field. In Wald's solution the magnetic field is aligned with the rotation axis of the hole, and negative charges on the symmetry axis are repelled by the hole, whereas positive charges are accreted. It can be shown by considering the particle's energy when lowering it down the symmetry axis $\epsilon = E_\mathrm{f} - E_\mathrm{i} = e A_\mu \eta^\mu|_\mathrm{hor} - e A_\mu \eta^\mu|_\infty$. If ϵ is positive, it is energetically favorable for the black hole to accrete the positive charges. Accretion can be sustained until $\epsilon = 0$ and this condition defines the Wald's charge $Q_\mathrm{W} = 2 B_0 J$. A solution for a black hole charged with $Q = f Q_\mathrm{W}$ (f denotes the fraction of the maximum charge, which has been already accreted by the hole) in a uniform magnetic field is a sum of the uncharged solution (3.63) and the charge perturbation, proven by Wald to be $(-Q/2M) F_\eta$

$$F = \frac{1}{2} B_0 \left(d\psi + \frac{2J}{M} d\eta \right) - \frac{Q}{2M} d\eta_\mu \tag{3.70}$$

As he discussed, the contribution to the electric field from the accreted charges is not significant, however, since a Kerr black hole must satisfy $a \leq M$, $Q/M \leq 2 B_0 M$.

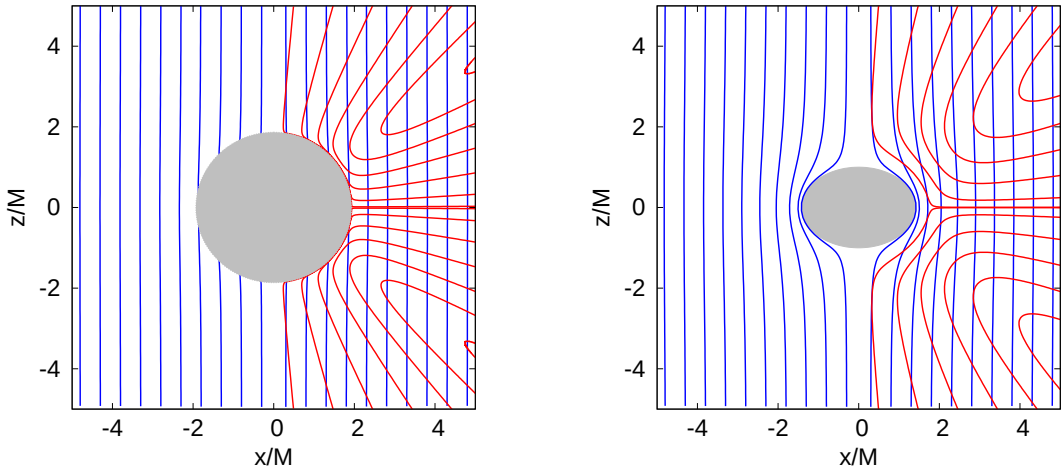

(a) $a/M = 0.5$ (b) $a/M = 1$

Figure 3.3: A rotating black hole (gray shading), placed in an asymptotically uniform magnetic field (Wald's solution). Blue: magnetic field lines, red: electric field lines (shown only for one half space), in the ZAMO frame.

In a general case of a strong field, to consider the test particle trajectories quantitatively, it is necessary to take into account radiation damping (see §2.3.1, where we discuss radiation reaction). For a given particle of mass m and charge e, the ratio of its gyroradius $r_{\rm gy} = m/eB$ to the gravitational radius $r_{\rm g} = M$, depends only on the product MB, thus, when radiation reaction is unimportant, the dynamics is the same for supermassive holes with lower fields and the less massive holes with the stronger fields. Radiation damping changes this picture, and can significantly affect the motion in the magnetosphere [156]. The equations of motion take a form

$$\frac{du_\alpha}{d\tau} = \Gamma^\rho_{\alpha\beta} u_\rho u^\beta + \frac{e}{m} F_{\alpha\beta} u^\beta - \frac{2e^4}{3m^3} F_{\mu\nu} u^\nu F^{\mu\rho} u_\rho u_\alpha \tag{3.71}$$

where we employed the Landau-Lifshitz approximation for the radiation reaction and we took into account only the largest term of the force acting on the particle. These trajectories are shown in Fig. 3.4 below. One can see that if initially the particles are located in latitudes between the equator and the inclined force-free surface, the electrons are attracted to the former, and the positrons to the latter, so that the force-free surfaces trap the particles undergoing strong radiation reaction. Surfaces attracting opposite charges are well separated, but in a more general solution of the asymptotically uniform magnetic field that is misaligned with the rotational axis of a black hole (this solution was given by [28]), it was shown that these force-free surfaces "reconnect" [156].

For pulsars a similar problem was studied by Finkbeiner el al. [59]. They considered a star, endowed with the vacuum dipole magnetic field (Deutsch solution), and considered the motion of particles from its surface. Their motivation was to obtain a self-consistent picture, where the magnetosphere is gradually filled up with the charges that modify the initially vacuum field. They found that the trajectories on which the radiation reaction is minimized during the motion define the local velocity field. It is an attractor for the particles undergoing strong radiation damping, and the stronger is the damping, the faster the particle velocity converges with the local field. In particular, a particle trapping on the force-free surfaces was observed. The local field was calculated by solving $g^\alpha = 0$, where the force g^α is given by (2.84), and the solution is given by

$$\boldsymbol{v}_{\rm L} = \frac{1}{B^2 + P^2} \left(\boldsymbol{E} \times \boldsymbol{B} + \frac{\boldsymbol{E} \cdot \boldsymbol{B}}{P} \boldsymbol{B} + P \boldsymbol{E} \right), \tag{3.72}$$

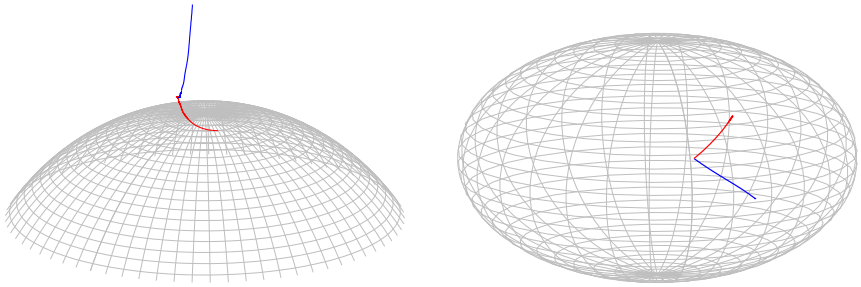

(a) (b)

Figure 3.4: Trajectories of charged particles in the Wald field: blue e^-, red e^+, in gray the black hole horizon (or its part) is shown. Initially the particles are located above the event horizon of a rotating black hole with $a = 0.5$: (a) in polar regions e^- is expelled, whereas e^+ is accreted onto the black hole, (b) for latitudes higher than 0 both particles move towards the force-free surfaces. The trajectories exhibit wiggles as the particles radiate and recoil, but these features are not seen on the scale of the figures.

where

$$P = \mathrm{sgn}(e)\left\{\tfrac{1}{2}(\boldsymbol{E}^2 - \boldsymbol{B}^2) + \tfrac{1}{2}\sqrt{(\boldsymbol{E}^2 - \boldsymbol{B}^2)^2 + 4(\boldsymbol{E}\cdot\boldsymbol{B})^2}\right\}^{1/2}. \tag{3.73}$$

It has a drift component $\propto \boldsymbol{E}\times\boldsymbol{B}$, a component describing the motion along the magnetic field $\propto (\boldsymbol{E}\cdot\boldsymbol{B})\boldsymbol{B}$, and a component along the electric field $\propto \boldsymbol{E}$. For black holes, all these vector operations should be understood as performed in a curved space of ZAMO.

In fact, a proper description of radiation reaction in a Kerr metric is much more tricky, since the causal structure of the Green's functions is richer in the curved spacetime than it is in the flat one[4] (for exhaustive discussion see Poisson [167]). As a consequence, radiation reaction has a gravitational part, which appears only due to the presence of a curvature. The equation of motion of a point charge in a curved spacetime, including its self-force, was carried out by DeWitt & Brehme [53] and corrected by Hobbs [84]. However, when the gravitational radius is much larger than the gyroradius of a particle, radiation reaction due to presence of curvature can be ignored. This is the case in the astrophysical context.

3.3 Particle acceleration and cascade pair production

In the Wald solution the normal component of a magnetic field B_n generates an electric field of the order $E \sim \Omega_\mathrm{H} r_\mathrm{H} B_\mathrm{n}$. The potential difference within the gap of height $\sim r_\mathrm{H}$, induced above the polar regions, reaches

$$U \sim E r_\mathrm{H} \sim \frac{1}{2}\frac{a}{M} B_\mathrm{n} r_\mathrm{H} \sim 2\times 10^{19}\,\mathrm{V}\left(\frac{a}{M}\right)\left(\frac{M}{10^9\mathrm{M}_\odot}\right)\left(\frac{B_\mathrm{n}}{10^4\mathrm{G}}\right) \tag{3.74}$$

Thus, acceleration of any stray particle from an accretion disk, can be very efficient. The supermassive black holes that can sustain such fields in very limited regions of their magnetospheres, were considered as candidates for the cosmic ray (CR) accelerators [34]. However, due to curvature losses, the energy a particle can gain in the gap must be limited far below the maximum value that is defined by the potential drop [122]. As argued by Levinson, the curvature photons would be emitted in TeV band, and could, in turn, produce pairs via scattering on external soft photons, originating from the accretion disk. However, if such soft photons were not prolific in the black hole vicinity, the very high energy (VHE) curvature radiation would be able to escape. Apart from being a particle accelerator, such an object would be also a TeV emitter [122, 156].

[4] In a curved space, the vector potential of an electromagnetic field couples to the Ricci tensor, and the wave equation is more complicated in comparison to that in a flat space.

The absence of soft photon fields around a black hole, places restrictions on the class of the objects that can be the candidates for the accelerators, i.e., these must be dormant AGNs or quasar remnants. Boldt & Ghosh [34] and also Levinson [122] argued that massive dark objects (MDOs) in the centers of nearby galaxies, detected recently by [138], satisfy these criteria. Some of them have masses in excess of $10^{10}\mathrm{M}_{\odot}$ and it is not well understood why they do not show any accretion activity, remaining radiatively inefficient. Thus, without rich environment, such objects may be able to sustain vacuum gaps, not broken down by the pair cascading of the curvature photons.

On the other hand, Neronov et al. [156] argued that the models of acceleration of particles in dormant AGNs to the highest energies ($> 10^{20}$ eV), work well only for the most massive BHs (i.e., balancing the acceleration and the curvature losses terms in the equation of particle motion, one obtains that only black holes of masses $M \sim 10^{10}\mathrm{M}_{\odot}$ could accelerate the most energetic particles), which are rare. In that case the acceleration is accompanied by the electromagnetic emission with 2-3 orders of magnitude higher luminosity than the UHECR-luminosity of the source, which, in turn, would mean that the object is not dormant. They argued that this scenario can be recovered, if an inclination between the magnetic and rotational axes is within a few degrees. In that case the most energetic particles can be produced around less massive BHs ($\sim 10^{8}\mathrm{M}_{\odot}$), but, on the other hand, the magnetic field is required to be extremely very strong $\sim 10^{5}$ G, much above the current estimates. They showed that also the electromagnetic luminosity is decreased by misalignment so that it does not exceed a typical power output of AGNs in the local Universe.

The TeV emission was detected in many blazars. Those objects are special, however, because of strong Doppler boosting, which enhances observed radiation. The vacuum gap geometry, and, thus, its ability to accelerate particles, can be tested rather by examining non-blazar objects. If the acceleration is sufficiently efficient, misaligned, low-luminosity radio galaxies should be also detectable in the TeV band. To search for this emission from the non-blazar objects, Pedaletti et al. [162] analyzed VHE (HESS and Fermi) data for NGC 1399, which has a high-mass central black hole, low-luminosity jets (at all wavelengths), and it is located close enough to enable detection, if the emission is produced. However, there was no detection reported. They obtained the upper limit for the source luminosity at energies above 200 GeV $L < 9.6 \times 10^{40}$ erg s^{-1}. This result is also robust in the sense that there is no expected source of attenuation of the signal along the line of sight to an observer. Pedaletti et al. concluded that either only a small portion of the vacuum gap is available for the particle acceleration, and/or the charge density close to the black hole is much smaller than the Goldreich-Julian density (and, therefore, the fully developed vacuum gap exists), but additional production of pairs occurs due to absorption of inverse Compton upscattered photons at larger distances. Up to date, only a minor fraction of AGNs detected above 100 MeV are radio galaxies, the rest consisting of blazars, e.g., [176]. This fact may favor scenarios in which the highest energy emission originates from the relativistic jet rather than from the stationary gap, and the Doppler beaming makes blazars stronger TeV sources than radio galaxies.

It was proposed [32] that, in analogy to pulsar magnetospheres, vacuum gaps may be unstable to cascade pair production, and a plasma-filled magnetosphere can result instead. As will be discussed in detail later, in polar gap models of pulsar magnetospheres, such sparks, where a pair avalanche can be initiated, are located close to the stellar surface and primary particles for a cascade production are supplied directly from it. In the black hole case, location of vacuum gaps is only limited to be above the event horizon, possibly being even nonstationary [32]. Numerical investigations [201, 153] show that in analogy to the pulsar magnetospheres, also in the black hole vicinity the density of produced pairs may be high enough to screen out the gravitationally induced electric field, and pair production may proceed in bursts, when the sparks discharge. The production of plasma would be manifested by the appearance of relativistic outflows – highly magnetized plasma beams, launched in the form of jets. The energy that they carry is supposed

to come from the rotation of a black hole.

3.4 Force-free magnetosphere and Blandford-Znajek mechanism

Force-free (FF) electrodynamics is a massless limit of MHD, applicable when the electromagnetic stresses are completely dominant in the system, such that the plasma dynamics does not play a role in determining of the field configuration. In that case the inertial ($\rho = 0$), pressure, and gravitational forces are neglected [75]. The plasma provides only charges and currents, and the charge density necessary to satisfy the FF condition, i.e., screening out the electric field component along the magnetic field lines, is the equivalent of the Goldreich-Julian density in pulsars [32] (see also §5.1): $\rho = \nabla \cdot \boldsymbol{E}/4\pi \sim aB/(GM)^2$.

Clearly, FF electrodynamics is only the first approximation, and the relativistic MHD approach, which takes into account particle (in the sense of one-fluid) inertia, is more general.

The advantage of the FF approximation is that one can search for the electromagnetic field structure without invoking any plasma dynamics. Such a plasma-filled magnetosphere was considered by Blandford & Znajek in their seminal paper [32]. They proposed that the energy can be extracted from a rotating black hole in the same manner as it is extracted from a rotating pulsar. In the following we first summarize their result, then we discuss what was criticized about it and how the mechanism is understood today.

3.4.1 The Blandford-Znajek mechanism

To obtain a solution for the plasma-filled, highly magnetized magnetosphere, Blandford & Znajek used the covariant form of the FF condition $F_{\mu\nu}J^\nu = 0$, together with Maxwell equations. It was assumed to hold everywhere apart from the equatorial plane, where an accretion disk separates two magnetic hemispheres. This approach has several important implications: (1) from the 0th and 3rd component of the FF condition, a function $\Omega(r, \theta)$ can be defined, that was proved to be constant along each magnetic field line. BZ interpreted Ω as an electromagnetic angular velocity. Even though it is constant along a given field line, it may change from line to line. In general, it does not coincide with the angular velocity of the black hole, but depends on the global structure of the black hole magnetosphere. (2) The electrostatic potential A_t is also constant along each field line. (3) The poloidal field surfaces can be defined by $A_\phi = \text{const}$. A_ϕ plays a role of a stream function for the magnetic field, and the toroidal component of the field B_T was shown to be a function of A_ϕ only. (4) The magnetospheric current does not cross the poloidal field surfaces, thus it flows along them. This outflowing current has to be balanced by the inflowing current in the equatorial disc that supports the discontinuity in the toroidal field across the disk.

Thus, the solution for a magnetosphere is determined by the topology of the magnetic surfaces $A_\phi = \text{const}$, and all the relevant quantities can be expressed as functionals of A_ϕ. BZ obtained the final self-consistent equation governing A_ϕ, being in fact a generalization of the one obtained in the case of flat space by Scharlemann & Wagoner [180]. This fundamental equation was complemented by the boundary conditions: (1) for the field lines threading the equatorial disk, instead of the black hole horizon, the boundary condition was the continuity of the tangential electric field across the (conducting) disk. This implies $\Omega(A_\phi)$ equal to the angular velocity of the disk at the line footpoint. (2) For the lines threading the black hole horizon, the boundary condition was specified on its surface: it was the requirement that A_ϕ is finite and the famous Znajek boundary condition

$$B_\mathrm{T}[A_\phi(r_+, \theta)] = \frac{(r_+^2 + a^2)(\Omega - \Omega_H)}{r_+^2 + a^2 \cos^2\theta} \sin\theta A_{\phi;\theta}(r_+, \theta) \tag{3.75}$$

where $\Omega_H = a/(r_+^2 + a^2)$ is the angular velocity of the hole. As shown by Komissarov [106]

it is equivalent to the regularity condition (rather than a boundary condition) of a field at the horizon, not violating causality.[5] (3) For the field lines threading the black hole horizon, the boundary condition at infinity was also given: the solution has to match a known flat space solution – specifically, radial and paraboloidal topologies were considered.

With these conditions, an exact solution of the fundamental equation for A_ϕ was found, in the case $a = 0$, i.e., a generalization of the Michel's monopole magnetosphere, found earlier in pulsar related studies [149, 150]. A solution for $a \neq 0$ was obtained in the perturbation analysis with a small parameter $\epsilon = a/M$, such that the influence of the black hole spin on the poloidal field lines is small (BZ noted that it is not applicable in the pulsar case, because the poloidal lines change their topology dramatically when they open up due to the rotation). According to the boundary conditions at infinity, in the first case of the asymptotically the radial lines (i.e., the split monopole magnetic field), BZ obtained a constant angular velocity of field lines, given by $\Omega/\Omega_H = 0.5$. In the second case, a solution for the paraboloidal field lines was given, and the resulting angular velocity of the field lines was not uniform, changing from line to line $0.265 < \Omega/\Omega_H < 0.5$.

Such a configuration, with the currents flowing along the field lines that rotate more slowly than the black hole, was interpreted to extract the energy by braking of the black hole, similar as in the case of pulsars. The local ZAMO measures the velocity of a field line according to (3.19), which may be expressed as $v^\phi = (\Omega - \Omega_{\rm zamo})/\alpha$, and the energy flux that he measures (see also discussion in [106]) is

$$S^i = \epsilon^{ijk} E_j B_k \tag{3.76}$$

where the electric field is given by the MHD condition

$$E_i = -\epsilon_{ijk} v^j B^k \tag{3.77}$$

The poloidal component $\boldsymbol{S}_{\rm P} = S^r \boldsymbol{e}_r + S^\theta \boldsymbol{e}_\theta$ of this energy flux yields

$$\boldsymbol{S}_{\rm P} = -\frac{1}{\alpha}(\Omega - \Omega_{\rm zamo}) B_{\rm tor} \boldsymbol{B}_{\rm P} \tag{3.78}$$

where by $B_{\rm tor}$ we denoted B_ϕ measured by ZAMO. On the other hand, the poloidal component of the energy at infinity flux (i.e., the energy flux as seen by the observer at infinity)

$$\boldsymbol{S}_{\rm P\infty} = -\frac{1}{\alpha}\Omega B_{\rm tor} \boldsymbol{B}_{\rm P} \tag{3.79}$$

The fluxes flow along the poloidal surfaces, and cannot reverse on any given field line. The "radiation condition" at infinity defines the flow in (3.79) as being outward on all lines. In the ZAMO frame, on the other hand, there is the Poynting flux coming into the hole along the lines with $\Omega < \Omega_{\rm zamo}$, and also outgoing flux along the lines $\Omega > \Omega_{\rm zamo}$. At the event horizon $\Omega_{\rm zamo} = \Omega_{\rm H}$ ($\Omega_{\rm H}$ is the angular velocity of the horizon) implies that for all the lines in the magnetosphere the condition $0 \leq \Omega \leq \Omega_{\rm H}$ must hold.

BZ argued that the assumption about the FF magnetosphere at $r > r_+$ implies that the friction, responsible for the extraction of the hole energy, acts inside the horizon, where the electrical circuit between the outflowing current and that inflowing along the equatorial disk is completed, but by no-hair theorem the character of this friction cannot be exhibited outside. The closure of currents inside the horizon is possible because the FF condition, upon which particles move along the poloidal surfaces of constant A_t and A_ϕ, breaks down inside the horizon, since

[5] Formally, a boundary condition at the horizon is not the same as a regularity condition; the former applies to both steady-state and time-dependent solutions and is set on the boundary of the computational domain in order to select a particular solution; the latter applies only to the steady-state solutions, when one wants to find the one passing smoothly through the critical points at which the steady-state equations change their type – for discussion see, e.g., [38].

these surfaces muss cross the equator at a finite distance, and, therefore, become spacelike. Thus, the particles cannot follow them any longer. As a consequence, within the horizon the energy is transferred from the electromagnetic into the mechanical component.

Thorne et al. [197] developed this formulation in, so-called, the membrane paradigm. In it, the details of the physics close to horizon are neglected, regarded as a relic history of the black hole's past that do not have astrophysical importance. This frozen boundary-layer structure of particles and fields is in this sense a membrane that stretches the horizon. The stretched horizon looks from outside as endowed with the electric charge, currents and other properties that help to determine the physical conditions outside [197]. Braking of the black hole in this case is in a direct analogy to the pulsar case. This approach, however, was criticized by papers of Punsly & Coroniti [170] (an exhaustive summary is contained in the book of Punsly [169]), who argued that the horizon cannot not play any role in the energy extraction, because it is causally disconnected from the surroundings. Okamoto [157] developed the idea that instead of the event horizon, it is rather the "effective" ergosphere that allows the energy extraction by the magnetic field, in analogy with the Penrose process. Komissarov [108] argued that in fact the energy extraction is a result of more general phenomenon – energy counter-flow, and the Penrose process itself is a particular example of it.

3.4.2 Blandford-Znajek as a Penrose process

In the mechanical Penrose process the existence of the ergoregion (bounded by the ergosphere) is crucial. In the magnetosphere, rotating with respect to the black hole, the ergosphere is not the same as in the vacuum case, and is referred to as the effective ergosphere. The difference comes from the fact that in the rotating magnetosphere the null surface is replaced by two new null surfaces [152], which we call light cylinders, in analogy to pulsar magnetospheres.

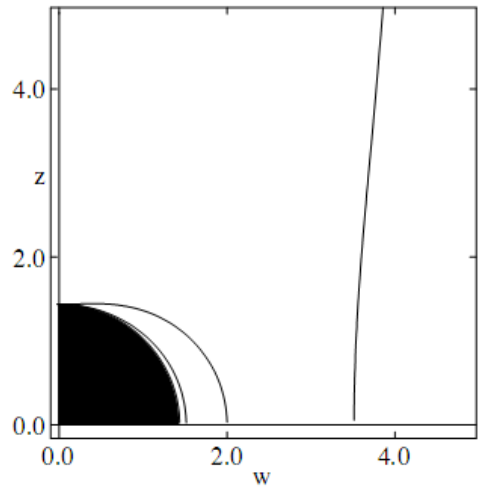

Figure 3.5: Black hole (black shading), light cylinders shown by thin lines, ergosphere shown by a thicker (middle) line, calculated for $\Omega = 0.7\Omega_{\rm H}$, $a = 0.9$. Taken from [106].

Consider a point of a field line, orbiting a black hole with a uniform angular velocity Ω, and 4-velocity $u^\mu = u^t(1, 0, 0, \Omega)$. 4-velocity of the point becomes null when [152, 106]

$$f(\Omega, r, \theta) \equiv g_{tt} + 2g_{t\phi}\Omega + g_{\phi\phi}\Omega^2 = 0 \qquad (3.80)$$

In the simplest case $\Omega = 0$ one gets $f = g_{tt} = 0$. Hence, the only light cylinder is the ergosphere. When $\Omega > 0$, the location of the inner light cylinder changes, but it always lies between the horizon and the ergosphere [106]. Moreover, in the case of $\Omega > 0$ also another light cylinder emerges from infinity. For large r it is given by

$$f(\Omega, r, \theta) = \Omega^2 r^2 \sin^2\theta - 1 \qquad (3.81)$$

$$= 0 \qquad (3.82)$$

This is the outer light cylinder, in analogy to the pulsar one, but modified by the gravity close to the equatorial plane. The geometry of null surfaces is shown in Fig. 3.5. The condition for subluminal rotation $f(\Omega, r, \theta) < 0$ implies that $\Omega_- < \Omega < \Omega_+$ [152], where

$$\Omega_\pm = \Omega_{\rm zamo} \pm \sqrt{\Omega_{\rm zamo}^2 - g_{tt}/g_{\phi\phi}} \qquad (3.83)$$

and the angular velocity of ZAMO is $\Omega_{\rm zamo} = -g_{t\phi}/g_{\phi\phi}$ (see Eq. 3.6). This means that only the lines that do not rotate too fast, or too slow, can be force-free. This is in a direct analogy with

the pulsar case, for which, beyond the light cylinder, the force-free condition breaks down, and the induced electric field cannot be screened on the lines that cross the light cylinders. As for the pulsars, in black hole magnetospheres the particles move outwards beyond the outer light cylinder, and they must move inwards into the black hole, when crossing the inner light cylinder [106]. The spark gaps where the plasma is created and the outflowing currents formed, must lie between these two surfaces, [32].

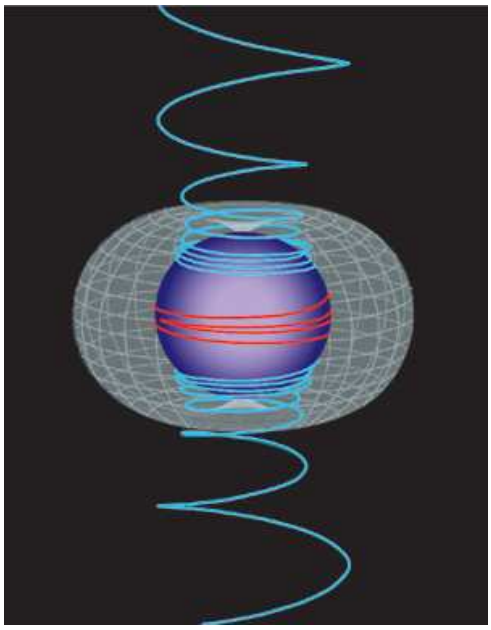

Figure 3.6: Twisting of magnetic field lines due to frame dragging in the ergosphere. Red lines show negative energy at infinity orbits. Simulations by [169].

The propagating outwards Poynting flux is a magnetic twist, launched beyond the light cylinder as it is in the pulsar magnetosphere. Originally Koide [105, 102] proposed that such a twist exerts a tension back onto the plasma and pushes the particles into negative energy at infinity orbits which brake the hole when plunging behind the horizon, exactly as in the mechanical Penrose process. However, the simulations by Komissarov [107] suggest that initially such hydrodynamic negative energy at infinity orbits indeed appear, but even when they disappear the BZ process still operates. Okamoto [157] defined the effective ergosphere by the condition $\Omega = \Omega_{\rm zamo}$. For the lines that rotate faster than ZAMO, $\Omega > \Omega_{\rm zamo}$, the fluxes $\boldsymbol{S}_{\rm P}$ and $\boldsymbol{S}_{\rm P\infty}$ flow in the same direction, and the Poynting flux propagates outwards when these lines cross the outer light cylinder. For the lines that rotate more slowly than ZAMO, $\Omega < \Omega_{\rm zamo}$, the fluxes flow in the opposite sense, when the lines cross the inner light cylinder. In analogy to the Penrose process, the incoming wind brakes the black hole, and the outflowing one extracts its energy. Komissarov [108] argued, however, that the domain of this energy counter-flow does not necessarily coincide with the negative energy at infinity domain, in particular, the wind separation surface $\Omega = \Omega_{\rm zamo}$ may be located outside the ergosphere, whereas the Penrose process can operate only inside the ergosphere. For that reason, he named the whole mechanism the energy counter-flow rather than the Penrose process.

3.4.3 Vacuum of a curved spacetime as an electromagnetically active medium

In the pulsar case, the physics of energy extraction is in analogy with the unipolar inductor, i.e., due to rotation of a conducting stellar surface with the anchored magnetic field, charges become redistributed, the electric field in the space is induced, and along the field lines that cross the light cylinder it cannot be screened out so that it drives a current that brakes the rotating conductor.

In the black hole case there is no conducting surface (like a stellar surface) to induce the electric field by the charge distribution. The curved spacetime itself behaves as an electromagnetically active medium, e.g., [108], in the sense that the electric field is induced even by the vacuum magnetic field in the vicinity of a rotating black hole (Wald's solution).

To see how the curved spacetime is electromagnetically active, we consider Maxwell equations in the ZAMO frame (3.40), (3.44), (3.45), (3.46). Given that $\tilde{\nabla}_i B^i = 0$ and also in Boyer-Lindquist coordinates $\tilde{\nabla}_i \beta^i = 0$, one can write

$$[\nabla \times (\boldsymbol{\beta} \times \boldsymbol{B})]^i = B^j \nabla_j \beta^i - \beta^j \nabla_j B^i = -\mathcal{L}_{\boldsymbol{\beta}} B^i \tag{3.84}$$

where we also used the fact that the covariant derivative of the Levi-Civita tensor vanishes. The Faraday law can be expressed as

$$\frac{\partial}{\partial t}\boldsymbol{B} + \nabla \times (\alpha \boldsymbol{E} + \boldsymbol{\beta} \times \boldsymbol{B}) = 0 \tag{3.85}$$

In analogy the Ampère law is

$$\frac{\partial}{\partial t}\boldsymbol{E} - \nabla \times (\alpha \boldsymbol{B} - \boldsymbol{\beta} \times \boldsymbol{E}) = -4\pi\alpha \boldsymbol{j} \tag{3.86}$$

Defining new quantities

$$\tilde{\boldsymbol{E}} = \alpha \boldsymbol{D} + \boldsymbol{\beta} \times \boldsymbol{B}, \qquad \boldsymbol{D} = \boldsymbol{E} \tag{3.87}$$

$$\boldsymbol{H} = \alpha \boldsymbol{B} - \boldsymbol{\beta} \times \boldsymbol{D}, \qquad \boldsymbol{B} = \boldsymbol{B} \tag{3.88}$$

one finds the Maxwell equations have the same form as those in an electromagnetically active media. This analogy was in fact first discussed by Landau & Lifshitz. In a special case of a constant gravitational field one gets $\boldsymbol{D} = \tilde{\boldsymbol{E}}/\alpha$, $\boldsymbol{B} = \boldsymbol{H}/\alpha$ as if the electric permittivity and magnetic permeability were $\varepsilon = \mu = 1/\alpha$.

3.4.4 Efficiency of the Blandford-Znajek process

In the BZ process the current driving battery is close to the black hole horizon. The power extracted in the astrophysical load (L) far from the black hole is given by [197]

$$\Delta P_{\rm L} = I^2 \Delta R_{\rm L} = \frac{U^2}{(\Delta R_H + \Delta R_L)^2} \Delta R_L \tag{3.89}$$

where $U = \Omega_{\rm H} \Delta\Phi / 2\pi$ is the potential difference created by the battery, $\Delta\Phi \sim B_{\rm n} \pi r_{\rm H}^2$ is the magnetic flux, $\Delta R_{\rm H}$ is the impedance between two magnetic surfaces on the horizon (denoted 1 and 2 in Fig. 3.7), and $\Delta R_{\rm L}$ is the impedance in the astrophysical load.

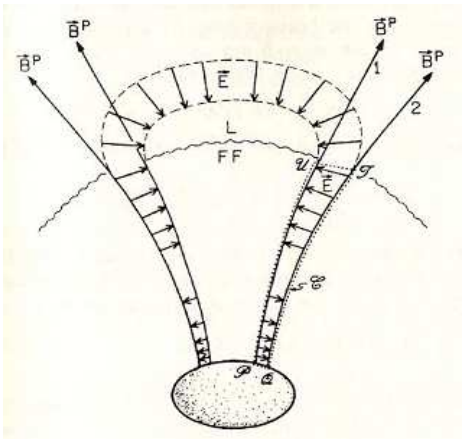

Figure 3.7: Black hole battery and the astrophysical load. From [197].

Since the circumference around the black hole is given by $2\pi\varpi = 2\pi\sqrt{g_{\phi\phi}}$ one can relate the part of it Δl between magnetic surfaces, to the whole circumference with the impedance of free space $R_{\rm H} = 4\pi = 377$ ohms

$$\Delta R_{\rm H} = R_{\rm H} \frac{\Delta l}{2\pi} \tag{3.90}$$

Moreover one can write for the magnetic flux difference between magnetic surfaces

$$\Delta\Phi = (2\pi\varpi \Delta l) B_{\rm n} \tag{3.91}$$

and thus

$$\Delta R_{\rm H} = R_{\rm H} \frac{\Delta\Phi}{4\pi^2 \varpi^2 B_{\rm n}} \tag{3.92}$$

Apart from this, since the same current driven by the battery flows through the load

$$\frac{\Delta R_{\rm L}}{\Delta R_{\rm H}} = \frac{U_{\rm L}}{U_{\rm H}} = \frac{\Omega}{\Omega_{\rm H} - \Omega} \tag{3.93}$$

since in the load the angular velocity is that of the field lines Ω, and for the horizon only it is calculated from $U - U_{\rm L}$, thus proportional to $\Omega_{\rm H} - \Omega$. One gets

$$\begin{aligned} \Delta P_{\rm L} &= \frac{\Omega(\Omega_{\rm H} - \Omega)}{4\pi} \varpi^2 B_{\rm n} \Delta\Phi \\ &\sim \frac{1}{128} \left(\frac{a}{M}\right)^2 B_{\rm n}^2 r_H^2 \sim 10^{43}\,{\rm erg\ s^{-1}} \left(\frac{a}{M}\right)^2 \left(\frac{M}{10^8 M_\odot}\right)^2 \left(\frac{B_{\rm n}}{10^4 {\rm G}}\right)^2 \end{aligned} \tag{3.94}$$

where in the last calculation we assumed $\Omega \sim \Omega_{\rm H}/2$, for which the mechanism has the highest efficiency.

Studies of Blandford-Znajek mechanism confirm that the mechanism can work efficiently in astrophysical conditions, but may require high values of the black hole spin [139]. Since it depends also on the magnetic field strength, advected by matter infalling from a disk, a kind of accretion is also of importance. The stronger the field is generated in the inner disk (and sustained against diffusion outwards), the stronger is its Maxwell pressure, which maintains the field close to the black hole. Given that geometrically thick, optically thin ADAF disks are plausibly able to support much stronger fields than radiatively efficient ones, BZ process can provide a significant fraction of the overall energy budget of low luminosity sources [11].

3.5 Astrophysical jets

3.5.1 Central engine – accreting black hole

The luminosity from the BZ mechanism competes with the luminosity of an accretion disk in a system. For the steady, spherical accretion the maximum luminosity is the Eddington one, determined by the balance between gravitational and radiation-pressure forces

$$G\frac{Mm_{\rm p}}{r^2} = \sigma_{\rm T} T^{01} \tag{3.95}$$

where $T^{01} = L_{\rm Edd}/4\pi r^2 c$ is the 01-component of the energy-momentum tensor of the radiation field (here, radial momentum flux), $m_{\rm p}$ is the proton mass; this implies

$$L_{\rm Edd} = \frac{4\pi GcMm_{\rm p}}{\sigma_{\rm T}} = 1.25\times 10^{46}\left(\frac{M}{10^8{\rm M}_\odot}\right){\rm erg\ s^{-1}} \tag{3.96}$$

To maintain this luminosity, the critical accretion rate is required

$$\dot{M}_{\rm Edd} = \frac{L_{\rm Edd}}{\eta c^2} \approx 2\left(\frac{M}{10^8{\rm M}_\odot}\right){\rm M_\odot yr^{-1}} \tag{3.97}$$

where $\eta \approx 0.1$ is a typical efficiency of conversion energy into radiation. The equipartition magnetic field at $r_{\rm g}$

$$\frac{B_{\rm eq}^2}{8\pi} = \frac{L}{4\pi r_{\rm g}^2 c} \tag{3.98}$$

have the upper Eddington limit for $\dot{M} = \dot{M}_{\rm Edd}$

$$B_{\rm eq} = \left(\frac{2L}{r_{\rm g}^2 c}\right)^{1/2} \approx 6\times 10^4 \left(\frac{\dot{M}}{\dot{M}_{\rm Edd}}\right)^{1/2}\left(\frac{10^8{\rm M}_\odot}{M}\right)^{1/2}{\rm G} \tag{3.99}$$

In the accretion disc the gas accreting onto the black hole may be shaped in various geometries, but the Bardeen-Petterson effect[6] should eventually drag it into the equatorial plane.

Power output of the BZ process (3.94) can compete with luminosity of the accretion, if the latter proceeds in a weak, sub-Eddington regime. As we mentioned, however, the role of an accretion disc is not only to launch a wind, in particular – a collimated disk jet, whose luminosity competes with the BZ jets, but also to provide environment that would be able to collimate the BZ jet, and to supply a magnetic field. This seems to go together – lower luminosity ADAF disks are able to supply stronger fields, and, what follows, in low-power sources the BZ process may account for the jet launching.

[6] At small radii, an accretion disk is driven into the equatorial plane of a rotating black hole, regardless of its initial inclination, due to a combination of gravitomagnetic forces and viscous forces in the disc.

However, as seen in (3.94), the Blandford-Znajek mechanism, even though efficient enough to play a role in BL Lac objects, cannot completely explain the power output of Flat Spectrum Radio Quasars (FSRQs). This suggests that two classes of AGNs are possible (see e.g. [38]): one class gets the luminosity from accretion (i.e., liberation of the gravitational energy of accreting matter), the other class – from rotation of a central black hole. In particular, FSRQs are energized by accretion at rates $\dot{M}/\dot{M}_{\rm Edd} \sim 1$ (which provides the luminosity $L \gtrsim 10^{46}$ erg s^{-1}), and BL Lacs with $\dot{M}/\dot{M}_{\rm Edd} \ll 1$, are powered by both the central black hole and the weak disk component, maintaining the overall luminosity $L \sim 10^{44}$ erg s^{-1}.

3.5.2 Disk jets

The process of launching jets from the disk was considered by Lovelace [131] and Blandford [29]. In these models, matter in the disk rotates with Keplerian velocity and drags along the magnetic field that threads the disk. This works as a unipolar inductor, and generates an electric field. Since the charges are presumably free to leave the disk, a current is driven along the magnetic field lines that act as wires. This process can account for the formation of the magnetosphere that satisfies the FF condition $\rho\boldsymbol{E} + \boldsymbol{j} \times \boldsymbol{B} \approx 0$. In it, each magnetic field line, anchored in the accretion disk, rotates rigidly with constant angular velocity of the matter in its footpoint. Near the light cylinder this corotation must cease, the FF approximation breaks down, and the retardation effects bend the field backwards. A magnetic twist propagates in a form of the wind, collimated by the toroidal field. The outflowing current exerts a torque on the disk, and Blandford showed that the field can be arranged so that the disk evolves in a stationary manner. The mechanism of braking of the disk is purely electromagnetic, and the energy and angular momentum are transported outwards as the Poynting flux.

This work was extended by Blandford & Payne (BP) in their seminal paper [31], where they went beyond the FF approach and included the particle inertia (MHD regime) in calculations. This inclusion of inertial effects allowed them to investigate the scenario of centrifugal acceleration of particles. To demonstrate explicitly that a magnetically focused jet outflow can be indeed established, they searched for self-similar solutions for cold, axisymmetric, ideal MHD flow from a rotating Keplerian disk, which, in analogy to a force-free problem of Blandford, was threaded by the magnetic field lines (see also [58]). Self-similar solutions are those for which all the physical quantities scale with the radial distance from the center (BP assumed particular scalings: velocity scales as the Keplerian one, the density scaling was given by the mass conservation in this spherical wind, and scaling of the magnetic field given by its relation to the Alfvén velocity, assumed to be scaled the same way as the wind velocity). In this solution, due to rotation, the lines wrap around the magnetic surfaces of constant magnetic flux. Their pressure causes the flow to accelerate along the rotational axis, and pinching yields collimation. Until the flow is inside the Alfvén surface the collimation is effective, because the the collimating force may be provided from the accretion disk (communication is possible through the Alfvén waves). Further BP identified two classes of solutions: (1) those which cross the FMS point at the finite distance, have paraboloidal streamlines and remain Poynting-flux dominated; (2) the second class includes those solutions that approach the FMS point asymptotically, collimate along the rotational axis, and are marginally kinetic-energy dominated. As most of the energy is extracted electromagnetically, a fraction of accreted matter that flows in a jet is small, and within the MHD description BP demonstrated explicitly that the cold, and initially starting from rest at the equatorial plane flow, can be centrifugally accelerated provided the angle between the disk and the poloidal component of the magnetic field is sufficiently small (less than $\pi/3$).

Also other self-similar solutions were investigated in the literature, with different scalings chosen, e.g., [47], and relativistic extensions of the BP model [127]. A different class of MHD outflows can be obtained from simplifications of the Grad-Shafranov equation. All these investigations show that disks and jets can be connected through the transfer of energy and angular

momentum, but, in reality, it is expected that such systems are far more complicated than the self-similar solutions given by the simplified models. In fact, the lunching of jets in the accreting systems, in which the jet acceleration and collimation can be supported by the wind from the disk, can be a universal mechanism for all accreting systems (including protostellar ones, accreting white dwarfs, neutron stars and black holes).

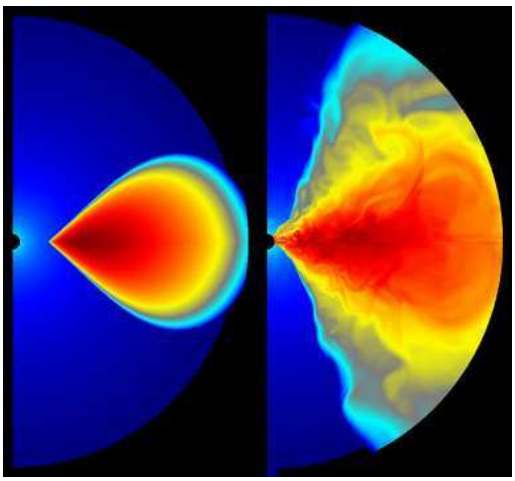

Figure 3.8: Formation of a low density funnel, which accreted matter does not penetrate. MHD simulations by [144].

Time-dependent general relativistic MHD simulations have been performed in 2D [104, 144] and also full 3D [143]. Porth & Fendt [168] performed simulations, in which the disk surface is prescribed as a boundary condition for the outflow, such that the study of how the disk conditions determine the outflow properties, becomes possible. This numerical analysis shows that the accreted matter does not penetrate the region close to the rotational axis of a central black hole, and a low density funnel in the polar regions of the black hole magnetosphere is formed. The reason is that due to the flux-freezing condition, the matter accreted onto the black hole cannot pass onto the magnetic field lines that thread the horizon, and, therefore, have no connection to the accretion disk.

From a theoretical point of view, "cleaning" of the magnetic field was investigated by [197]. They argued that the plasma that spirals down from the inner part of an accretion disk onto the hole, transports the magnetic field that is frozen into it, but as it falls down the hole, it becomes causally disconnected from the field. The field however is a subject to Maxwell pressure of the magnetic field in the black hole vicinity, and also in the inner disk. If the pressure of the transported field lines is smaller than that of the disk field, the plunging field lines are pushed onto the black hole neighborhood, and develop the ordered structure between the horizon and the disk.

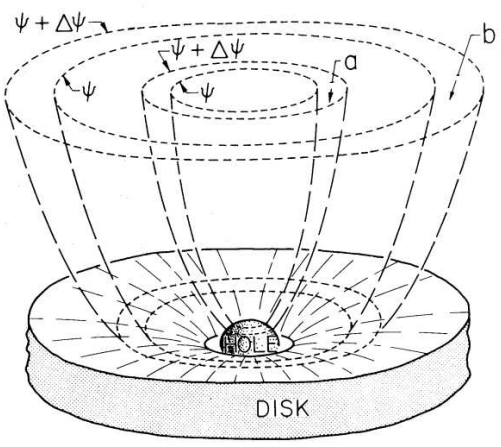

Figure 3.9: Sketch of a two-composite jet. Dashed lines show annular flux tubes (a intersects the hole, b – the accretion disk), characterized by the magnetic flux ψ, around which magnetic field lines wind. Taken from [137].

The model of a composite (stratified) jet was first proposed by Sol et al. [185] and also linked to the different launching mechanisms by Cavaliere & D'Elia [39]. This jet has the magnetospheric, highly Poynting-dominated core plus the hydromagnetic, dissipative component that emerges, when the accretion power increases, and the disk becomes radiation-pressure dominated. If the BZ mechanism operates in the black hole vicinity, the inner "spine" of the jet is possibly loaded with pairs produced in the black hole magnetosphere, and the rotational energy of a central hole is extracted according to the BZ mechanism. Such inner outflow is highly relativistic. On the other hand, the outer "sheath", i.e., more slowly moving counterpart launched from the accretion disk, consists of a proton-electron plasma from the accreting matter that flows along the magnetic field lines anchored in the disk.

The two-component model can account for the presence of the ultrarelativistic flow at parsec scales (indicated by apparent superluminal velocities from

VLBI observations), dominated by the fast component or a mixture of both, and a large-scale mildly-relativistic component from outer parts is dominates far from the source. In particular, if the jet was stratified, the inner highly relativistic spine would dominate the blazar emission, whereas radiation from radio galaxies, seen at larger viewing angles, would be dominated by the outer disk-jet.

3.5.3 Collimation and acceleration

Astrophysical jets are observed to propagate over very long distances, which may reach megaparsecs. Since the expanding plasma volume losses its energy adiabatically and radiatively very quickly, most of the jet energy must be accumulated in other forms, that slowly dissipate it over long lengthscales [109]. In the "standard model" most of the energy is in the Poynting flux, which converts to the kinetic energy and eventually dissipates at shocks. It is not clear, however, how and where the EM energy is transferred to the plasma, in order for the jet to have high Lorentz factor, low magnetization, and, thus, be able to dissipate at the shock.

The simplest possibility – radial MHD wind in a generic case does not convert the electromagnetic to the kinetic energy. In the nonrelativistic case, BP showed that this conversion is possible, since the organized magnetic field provides acceleration and collimation by the build-up of the toroidal component. However, this configuration seems to be prone to instabilities [82] so that may not be maintained to large distances. Moreover, the generalization to the relativistic case changes this picture: the inward pressure gradient of the magnetic lines almost exactly balances the outward tension force [133, 100]. After the flow has passed the fast magnetosonic point, it does not collimate any longer. Thus, if the flow is radial in the force-free region, it remains so further out [100]. This implies that in the relativistic case the acceleration at the expense of the magnetic energy depends strongly on the field geometry, and in the case of a radial flow, the magnetization remains large at long distances, making the flow unable to convert the energy to the particles. Therefore, in a relativistic, radial MHD wind it is difficult to envisage the production of a jet with high Lorentz factor and low magnetization.

To overcome this problem, the collimated flows were considered, which can increase the asymptotic Lorentz factor and decrease magnetization by the factor $\theta_{\rm jet}^{-2/3}$ (this is a jet asymptotic, half-opening angle). Causal contact across the flow demands that the faster it is, the smaller the opening angle should be, and thus the stronger collimation. The maximal angle $\theta_{\rm max} = 1/\Gamma \sim 1/\sigma_0$ seem to be consistent with observations of AGNs [171] (not for GRBs). Collimation, however, requires special boundary conditions [132, 135]. More specifically, in the ideal MHD description, transformation of the electromagnetic into the kinetic energy is possible only to the equipartition limit (which is still not the matter dominated limit); and even for this, however, there is the requirement that the flow is confined by the external pressure which does not diminish too fast with the distance. If it does so, the flow stops accelerating after reaching the terminal Lorentz factor, in general much smaller than the maximum possible one. What is even more important is that – since the acceleration in relativistic MHD proceeds very slowly due to the cancellation of the electric and Lorentz forces – this confining medium has to be present up to large distances. Thus, Lyubarsky [132] showed that jets cannot be completely matter-dominated without dissipation. On the other hand, the jets indeed are observed where the external pressure exists, e.g., winds from the outer parts of the disk in accreting systems.

Models, in which the magnetization remains high at large distances, were also proposed. In that case magnetic acceleration must be somehow enhanced, e.g., via nonaxisymmetric current-driven instabilities that randomize the magnetic field and transfer the energy from the slowly decaying transverse field component to the rapidly decaying longitudinal component [82]. Heinz & Begelman found that such chaotic magnetic field exhibits the acceleration $\Gamma \propto r$, the same as an ultrarelativistic gas with $\gamma = 4/3$. Thus, this magnetic mechanism would be able to provide acceleration as rapidly as the thermal mechanism. Instabilities can be also connected with

dissipation of the magnetic energy into plasma heating or kinetic energy in sideways expansion.

Contopoulos [46] suggested that magnetic acceleration is more efficient if it proceeds in the impulse, instead of a steady-state, manner. In the relativistic regime this idea was developed by Granot et al. [74]. They considered a discrete magnetized shell of width l_0, whose back is adjoined to a conducting "wall", and which expands into a vacuum in front of it. This expansion can be described as a rarefaction wave propagating into the shell towards the wall. The front of the shell moves away from the wall with relativistic velocity, because the particle inertia are negligible in the strongly magnetized shell and, therefore, the shell resembles an electromagnetic pulse. Quickly the rarefaction wave reaches the wall and the second, "reverse" rarefaction wave is launched behind the escaping front of the shell. Since both fronts propagate with relativistic speeds, their mutual distance changes very slowly. Between those fronts the fluid is accelerated by the pressure gradient of the magnetic field that was generated in the initial expansion. Moreover, behind the reverse rarefaction wavefront the fluid density and pressure are very low and therefore the shell can be regarded as separated from the wall. After the shell has lost causal contact with the wall, it keeps accelerating with time as $\Gamma \propto t^{1/3}$, and its width is approximately constant[7]. Eventually, when the kinetic energy becomes comparable to the magnetic energy, the acceleration ceases and the flow enters the coasting phase. At this point the Lorentz factor has its maximum value $\Gamma \sim \sigma_0$ and the flow is kinetically dominated. During coasting the shell width increases with time, while its magnetization decreases inversely proportional to time. However, Levinson [124] showed that in this mechanism acceleration is limited by interaction of high-σ shells with the ambient medium.

It appears, therefore, that it may be necessary to go beyond the ideal MHD approximation in order to understand the high Lorentz factors and collimation of jets. There is yet another big puzzle, revealed by observations of very rapid variability in blazars.

3.5.4 Extreme TeV variability in blazars

Blazars are variable at all wavelengths. The shortest timescales and the largest amplitudes of variability are in the VHE band. In some cases (PKS 2155-304, Mrk 501) the timescale of TeV flares is a few minutes [3, 5], and in Mrk 421 $\sim$ 20 minutes [60]. Since the supermassive black holes have masses $\sim 10^9 \mathrm{M}_\odot$, the light-crossing time of the black hole horizon is $t \sim r_\mathrm{g}/c = GM/c^3 = 1.4$ h, much longer than the variability timescale [23]. One possibility is that the observed fluctuations are generated by the small fraction of the black hole horizon, but there is no obvious source of characteristic scale smaller than r_g. It also demands high efficiency of the energy conversion into radiation [136]. Most of existing models concentrated on the possibility that the rapid variations are produced rather in a relativistically moving jet, and in this case, causality implies that the length (radius) l' of the emission region in the comoving frame satisfies [23]

$$l' < ct' = c\frac{t_\mathrm{obs}}{\Gamma(1-\boldsymbol{\beta}\cdot\boldsymbol{n})} \tag{3.100}$$

where $\boldsymbol{n}$ is the direction to the observer, $\boldsymbol{\beta}$ and Γ are the emitting region speed and Lorentz factor, respectively, t_obs is the variability timescale. Due to beaming, photons can reach the observer only when $\boldsymbol{\beta}$ is almost parallel to $\boldsymbol{n}$

$$1-\boldsymbol{\beta}\cdot\boldsymbol{n} \approx 1-\beta \approx \frac{1}{2\Gamma^2} \tag{3.101}$$

[7]It is interesting to show how this effect is explained by Granot et al. They use the analogy to two masses m connected by a compressed spring with potential energy E_pot in the comoving frame. In this frame the total energy is $E' = 2mc^2 + E_\mathrm{pot}$, and in the lab frame $E = \Gamma E'$. When the spring energy is released, it goes into the kinetic energy of the masses, which in the comoving frame achieve Lorentz factors $\Gamma_* = 1 + E_\mathrm{pot}/2mc^2$ and velocities $u'^\mu_\pm = \Gamma_*(1, \pm\beta_*, 0, 0)$. This implies that in the lab frame $u^\mu_\pm = \Gamma\Gamma_*(1 \pm \beta\beta_*, \beta \pm \beta_*, 0, 0)$. Thus, for Γ, $\Gamma_* \gg 1$ one gets $E_-/E_+ \approx (1/\Gamma^2 + 1/\Gamma_*^2)/4 \ll 1$, i.e. as seen in the lab frame, almost entire energy released by the spring goes into a leading mass. E_pot in the model is the shell magnetic energy.

and then one obtains that

$$l' \lesssim ct_{\rm obs}\Gamma \tag{3.102}$$

For PKS 2155-304 the mass of a central black hole $M \sim 10^9 {\rm M}_\odot$ [3] implies approximately $\Gamma > 30(l'/r_g)$, where $l' > r_{\rm g}$. Observations of the proper motion of the jet knots allow to directly measure the Lorentz factor of the flow. Those are mainly VLBA radio measurements of apparent superluminal speeds $\beta_{\rm a} = \beta \sin\theta/(1-\beta\cos\theta)$. Results from the MOJAVE survey of highly-beamed radio-loud AGNs indicate $\Gamma \sim 10$ with a tail extending up to $\Gamma \sim 50$ [128].

On the other hand, rapid VHE variability implies much higher values, for several reasons [23]:

(1) ability of electrons to cool efficiently within the required timescale. γ-rays can be produced in the jet due to inverse Compton scattering of synchrotron and also external photons [23]. Begelman et al. [23] argued that constraints on radiative efficiency rather exclude the synchrotron self-Compton (SSC) mechanism for flares. The reason they gave was that the homogeneous SSC model of Comptonization of the synchrotron spectrum, requires $\Gamma \gtrsim 50$ for the γ-ray peak, i.e. the bulk Lorentz factor of the flow has to be high. The cooling timescale of high energy electrons is however longer for higher Γ, since $t_{\rm ic} \sim \gamma/\dot{\gamma}$, and the energy density of photons, which appears in $\dot{\gamma}$ is boosted by a factor $\sim \Gamma^2$. For the fast variability (i.e., very short cooling timescale) this places an upper limit $\Gamma \lesssim 40$ [23]. However, the requirement of high Lorentz factor in the homogeneous SSC models can be alleviated in the decelerating jet model [63]. If the jet continuously decelerates, fast electrons in the jet spine see the photons from the slow sheath as beamed, and upscatter them in the IC process to the TeV range, without a need to invoke high bulk Lorentz factors. Model with initial $\Gamma \sim 15$ to final $\Gamma \sim 4$ well reproduces the existing data.

Begelman et al. [23] argued that, instead of SSC, the external Compton (EC) scattering may be rather of importance, since the conditions on radiative efficiency can be relaxed. In that case the energy density in the ambient photon field must exceed that of the synchrotron photons. The external emission should be in submillimeter band if it is isotropic. In contrast to the SSC, cooling of electrons in EC mechanism is more efficient with larger Γ. In particular, such submillimeter nonthermal radiation could be produced in the radiatively inefficient accretion flows (RIAF) that can be present in blazars, or as a thermal emission from outer, cool parts of the accretion disc, or as emission of electrons in the outer shear layer of a jet.

(2) low opacity such that TeV photons can escape from the flaring region without producing pairs in scattering on soft photons in that region. It places a lower limit on the bulk Lorentz factors, depending, however, on the character of target photons, i.e., whether they are synchrotron, or rather external in origin [23]. If synchrotron photons dominate the energy density in the flaring region, the condition of low opacity $\tau_{\gamma\gamma} \leq 1$ implies Lorentz factors $\Gamma \gtrsim 50$, provided that the synchrotron emission comes from the same region as the TeV photons (if VHE photons pass through other radiating regions, probability of their absorption increases). If the external photon fields are present, flaring activity could be produced in external Comptonization rather than synchrotron process – but only out to a radius of several hundred $r_{\rm g}$ if $\Gamma \sim 50$ (although higher values would allow flares at larger distances) [23].

(3) emitting region travels to parsec scales before the radiation occurs, since otherwise the TeV photons would be absorbed in the accretion flow (e.g. [64]).

The discrepancy of these constraints with VLBI measurements poses a challenge for emission models, and is known as "blazar's bulk Lorentz factor crisis". [23] argued, however, that the radio and gamma-ray producing regions may have different properties, so, in fact, they do not have to be necessarily associated with the same Lorentz factor. In particular, it was proposed that a jet may decelerate on scales $\sim 10^2 - 10^3 r_{\rm g}$, where the local dissipation, responsible for the TeV photons, occurs [123].

To explain TeV rapid flaring many models were investigated:

(1) "needles" in a jet [65] – a compact and active region moves in a larger jet with much

higher Lorentz factor. The entire jet is responsible for the persistent emission, and the needle accounts for the very rapid variations. Such a needle could be an anisotropic electron beam directed along the jet [66]. Variable emission is produced by the IC scattering of relativistically streaming particles along the magnetic field in the jet. Occasionally these particles with small pitch angles point towards the observer which results in the flaring event. As they have very small pitch angles, there is very little synchrotron emission and resulting TeV flare is "orphan". Such beams were argued to be produced in the magneto-centrifugal acceleration scenario.

(2) misaligned minijets inside a jet [68] – compact high Lorentz factor emitting regions move relativistically within the jet of a bulk Lorentz factor $\Gamma \sim 10$, which is implied by the VLBA, sub-pc jet observations. Those emitting regions have origin in reconnection sites, where the magnetic energy of a Poynting-dominated global flow is dissipated, and a plasma accelerated to local, high Lorentz factors. TeV flares are produced through SSC process. There is also the simultaneous synchrotron X-ray emission, which potentially distinguish this model from the needle-in-a-jet one.

(3) interaction with the star [19] – flares are produced when a red giant crosses the jet close to its launching site. The stellar envelope becomes fragmentated into the compact magnetized blobs, which are accelerated, and radiate γ-rays through the proton synchrotron, or EC scattering of electrons.

(4) firehose instability [188] – the instability develops due to the pressure anisotropy in the jet: the parallel pressure exceeds the perpendicular one, as a result of the bulk jet streaming. When the instability develops, it causes the disruptions in the jet structure that, in turn, may produce the variability in the observed emission. The characteristic growth rate is on the order of several minutes, which could explain the measured variability timescales in blazars.

A quite different idea, in the case of PKS 2155-305, was investigated by Rieger & Volpe [177]. They argued that the system can consist of a binary black hole with the more and also the less massive object. The latter is responsible for the flare, and the variability timescale is consistent with the light crossing time of its horizon.

Recent observations reveal that the very rapid TeV variability exists in both subclasses of blazars, BL Lacs and FSRQs. Dense external photon fields that are thought to exist in the vicinity of quasars suggest that the TeV variable emission occurs at large distances from the central objects, such that the TeV photons are able to escape not attenuated by pair production in $\gamma\gamma$ scattering on the soft radiation. In all the cases, for both BL Lacs and quasars, the flares show that the flux variations are large-amplitude. This suggests that the whole emitting region contributes to the flares [155].

In the following we propose a different model of the rapid variability in blazars. In it, the particle emission is modulated by the large-amplitude magnetic twist, launched together with a relativistically outflowing plasma from the polar region of a black hole. The radial dimension is a wavelength that constrains the variability scale – in fact, much smaller than the gravitational radius. A candidate for a source of such small-wavelength, large-amplitude fluctuations can be the vacuum gap above the polar regions of the central black hole. Both theoretical and numerical investigations show that it may be highly nonstationary in nature. In particular, Sturrock [187] argued that in the pulsar magnetospheres a steady state pair flow is not possible and that pairs escape in sequential charge sheets. In his model the flow is oscillatory, with a pattern resembling that of an oscillating diode. Shibata et al. [182] argued that models of stationary pair flow that screens out the parallel electric field just above the pair formation front require extremely large pair multiplicities, which cannot be realized around pulsars. Levinson et al. [126] considered a scenario in which bursts of pair creation in pulsar and black hole magnetospheres result from the large-amplitude electrostatic oscillations of the unscreened gap electric field. Specifically, the accelerated primary electrons produce pairs at the pair formation front, from which positrons are accelerated back and create a second pair formation front, from which electrons again are accelerated and enhance the primary electron beam. They argue that the fine-tuning is needed for

this process to screen out the parallel electric field, and in a generic case the oscillatory behavior sets up. This nonstationary nature of the gap discharges can be a source of short-timescale ($< r_{\rm g}/c$) variability in the outflow.

Chapter 4

Subluminal waves in blazar jets

In this chapter we present our model of ultra-fast variability of TeV gamma-ray flux from blazars. The timescales of the fluctuations, on the order of several minutes, imply the presence of structures much smaller than the black hole gravitational radius that modulate the entire flux reaching the observer. In our scenario these structures are associated with the wavelength of a nonlinear, large-amplitude wave that is launched together with a plasma from a black hole magnetosphere, and propagates relativistically as a Poynting-flux dominated jet.

First, in Sect. 4.1 we introduce parameters that describe the physical conditions in the magnetized outflows, familiar from pulsar related studies. Further, in 4.2, we specify the two-fluid model of a pair plasma, coupled to Maxwell equations, which we further solve in Sect. 4.3, using a perturbation analysis. As a small parameter we choose the ratio of a wavelength to the actual radius at which the wave is probed. In the lowest order the solution is a subluminal, magnetic shear, that can be regarded as a large-amplitude, circularly polarized Alfvén wave. However, given that the wave is considered at large distances, the radial component of the magnetic field originating from the central object, is negligible, and a shear propagates without a background field (i.e., phase averages of the fields vanish). The wave properties become slowly modified by the lateral expansion. Thus, in the first order of the perturbation calculation we get the radial evolution of all the wave quantities. Our results show that this configuration effectively accelerates particles at parsec scales. The pre-existing nonthermal emission of these particles can be modulated, and we show that the fluctuations are not filtered out by the propagation effects, provided the pair loading in a black hole magnetosphere is sufficiently low. This suggests that the extremely rapid variability of the very high energy flux is confined to the sources that do not exhibit prolific pair production, and, presumably, are able to sustain vacuum gaps in their magnetospheres.

This chapter is based on work published in the Astrophys. J. [101].

4.1 Parameters

We specify the physical conditions in the pair-dominated, magnetized outflow via three dimensionless parameters:

(1) The nonlinearity or strength parameter a is a dimensionless measure of the energy-flux density (for details see Sect. 5.2.2). For a circularly polarized vacuum electromagnetic wave of frequency $\omega/2\pi$ and electric field E, the strength parameter is conventionally defined as $a = eE/(mc\omega)$, and measures the Lorentz factor that an electron would achieve if it were accelerated from rest over a distance of $(2\pi)^{-1}$ times one wavelength in the field E. Assuming radial propagation, the corresponding luminosity is

$$L = \frac{m^2 c^3 \omega^2 a^2 \Omega_s r^2}{4\pi e^2} \tag{4.1}$$

and we use this expression to define a for a general (non-vacuum) wave. In the absence of radiation losses, $a \propto r^{-1}$, and is determined by specifying its value at some fiducial radius. For this we chose $r_0 = c/\omega$, although our treatment is, of course, valid only for $r \gg r_0$ and we certainly do not expect radial flow to extend to such small radii. With this choice, a_0 is independent of ω:

$$a = a_0 \, (r_0/r) \tag{4.2}$$

$$\begin{aligned} a_0 &= \left[\frac{4\pi e^2 L}{m^2 c^5 \Omega_{\rm s}} \right]^{1/2} \\ &= 3.4 \times 10^{14} L_{46}^{1/2} \end{aligned} \tag{4.3}$$

where $L_{46} = (4\pi/\Omega_{\rm s})\, L/\left(10^{46}\,{\rm erg/s}\right)$ is the "isotropic" or "4π" luminosity of the jet, scaled appropriately. The energy *radiated* per unit solid angle by a jet is directly measurable if the distance to the object is known. For the rapidly variable gamma-ray flare of PKS 2155-304, it corresponds to an isotropic luminosity of roughly $10^{46}\,{\rm erg/s}$, so that, for this object, $L_{46} \gtrsim 1$.

(2) The mass-loading of the wind is conventionally described by the μ-parameter introduced by [148]:

$$\mu = L/\dot{M}c^2 \tag{4.4}$$

In the case of an electron-positron jet, μ denotes the Lorentz factor each particle would have if the entire luminosity was carried by a cold, unmagnetized flow. It is constant in those parts of the jet in which pair creation and radiation losses can be neglected.

(3) The magnetization parameter σ describes the ratio of the energy flux carried by electromagnetic fields to that carried by particles. For monoenergetic electrons and positrons of Lorentz factor γ,

$$\sigma = (\mu/\gamma) - 1 \ . \tag{4.5}$$

In a cold, non-accelerating, ideal MHD flow, σ is constant (assuming pair creation and radiation losses are negligible). However, as we show below, σ is not constant in charge-starved jets, even in the absence of dissipation. For this reason, we specify its value at the "launching" radius, inside of which the ideal MHD approximation is assumed to hold, and denote this quantity by σ_0, even though the region of constant σ is unlikely to extend to radii as small as $r \sim c/\omega$. The particle Lorentz factor at the launching point is then

$$\gamma_0 = \mu/\left(\sigma_0 + 1\right) \ . \tag{4.6}$$

The mass-loading parameter μ is determined by the physics of the pair-production cascade close to the black hole. A more intuitive measure, therefore, is the pair multiplicity κ, which relates the pair (proper) number density $n_\pm$ to the number density of electrons (or positrons) needed to screen out the (magnetic-)field-aligned component of the rotation-induced electric field. Adopting the definition conventionally used in pulsar physics, but replacing the angular velocity of the neutron star by $c/r_{\rm g}$ gives (e.g. [133])

$$\kappa = \gamma_\pm n_\pm \left(\frac{B}{2\pi e r_{\rm g}} \right)^{-1} \ , \tag{4.7}$$

where $\gamma_\pm$ is the Lorentz factor of the fluids. In the inner regions of the flows we consider, where $\sigma = \sigma_0 \gg 1$, the fluids move non-relativistically in the wave frame, so that $\kappa \approx a/\left(4\mu\right)$. Thus, in the absence of radiation losses and pair production, $\kappa \propto r^{-1}$ in this region. Physically, it is the value of κ at the outer boundary of the pair-production region that is most relevant. This is thought to be close to the black hole, but its precise location is unknown. In the following, therefore, we specify κ by its value $\kappa_{r_{\rm g}}$ at $r = r_{\rm g}$:

$$\kappa_{r_{\rm g}} \approx \frac{a_0}{4\mu} \left(\frac{c}{\omega r_{\rm g}} \right) \ . \tag{4.8}$$

4.2 The model

As we mentioned, the simplest model of an electron-positron plasma that takes account for the finite inertia of the charge-carriers is that of two cold, charged fluids (− denotes the electrons, whereas + stands for positrons). Such model, embedded in Kerr geometry, was developed in Khanna [96] and Koide [103]. Following this approach, we formulate the Euler equations for these fluids, coupled to the Maxwell equations, and we search for solutions that describe large-amplitude waves propagating radially from a magnetosphere of a rotating black hole. To keep the analysis tractable analytically, we consider only purely transverse, circularly polarized waves, for which also the phase-averaged electric and magnetic fields vanish. As discussed in 2.2.2, in this case fluids have equal number densities $n_+ = n_- = n$, equal radial velocities $v_{\parallel +} = v_{\parallel -} = v_\parallel$ and the meridional and azimuthal components of the fluid velocities are equal in magnitude but of opposite sign $v_{\perp +} = -v_{\perp -}$. Thus, fluids have also equal Lorentz factors

$$\gamma_+ = \gamma_- = \gamma = \left(1 - v_\parallel^2 - v_{\perp +}^2\right)^{-1/2} \tag{4.9}$$

The radial component of the four-velocity we denote by a dimensionless, parallel momentum $p_\parallel = \gamma v_\parallel / c$, and the transverse component this four-velocity by a dimensionless, perpendicular momentum $p_\perp = \pm \gamma v_{\perp \pm}/c$. Circularly polarized fields of a wave are described by complex quantities $E = E_{\hat{\theta}} + iE_{\hat{\phi}}$ and $B = B_{\hat{\theta}} + iB_{\hat{\phi}}$.

In the following we derive the continuity equation, the equations of motion of the fluids and the two relevant Maxwell equations (Faraday's law and Ampère's law) in the small-wavelength approximation, $r \gg c/\omega$, where ω is the wave frequency, using formulation in the ZAMO frame, outlined in 3.1.2. In the lowest order, large-amplitude plane-wave solutions are given by those discussed in 2.2.2.

4.3 Multiple-scale perturbation calculation

A self-consistent, nonlinear solution of two-fluid and Maxwell equations was carried out by Akhiezer & Polovin [4], and subsequently developed in the literature [140, 142, 42, 93]. It is based on the multiple-scale perturbation analysis.

In the astrophysical context, waves emitted from a central, compact object propagate with large amplitudes and at large distances, their characteristics become modified by the lateral expansion. Thus, there are two relevant scales in the problem:

(1) short one described by a "fast" phase variable ϕ

(2) long one determined by a "slow" radial coordinate $\rho = \epsilon r$, where ϵ is a small parameter.

The independent variables (t, r) are transformed into the new ones (ϕ, ρ), and also space and time derivatives are transformed into the derivatives of the new variables. In the lowest order in ϵ the space and time derivatives are given only in terms of $\partial/\partial\phi$. Thus, the relevant equations give the known plane wave solution.

However, the plane wave description is valid only at distances large compared to the wavelength, and large compared to the launching point. Close to this point lateral extend of a wave is possibly comparable to its wavelength, and plane waves must be invalidated. Thus, we assume that the waves are probed at a large radius, and we employ the short-wavelength approximation $r \gg c/\omega$, where ω is the wave frequency. This defines the small parameter of the problem $\epsilon = c/(\omega r) \ll 1$. The characteristic scale, on which the wave properties are modified, is determined by a slow radial coordinate $\rho = \epsilon r$. The expansion of the governing equations in the small parameter, in the first order gives the slow radial evolution of the phase-averaged plane-wave quantities.

Here we assume that the gravitational radius is of the same order in ϵ as the wavelength. We set $G = c = 1$, so that the black-hole mass $M \sim 1/\omega \sim \epsilon r$. As measured by a locally

nonrotating observer the fluid 3-velocities and Lorentz factors, and the electric and magnetic fields are denoted by $\boldsymbol{v}_{\pm}$, $\gamma_{\pm}$, and $\boldsymbol{E}$ and $\boldsymbol{B}$, respectively. Here we omit a "tilde" over the spatial differential operators $\tilde{\nabla}$, but, whenever they appear, should be understood as acting on 3D hypersurfaces, described by the metric $\tilde{g}_{ij}$. The wave speed is now denoted by $\beta_{\rm w}$, and β we reserve for the shift function.

In the two fluid model the continuity equation (3.47) reads (Eq. 22 in [96]))

$$\left(\partial_t - \boldsymbol{\beta}\cdot\nabla\right) n_{\pm}\gamma_{\pm} + \nabla\cdot\left(\alpha n_{\pm}\gamma_{\pm}\boldsymbol{v}_{\pm}\right) = 0 \ , \tag{4.10}$$

As before α is the lapse function and $\boldsymbol{\beta}$ is the shift vector. Lapse function determines the change between the local ZAMO time τ and the coordinate time t, i.e. $\alpha = d\tau/dt$, whereas $\boldsymbol{\beta}$ is interpreted as ZAMO 3-velocity with respect to the distant stars.

Since our fluids are cold and collisionless, the momentum conservation is given by the equations of motion for each fluid, but now, to equation (3.28) in §3.1.2 we add also a Lorentz force

$$\frac{1}{\alpha}\frac{\partial}{\partial t}p^i_{\pm} + \left(\boldsymbol{v}_{\pm} - \frac{\boldsymbol{\beta}}{\alpha}\right)\cdot\nabla p^i_{\pm} = \gamma_{\pm}g^i + H^i_j p^j_{\pm} \pm \frac{e}{m}\left(E^i + \epsilon^{ijk}v_{j\pm}B_k\right) \tag{4.11}$$

Faraday's law (3.44) and Ampère's law (3.46) are, respectively

$$\nabla\times\left(\alpha\boldsymbol{E}\right) = -\left(\partial_t - \mathcal{L}_{\boldsymbol{\beta}}\right)\boldsymbol{B} \tag{4.12}$$

$$\nabla\times\left(\alpha\boldsymbol{B}\right) = \left(\partial_t - \mathcal{L}_{\boldsymbol{\beta}}\right)\boldsymbol{E} + 4\pi\alpha e\left(n_+\boldsymbol{p}_+ - n_-\boldsymbol{p}_-\right) \ , \tag{4.13}$$

where, as before, $\mathcal{L}_{\boldsymbol{\beta}}$ is a Lie derivative along $\boldsymbol{\beta}$:

$$\mathcal{L}_{\boldsymbol{\beta}}\boldsymbol{E} = \left(\boldsymbol{\beta}\cdot\nabla\right)\boldsymbol{E} - \left(\boldsymbol{E}\cdot\nabla\right)\boldsymbol{\beta} \ . \tag{4.14}$$

Now we assume that the waves propagate radially so that the field and fluid variables depend only on t and r. The fast variable is the wave phase ϕ, a function of t and r that depends on the (as yet unspecified) wave phase velocity $\beta_{\rm w}(r)$, which is a function of r alone. The phase of an outwardly propagating vacuum wave in Kerr geometry is

$$\phi_{\rm vac} = \omega\left(t - \frac{r_*}{c\beta_{\rm w}}\right) \tag{4.15}$$

where

$$r_* = \int^r \frac{r'^2 + a^2}{r'^2 - 2Mr' + a^2}\mathrm{d}r' \ , \tag{4.16}$$

a is the Kerr parameter, and ω is the wave frequency measured by an observer at infinity (e.g. [197], Eq. 8.66). In analogy with this expression we write the phase of the nonlinear wave as

$$\phi = \omega\left(t - \int^r \frac{r'^2 + a^2}{\left(r'^2 - 2Mr' + a^2\right)\beta_{\rm w}(r')}\mathrm{d}r'\right) \ . \tag{4.17}$$

Transforming the independent variables in (4.10–4.13) from (t, r) into (ϕ, ρ), where $\rho = \epsilon r$, we now expand in the small parameter ϵ, assuming $\rho \sim r_{\rm g}$. Keeping terms of zeroth and first order, the derivatives are replaced according to

$$\frac{\partial}{\partial t} \ \rightarrow \ \omega\frac{\partial}{\partial\phi} \tag{4.18}$$

$$\begin{aligned}\frac{\partial}{\partial r} \ &\rightarrow \ \frac{\partial\rho}{\partial r}\frac{\partial}{\partial\rho} + \frac{\partial\phi}{\partial r}\frac{\partial}{\partial\phi} \\ &= \ \epsilon\frac{\partial}{\partial\rho} - \left(1 + \epsilon\frac{2M}{\rho}\right)\frac{\omega}{\beta_{\rm w}}\frac{\partial}{\partial\phi}\end{aligned} \tag{4.19}$$

$$\frac{\partial}{\partial t} + \left(\alpha\boldsymbol{v}_{\pm} - \boldsymbol{\beta}\right)\cdot\nabla \ \rightarrow \ \epsilon v_{\parallel\pm}\frac{\partial}{\partial\rho} + \omega\left(1 - \frac{v_{\parallel\pm}}{\beta_{\rm w}}\right)\frac{\partial}{\partial\phi} \ . \tag{4.20}$$

Expanding the dependent variables according to

$$p_{\parallel} = p_{\parallel}^{(0)} + \epsilon p_{\parallel}^{(1)} \tag{4.21}$$

etc., one finds the zeroth-order equations are those of continuity:

$$\omega \frac{\partial}{\partial \phi}\left(n^{(0)}\Delta^{(0)}\right) = 0 \ , \tag{4.22}$$

Faraday's and Ampère's laws:

$$-\frac{\omega}{\beta_{\rm w}}\frac{\partial E^{(0)}}{\partial \phi} - i\omega \frac{\partial B^{(0)}}{\partial \phi} = 0 \tag{4.23}$$

$$-\frac{\omega}{\beta_{\rm w}}\frac{\partial B^{(0)}}{\partial \phi} + i\omega \frac{\partial E^{(0)}}{\partial \phi} + i8\pi e n^{(0)} p_{\perp}^{(0)} = 0 \ , \tag{4.24}$$

and momentum/energy conservation:

$$\omega \Delta^{(0)} \frac{\partial p_{\parallel}^{(0)}}{\partial \phi} + \frac{e}{m}{\rm Im}\left(p_{\perp}^{(0)} B^{(0)*}\right) = 0 \tag{4.25}$$

$$\omega \Delta^{(0)} \frac{\partial p_{\perp}^{(0)}}{\partial \phi} - \frac{e}{m}\left(\gamma^{(0)} E^{(0)} + i p_{\parallel}^{(0)} B^{(0)}\right) = 0 \tag{4.26}$$

$$\omega \Delta^{(0)} \frac{\partial \gamma^{(0)}}{\partial \phi} - \frac{e}{m}{\rm Re}\left(p_{\perp}^{(0)} E^{(0)*}\right) = 0 \ , \tag{4.27}$$

where $\Delta = \gamma - p_{\parallel}/\beta_{\rm w}$. Solutions to these equations can be found with superluminal phase speed, $\beta_{\rm w} > 1$, but these waves do not propagate close to the black hole [97]. Here, we concentrate on subluminal waves. As remarked, a general solution can be found with a large-scale, constant magnetic field in the direction of a wave propagation [43]. However, we consider waves already at large distances $r \gg c/\omega$, where the magnetic field originating from the central object is weak, diminishing as $1/r^2$. Thus, we concentrate on the case of vanishing phase-averaged fields, and this implies that for the solutions the condition $\Delta = 0$ holds.

4.3.1 Lowest order solution: nonlinear waves

In the lowest order a solution with subluminal speed $\beta_{\rm w} < 1$ is that of a plane wave, derived in 2.2.2. It describes the monochromatic wave, in which

$$B = iE/\beta_{\rm w} \tag{4.28}$$

and, since the phase-averaged fields vanish, $\Delta = 0$ implies that the particles are in resonance with the wave, i.e., the radial components of the fluid velocities equal the phase velocity of the wave. Viewed from a frame that moves radially with speed $\beta_{\rm w}$, the electric field vanishes, and the wave is simply a static magnetic field of constant magnitude, whose direction rotates through 2π radians over one wavelength. The rate at which the B-vector rotates is arbitrary, being determined by the dependence of the fluid density n on phase. At each point, the current and, hence $p_{\perp}$, is parallel to the magnetic field to zeroth order. Thus, to this order, the forces exerted on the fluids by the fields vanish. We select the simplest case, where n, $|B|^2$ and $|p_{\perp}|^2$ are all constant and the wave is a monochromatic magnetic shear: $B \propto p_{\perp} \propto {\rm e}^{\pm i\phi}$.

4.3.2 First order solution

Our lowest order solution has $\Delta^{(0)} = 0$, and $|B^{(0)}|^2$, $|E^{(0)}|^2$, $|p_\perp^{(0)}|^2$, $p_\parallel^{(0)}$ and $n^{(0)}$ all independent of ϕ. Taking account of this, the first-order equation of continuity is:

$$\omega\frac{\partial}{\partial\phi}\left(n^{(0)}\Delta^{(1)} + n^{(1)}\Delta^{(0)}\right) + \frac{1}{\rho^2}\frac{\partial}{\partial\rho}\left(\rho^2 n^{(0)}p_\parallel^{(0)}\right) + \frac{1}{\rho\sin\theta}\frac{\partial}{\partial\theta}\left(\sin\theta n^{(0)}p_{\hat\theta}^{(0)}\right) + \frac{1}{\rho\sin\theta}\frac{\partial}{\partial\varphi}\left(n^{(0)}p_{\hat\varphi}^{(0)}\right) = 0 \ , \quad (4.29)$$

Faraday's and Ampère's laws are:

$$-\frac{\omega}{\beta_\mathrm{w}}\frac{\partial E^{(1)}}{\partial\phi} - i\omega\frac{\partial B^{(1)}}{\partial\phi} + \frac{1}{\rho}\frac{\partial}{\partial\rho}\left(\rho E^{(0)}\right) = 0 \quad (4.30)$$

$$-\frac{\omega}{\beta_\mathrm{w}}\frac{\partial B^{(1)}}{\partial\phi} + i\omega\frac{\partial E^{(1)}}{\partial\phi} + i8\pi e\left(n^{(0)}p_\perp^{(1)} + n^{(1)}p_\perp^{(0)}\right) + \frac{1}{\rho}\frac{\partial}{\partial\rho}(\rho B^{(0)}) - i\frac{M}{\rho}8\pi e n^{(0)}p_\perp^{(0)} = 0 \ , \quad (4.31)$$

and momentum/energy equations give:

$$\omega\Delta^{(0)}\frac{\partial p_\parallel^{(1)}}{\partial\phi} + \frac{e}{m}\mathrm{Im}\left(p_\perp^{(0)}B^{(1)*} + p_\perp^{(1)}B^{(0)*}\right) + p_\parallel^{(0)}\frac{\partial p_\parallel^{(0)}}{\partial\rho} - \frac{e}{m}\frac{M}{\rho}\mathrm{Im}\left(p_\perp^{(0)}B^{(0)*}\right) = \frac{|p_\perp^{(0)}|^2}{\rho} \quad (4.32)$$

$$\omega\Delta^{(0)}\frac{\partial p_\perp^{(1)}}{\partial\phi} + \omega\Delta^{(1)}\frac{\partial p_\perp^{(0)}}{\partial\phi} - \frac{e}{m}\left(\gamma^{(0)}E^{(1)} + \gamma^{(1)}E^{(0)} + ip_\parallel^{(1)}B^{(0)} + ip_\parallel^{(0)}B^{(1)}\right) + p_\parallel^{(0)}\frac{\partial p_\perp^{(0)}}{\partial\rho} + \frac{e}{m}\frac{M}{\rho}\left(\gamma^{(0)}E^{(0)} + ip_\parallel^{(0)}B^{(0)}\right) = -\frac{p_\parallel^{(0)}p_\perp^{(0)}}{\rho} - i\cot\theta\frac{p_\perp^{(0)}p_{\hat\varphi}^{(0)}}{\rho} \quad (4.33)$$

$$\omega\Delta^{(0)}\frac{\partial\gamma^{(1)}}{\partial\phi} + \Delta^{(1)}\frac{\partial\gamma^{(0)}}{\partial\phi} - \frac{e}{m}\mathrm{Re}\left(p_\perp^{(0)}E^{(1)*} + p_\perp^{(1)}E^{(0)*}\right) + p_\parallel^{(0)}\frac{\partial\gamma^{(0)}}{\partial\rho} + \frac{e}{m}\frac{M}{\rho}\mathrm{Re}\left(p_\perp^{(0)}E^{(0)*}\right) = 0 \ . \quad (4.34)$$

The slow dependence of the zeroth-order quantities on ρ follows by eliminating secular terms in the first-order quantities, i.e. by imposing the condition that they are periodic in ϕ. Equation (4.29) can immediately be integrated over ϕ, yielding, when periodicity is imposed,

$$\frac{1}{\rho^2}\frac{\partial}{\partial\rho}\left(\rho^2 n^{(0)}p_\parallel^{(0)}\right) = 0 \ . \quad (4.35)$$

Similarly, (4.30) integrates to give

$$\frac{1}{\rho}\frac{\partial}{\partial\rho}\left(\rho\int_0^{2\pi}\mathrm{d}\phi\, E^{(0)}\right) = 0 \ . \quad (4.36)$$

However, this merely constrains the average components of the wave fields, which we assume to vanish. In order to integrate (4.34) and (4.32), it is first necessary to use Ampère's law (4.31) to re-express $p_\perp^{(0)}$ in the expressions $\mathrm{Im}(p_\perp^{(0)}B^{(0)*})$ and $\mathrm{Re}(p_\perp^{(0)}E^{(0)*})$ in terms of $B^{(0)}$ and $E^{(0)}$ respectively.

We do it by substituting the Faraday's law

$$\frac{\partial B}{\partial \phi} = \frac{i}{\beta_\mathrm{w}} \frac{\partial E}{\partial \phi} - \epsilon \frac{i}{\omega} \frac{1}{\rho} \frac{\partial}{\partial \rho} \left(\rho E^{(0)} \right) \tag{4.37}$$

into the Ampère's law

$$\begin{aligned} -i8\pi n e p_\perp = {} & i\omega \left(1 - \frac{1}{\beta_\mathrm{w}^2} \right) \frac{\partial E}{\partial \phi} \\ & + \epsilon \left[i\omega \frac{M}{\rho} \left(1 - \frac{1}{\beta_\mathrm{w}^2} \right) \frac{\partial E^{(0)}}{\partial \phi} + \frac{i}{\beta_\mathrm{w}} \frac{1}{\rho} \frac{\partial}{\partial \rho} \left(\rho E^{(0)} \right) + i \frac{1}{\rho} \frac{\partial}{\partial \rho} \left(\rho \frac{E^{(0)}}{\beta_\mathrm{w}} \right) \right] \end{aligned} \tag{4.38}$$

where E and B denote the full fields, not yet expanded. This gives

$$\begin{aligned} \mathrm{Re}\left(u_\perp E^* \right) = -\frac{1}{16\pi n e} \Bigg\{ & \omega \left(1 - \frac{1}{\beta_\mathrm{w}^2} \right) \frac{\partial |E|^2}{\partial \phi} \\ & + \epsilon \left[\omega \frac{M}{\rho} \left(1 - \frac{1}{\beta_\mathrm{w}^2} \right) \frac{\partial |E^{(0)}|^2}{\partial \phi} + \frac{2}{\rho^2} \frac{\partial}{\partial \rho} \left(\rho^2 \frac{|E^{(0)}|^2}{\beta_\mathrm{w}} \right) \right] \Bigg\} \end{aligned} \tag{4.39}$$

where we used the fact that

$$\mathrm{Re}\left(\frac{\partial E^*}{\partial \rho} E \right) = \mathrm{Re}\left(\frac{\partial E}{\partial \rho} E^* \right) = \frac{1}{2} \frac{\partial}{\partial \rho} |E|^2 \tag{4.40}$$

In the first order, after multiplying by n, the equation (4.34) now takes a form

$$\begin{aligned} \omega \Delta^{(0)} n^{(0)} \frac{\partial \gamma^{(1)}}{\partial \phi} + p_\parallel^{(0)} n^{(0)} \frac{\partial \gamma^{(0)}}{\partial \rho} + \frac{\omega}{16\pi m} \left(1 - \frac{1}{\beta_\mathrm{w}^2} \right) \frac{\partial}{\partial \phi} \left({E^{(0)}}^* E^{(1)} + {E^{(1)}}^* E^{(0)} \right) \\ + \frac{1}{8\pi m} \frac{1}{\rho^2} \frac{\partial}{\partial \rho} \left(\rho^2 \frac{|E^{(0)}|^2}{\beta_\mathrm{w}} \right) = 0 \end{aligned} \tag{4.41}$$

Note that $E^{(0)}$ is periodic. The first order continuity equation implies that

$$p_\parallel^{(0)} n^{(0)} \frac{\partial \gamma_0}{\partial \rho} = \frac{1}{\rho^2} \frac{\partial}{\partial \rho} \left(\rho^2 p_\parallel^{(0)} n^{(0)} \gamma^{(0)} \right) \tag{4.42}$$

and we arrive at

$$\frac{\partial}{\partial \rho} \left[\rho^2 \left(p_\parallel^{(0)} n^{(0)} \gamma^{(0)} + \frac{1}{8\pi m} \frac{|E^{(0)}|^2}{\beta_\mathrm{w}} \right) \right] = 0 \tag{4.43}$$

In the same manner we get the expression for $\mathrm{Im}(p_\perp B^*)$. Expressing perpendicular current in terms of the magnetic field

$$\begin{aligned} -i8\pi n e p_\perp = {} & -\frac{\omega}{\beta_\mathrm{w}} \left(1 - \beta_\mathrm{w}^2 \right) \frac{\partial B}{\partial \phi} \\ & + \epsilon \left[\frac{1}{\rho} \frac{\partial}{\partial \rho} \left(\rho B^{(0)} \right) + \beta_\mathrm{w}^2 \frac{1}{\rho} \frac{\partial}{\partial \rho} \left(\rho B^{(0)} \right) - \frac{M}{\rho} \frac{\omega}{\beta_\mathrm{w}} (1 - \beta_\mathrm{w}^2) \frac{\partial B^{(0)}}{\partial \phi} \right] \end{aligned} \tag{4.44}$$

and thus

$$\begin{aligned} \mathrm{Im}(u_\perp B^*) = \frac{1}{16\pi n e} \Bigg\{ & -\frac{\omega}{\beta_\mathrm{w}} \left(1 - \beta_\mathrm{w}^2 \right) \frac{\partial |B|^2}{\partial \phi} \\ & + \epsilon \left[-\frac{M}{\rho} \frac{\omega}{\beta_\mathrm{w}} (1 - \beta_\mathrm{w}^2) \frac{\partial |B^{(0)}|^2}{\partial \phi} + \frac{1}{\rho^2} \frac{\partial}{\partial \rho} \left(\rho^2 \left(1 + \frac{1}{\beta_\mathrm{w}^2} \right) |E^{(0)}|^2 \right) \right] \Bigg\} \end{aligned} \tag{4.45}$$

From the equation (4.32), after multiplying by n and expanding, reads

$$\omega\Delta^{(0)}n^{(0)}\frac{\partial p_\parallel^{(1)}}{\partial\phi}+p_\parallel^{(0)}n^{(0)}\frac{\partial p_\parallel^{(0)}}{\partial\rho}-\frac{\omega}{16\pi m}\frac{(1-\beta_{\rm w}^2)}{\beta_{\rm w}}\frac{\partial}{\partial\phi}\left(B^{(0)*}B^{(1)}+B^{(1)*}B^{(0)}\right)$$
$$+\frac{1}{16\pi m}\frac{1}{\rho^2}\frac{\partial}{\partial\rho}\left(\rho^2\left(1+\frac{1}{\beta_{\rm w}^2}\right)|E^{(0)}|^2\right)-n^{(0)}\frac{|p_\perp^{(0)}|^2}{\rho}\frac{1}{m^2}=0 \quad (4.46)$$

The first order continuity equation implies that we can write

$$p_\parallel^{(0)}n^{(0)}\frac{\partial p_\parallel^{(0)}}{\partial\rho}=\frac{1}{\rho^2}\frac{\partial}{\partial\rho}\left(\rho^2{p_\parallel^{(0)}}^2n^{(0)}\right) \quad (4.47)$$

and now we have

$$\frac{1}{\rho^2}\frac{\partial}{\partial\rho}\left[\rho^2\left({p_\parallel^{(0)}}^2n^{(0)}+\left(1+\frac{1}{\beta_{\rm w}^2}\right)\frac{\left|E^{(0)}\right|^2}{16\pi m}\right)\right]=n^{(0)}\frac{|p_\perp^{(0)}|^2}{\rho} \quad (4.48)$$

Thus, our radial evolution equations are:

$$\frac{\partial}{\partial\rho}\left[\rho^2\left(p_\parallel^{(0)}n^{(0)}\gamma^{(0)}+\frac{\beta_{\rm w}\left|B^{(0)}\right|^2}{8\pi m}\right)\right]=0 \quad (4.49)$$

$$\frac{\partial}{\partial\rho}\left[\rho^2\left({p_\parallel^{(0)}}^2n^{(0)}+\left(1+\beta_{\rm w}^2\right)\frac{\left|B^{(0)}\right|^2}{16\pi m}\right)\right]=n^{(0)}|p_\perp^{(0)}|^2\rho\ . \quad (4.50)$$

Equations (4.35), (4.49) and (4.50) suffice to determine the dependence on ρ of the phase-averaged, zeroth-order variables. Note that, to this order, M does not appear; i.e., general relativistic effects do not enter. Furthermore, because we assume cold, dissipationless fluids that interact only via the wave fields, (4.49) simply states the conservation of the sum of the zeroth-order particle and field contributions to the phase-averaged energy flux in flat space, expressed in differential form. Radial momentum flux of the system is not conserved, because the perpendicular degrees of freedom are present, and part of the energy goes into sideways expansion of the flow. This, in fact, expresses the conservation equation for the energy-momentum tensor of the system. RHS of (4.50) appears due to nonvanishing Christoffel symbol in the 1st component of the tensor 4-divergence. This approach we discuss when investigating superluminal waves in pulsar winds, see Sect. 6.1 for details.

Integrating (4.35) and (4.49), and recovering units we get

$$2mcr^2n^{(0)}p_\parallel^{(0)}=\dot{M}/\Omega_{\rm s} \quad (4.51)$$

$$\mu=\gamma^{(0)}\left(1+\sigma\right) \quad (4.52)$$

and from (4.50)

$$\frac{d\nu}{dR}=\frac{R|p_\perp|^2}{\mu\hat{\omega}^2}\ , \quad (4.53)$$

where we define

$$\nu=p_\parallel^{(0)}\left(1+\frac{1+\beta_{\rm w}^2}{2\beta_{\rm w}^2}\sigma\right),\qquad R=\frac{\mu}{a_0}\frac{\omega r}{c}\ , \quad (4.54)$$

$\dot{M}/\Omega_{\rm s}$ is the mass-flux per unit solid-angle, $\mu=L/\dot{M}$ is the mass-loading parameter, ν is the radial momentum flux density per unit rest mass, R is the radius in units of the critical radius,

inside of which the superluminal modes do not propagate [97], and the magnetization parameter, defined as the ratio of the field and particle terms in the energy flux density, is

$$\sigma = \frac{\left|B^{(0)}/\gamma^{(0)}\right|^2}{8\pi n^{(0)} m} \ . \tag{4.55}$$

Using the definition of the strength parameter (4.3) enables the mass-flux to be expressed in terms of a_0 and μ, leading to

$$p_\parallel^{(0)} = \frac{a_0^2 c^2}{\mu r^2 \omega_{\rm p}^2} = \frac{\mu}{R^2}\frac{\omega^2}{\omega_{\rm p}^2} \ , \tag{4.56}$$

4.3.3 Radial evolution of a magnetic shear

The slow evolution of the subluminal magnetic shear wave as it propagates outwards at $r \gg r_{\rm g}$ is governed by the first-order equations in the expansion in $\epsilon \sim c/(\omega r)$, as derived in §4.3.2. Making simplifications to the notation by omitting superscripts "0", these are the continuity equation (4.56):

$$p_\parallel = \mu\hat{\omega}^2/R^2 \ , \tag{4.57}$$

the equation of energy flux conservation:

$$\mu = \gamma(1+\sigma) \tag{4.58}$$

and the radial momentum equation

$$\frac{d\nu}{dR} = \frac{R|p_\perp|^2}{\mu\hat{\omega}^2} \ , \tag{4.59}$$

where the momentum-flux density per unit mass-flux

$$\nu = p_\parallel\left(1 + \frac{1+\beta_{\rm w}^2}{2\beta_{\rm w}^2}\sigma\right) \tag{4.60}$$

and $\hat{\omega} = \omega/\omega_{\rm p}$, with the plasma frequency defined using the proper fluid density $\omega_{\rm p}^2 = 8\pi n e^2/m$. Note that in a non-monochromatic wave, the quantities $p_\parallel$, $\hat{\omega}$, σ and γ are replaced in these equations by their phase-averages.

According to (2.44), σ, as defined in (4.55), is related to the fluid momentum components through

$$\sigma = \frac{\beta_{\rm w}^4\gamma_{\rm w}^4\,|p_\perp|^2}{\hat{\omega}^2 p_\parallel^2} \ , \tag{4.61}$$

The condition that the wave velocity equals the radial component of the fluid velocity, $\Delta = 0$, implies

$$\gamma_{\rm w}^2 = \gamma^2/\left(1+|p_\perp|^2\right) \ . \tag{4.62}$$

The five equations (4.57)–(4.62), together with the definition

$$\gamma = \left(1 + p_\parallel^2 + |p_\perp|^2\right)^{1/2} \tag{4.63}$$

determine the radial dependence of the six unknown wave variables $\gamma_{\rm w}$, γ, $p_\parallel$, $|p_\perp|$, $\hat{\omega}$, and σ. It is straightforward to reduce these to a first-order ordinary differential equation for $p_\perp(\gamma_{\rm w})$, for example. Solutions extend from $R = 0$ to $R = \infty$ provided they are launched at super-magnetosonic speed: $\sigma = (\mu/\gamma) - 1 < \mu^{2/3}$. At $R \to 0$, $|p_\perp| \to 0$ and $\gamma \to \gamma_{\rm w}$, whereas at $R \to \infty$, $\sigma \to 0$ and $\gamma \to \mu$, so that the wave converts all of the Poynting flux to kinetic energy at large radius. The radial dependence of the wave goes through three phases:

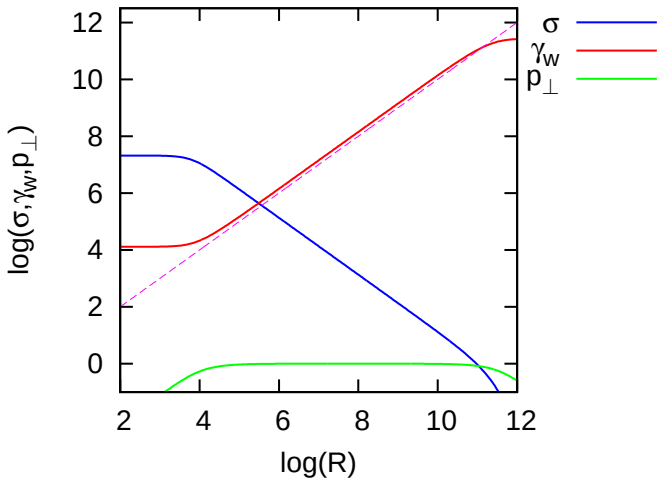

Figure 4.1: The magnetization parameter σ, transverse fluid momenta $p_\perp$ and Lorentz factor of the wave, $\gamma_{\rm w}$, as functions of the dimensionless radius $R = \mu r\omega/(a_0 c)$, for $\sigma_0 = 10^6$ and $\mu = 10^{10}$. The approximate solutions given in Eq. (4.67) are also shown.

1. At small R, $|p_\perp| \ll 1$ and the wave is essentially a cold MHD structure in which the inertia associated with the current is negligible. There is no acceleration of either the wave speed or the fluids in this regime, and the magnetization parameter σ remains constant at its initial value σ_0. Assuming $\sigma_0 \gg 1$, this region is restricted to $R \ll \mu/\sigma_0$.
2. At intermediate radii, one readily finds an approximate solution:

$$p_\perp \approx 1 \tag{4.64}$$
$$\sigma \approx \mu/(2R) \tag{4.65}$$
$$\gamma \approx 2R \tag{4.66}$$
$$\gamma_{\rm w} \approx \gamma/\sqrt{2}\ , \tag{4.67}$$

   valid in the range

$$\mu/\sigma_0 \ll R \ll \mu\ . \tag{4.68}$$

3. Finally, at large radius, $R \gg \mu$, only kinetic energy remains: $\gamma \approx \gamma_{\rm w} \approx \mu$, $|p_\perp| \ll 1$.
   This behavior is illustrated in Fig. 4.1.

4.4 Application to blazar variability

The locations of the three phases of wave propagation illustrated in Fig. 4.1 depend on the parameters a_0, μ (or $\kappa_{r_{\rm g}}$), σ_0 and ω. As discussed in Sect. 4.1, it is possible to infer values for a_0 and ω directly from the observed flux and variability timescale. Another parameter may be eliminated by fixing the wave speed at its launching point. A very slow, sub-magnetosonic outflow can be described by the force-free MHD equations, and would accelerate as $\gamma \propto r$ [36], until it approached the sonic speed, where $\gamma_0 \approx \sigma_0^{1/2} \approx \mu^{1/3}$. On the other hand, all waves launched at super-magnetosonic speeds ($\sigma_0 < \mu^{2/3}$) behave similarly, as described in §4.3.3, with the acceleration phase moving out to larger radius as the initial magnetization decreases. It suffices, therefore, to analyze the case of mildly supersonic launch: $\sigma_0 \approx \mu^{2/3}$, corresponding to the maximum magnetization of a supersonic flow.

However, the uncertainty associated with the unknown mass-loading of the flow can be removed only by modelling the pair cascade. Leaving this quantity as a free parameter, the

radius $r_{\rm acc}$ at which acceleration begins, corresponding to $R \approx \mu/\sigma_0$, is

$$\begin{aligned} r_{\rm acc} &\approx r_{\rm g} a_0^{1/3} \kappa_{r_{\rm g}}^{2/3} \left(\omega r_{\rm g}/c\right)^{-1/3} \\ &= 1.2\, \Delta t_{100}^{1/3} \kappa_{r_{\rm g}}^{2/3} L_{46}^{1/6} M_9^{2/3}\, {\rm pc} \ , \end{aligned} \tag{4.69}$$

where we define the variation timescale in units of 100 s to be $\Delta_{100} = (2\pi/\omega)\,/\,(100\,{\rm s})$, and write the mass of the black hole as $M = M_9 \times 10^9\,{\rm M}_\odot$. For $r < r_{\rm acc}$ the Lorentz factor of the flow remains constant at roughly the sonic speed:

$$\gamma_0 \approx 6.5 \times 10^3 \Delta t_{100}^{1/3} \kappa_{r_{\rm g}}^{-1/3} L_{46}^{1/6} M_9^{-1/3} \tag{4.70}$$

and, for $r > r_{\rm acc}$, the Lorentz factors increase linearly with r:

$$\gamma_{\rm w} \approx \gamma/\sqrt{2} \ \approx \ 7.4 \times 10^3 \left(r/1\,{\rm pc}\right) \kappa_{r_{\rm g}}^{-1} M_9^{-1} \ . \tag{4.71}$$

The solutions presented in §4.3.3 eventually convert all of the Poynting flux to kinetic energy flux at large radius. However, in the case of blazars, this is unlikely to be realized, since the resulting Lorentz factor ($= \mu$) is very large. Instead, dissipative processes so far neglected, such as instabilities in the wave-solution, or interaction of the jet with the external medium, or with ambient photons, are likely to intervene.

The wave propagates radially with fixed frequency. However, if it converts part of its energy into high-frequency ($\gg \omega$), forwardly beamed photons via an emissivity that is modulated by the wave-phase, then the difference between photon and wave propagation speeds will lead to a smoothing of the modulation in the observed photon signal. This loss of short-timescale variability becomes more effective as the size of the radiating section of the wave increases. Similarly, if the photons do not propagate exactly in the radial direction, smoothing of the modulation will be produced by the difference in light-travel time to the observer from different parts of the spherical wavefront. In §3.5.4 we discussed the criterion (3.102) on the size of the emitting region (assumed here $\sim r = l'/\gamma_{\rm w}$, where l' is the size of the emitting region in the comoving frame) and the Lorentz factor of the jet $\gamma_{\rm w}$, such that fluctuations of frequency $\omega = 2\pi/t_{\rm obs}$ are not suppressed in the photon signal – here this criterion takes a form

$$\gamma_{\rm w}^2 2\pi c/\omega > r \ . \tag{4.72}$$

In the acceleration region, $\gamma_{\rm w} \propto r$, so that this condition is fulfilled everywhere within this region, provided it is satisfied at the beginning, where $r = r_{\rm acc}$, and $\gamma_{\rm w} = \gamma_0$. Combining (4.69) and (4.70) the requirement that modulation on a timescale of $100\Delta t_{100}$ seconds should not be filtered out leads to an upper limit on the multiplicity:

$$\kappa_{r_{\rm g}} < 14\, \Delta t_{100} L_{46}^{1/8} M_9^{-1} \ . \tag{4.73}$$

Equation (4.73) implies that electron-positron pair creation is much less effective in the central engine of a rapidly variable blazar than it is in a pulsar magnetosphere [145], but this is perhaps not unexpected, given that a neutron star surface is able to anchor a very strong magnetic field. However, it also implies that blazars exhibiting extreme variability contain a charge-starved magnetosphere able to support a vacuum gap [122, 125]. This scenario is particularly attractive, because the non-stationary nature of gap discharges found in pulsar-related studies [187, 182, 126, 198], suggests a natural source of short-timescale ($< r_{\rm g}/c$) variability in the outflow from a black-hole magnetosphere.

4.5 Summary and conclusions

Here we described a mechanism that causes a magnetically dominated, radial outflow from a black-hole magnetosphere to enter a delayed acceleration phase, starting at a distance from the hole given by (4.69). Applying this mechanism to blazar jets, we derive a constraint, (4.73), on the pair density in the magnetosphere that permits radiation produced in the jet acceleration region to retain short-timescale structure imposed on it close to the launching site.

The mechanism is based on an analysis of the propagation characteristics of a nonlinear wave – specifically a circularly polarized magnetic shear – in a low-density plasma. Such a wave, we suggest, is likely to be launched in the polar regions of a rotating, accreting black hole, and, in a non-axisymmetric picture, may fluctuate on a time shorter than $r_{\rm g}/c$, as indicated by observations of the source PKS 2155-304. Acceleration is a result of charge-starvation – a non-MHD effect that arises when the relative drift-speed of the oppositely charged constituents in a low-density plasma becomes relativistic. The analysis employs a cold two-fluid model of the plasma, and uses a short-wavelength perturbation expansion to find the evolution of the radially propagating, nonlinear wave. The equations are derived in Kerr geometry. However, under the conditions we envisage, where the wavelength of the oscillation is of the same order in the expansion parameter as the gravitational radius, general relativistic effects do not appear in the governing equations.

Several important problems remain to be investigated. These include the nature of the dissipation and radiation mechanisms, and the effect these might have on the propagation of the wave, as well as the possibility of modelling the multi-wavelength blazar spectrum. Furthermore, although the picture of a circularly polarized magnetic shear that is static in the jet frame is intuitively attractive, this is only one specific, nonlinear solution of the governing equations; other polarizations and other modes, such as the linearly polarized striped wind [133] or the electromagnetic mode of superluminal phase-speed [97, 10] may also prove important. Nevertheless, the underlying physical cause of the acceleration — the inertia of the charge-carriers — suggests that delayed jet-acceleration may be a generic phenomenon.

Part III

Chapter 5

Pulsar winds

In this chapter we summarize the present state of our knowledge and models of Poynting-flux dominated outflows from pulsars. Our current understanding is based mainly on theoretical modelling and numerical simulations. Many key issues, such as the details of the pair production sites in the pulsar magnetosphere, the corresponding multiplicity of pair cascades, and the location of emitting regions, are still open. First, in Sect. 5.1 we discuss the launching of pulsar winds, together with the suggested models of vacuum gaps in otherwise force-free magnetospheres, where the particles are accelerated and pair avalanches ignited. Sect. 5.2 summarizes the physics of the outflowing, MHD wind: its structure §5.2.1, the parameters that are thought to describe it (albeit rather poorly constrained) §5.2.2, and the formation of the MHD termination shock at the interface with the surrounding nebula §5.2.3. However, this MHD description of the shock suffers from the so-called magnetization problem, which we describe in §5.2.4. In Sect. 5.3 we discuss a possible solution to this problem – the model of electromagnetic precursors to the termination shocks. We summarize the conditions for such a precursor to propagate in §5.3.1, and the conversion process between the MHD striped wind and the precursor – in §5.3.2.

5.1 Launching from the magnetosphere

A magnetosphere is the region closest to a neutron star – located inside the light cylinder, where the electromagnetic fields dominate the plasma dynamics, and where a pulsar wind is thought to originate from. A full understanding of pulsar wind launching requires the knowledge of (1) a field topology, (2) the location of particle accelerating regions, and (3) the mechanisms that lead to the charge supply in the flow. The latter are closely linked to radiation processes, which in a strong-field regime often change their character or become dominated by new, exotic phenomena, resulting from energy quantization in the direction perpendicular to the field, nonconservation of transverse momenta, and the importance of the particle spin [78].

The structure of the magnetic field is anticipated from the polarimetry of averaged pulse profiles. The sweep of the polarization angle through the radio pulse profiles is consistent with the dipole geometry [172]. Close to the surface, however, higher multipoles are expected to be important [20, 69]. The strength of the magnetic field can be measured directly from the energies of cyclotron absorption lines in the X-ray spectra of X-ray and γ-ray pulsars. The lines are generated in resonant photon scattering and absorption by electrons at multiples of the cyclotron frequency[1] (e.g., [78])

$$\omega_B = \frac{eB}{mc} = 2 \times 10^{19} B_{12} \text{ Hz } \rightarrow \text{ } 12 B_{12} \text{ keV} \tag{5.1}$$

[1]The occurrence of the resonant lines is a result of the aforementioned quantization of the momentum component perpendicular to the magnetic field. The quantized energy levels are discrete Landau states, separated by the cyclotron energy.

These measurements imply the fields exceeding 10^{12} G.

A neutron star rotating in this dipole field, generates also a quadrupole electric field, in a direct analogy to a unipolar inductor: as for a conductor rotating in a magnetic field, charges on the pulsar's surface are redistributed by the Lorentz force, what induces an electric potential difference between the poles and the equator. The normal component of the resulting electric field $E_\parallel = \omega B r_*/c$ acts on the charges with the force that is orders of magnitude larger than the gravitational one

$$\frac{eE_\parallel}{GMm/r_*^2} \approx 8 \times 10^{11} B_{12} P_1^{-1} \tag{5.2}$$

where $B = B_{12} \times 10^{12}$ G, $P = P_1$ s is a pulsar rotation period, and $r_* = 10$ km is a typical radius of a neutron star. Hence, the dynamics in a magnetosphere is completely dominated by the electromagnetic fields. The binding energy of material on the stellar surface is thought to be smaller than the work done by the electric forces and, therefore, the field is able to rip the charges off the surface, providing particles to the magnetosphere. These particles are accelerated and redistributed to screen out the accelerating field component. For an aligned rotator, the minimum charge density needed for this screening was obtained in the ideal MHD approximation $\boldsymbol{E}+\boldsymbol{v}\times\boldsymbol{B}/c = 0$ (where $\boldsymbol{v} = \boldsymbol{\omega}\times\boldsymbol{r}$), with the magnetic field lines as equipotentials (i.e. $\boldsymbol{E}\cdot\boldsymbol{B} = 0$), by Goldreich & Julian (GJ) [71]

$$\rho_{\rm GJ} = \frac{1}{4\pi}\nabla\cdot\boldsymbol{E} = -\frac{\boldsymbol{\omega}\cdot\boldsymbol{B}}{2\pi c}\frac{1}{1-(\omega r/c)^2\sin^2\theta} \tag{5.3}$$

This model describes a stationary state of an aligned rotator, with a corotating, closed magnetosphere, and a wind of charges flowing along the open magnetic field lines from the polar cap regions.

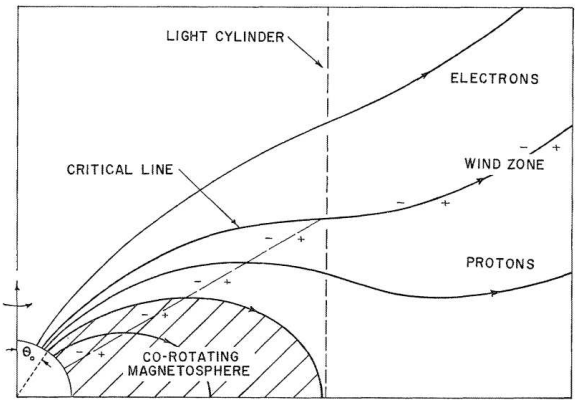

Figure 5.1: Goldreich-Julian space charge. The null surface is shown by the inclined line that separates charges of opposite sign. Taken from [71].

The charge is not lost from the system as long as the return current back to the star is assumed. In fact, the derivation of GJ density assumes that the charges fill in the entire space that surrounds the pulsar. However, it was pointed out by Holloway [85] that many field lines must cross the null surface $\boldsymbol{B}\cdot\boldsymbol{\omega} = 0$, beyond which the required charge density has the opposite sign to the charges that can be supplied from the star. Thus, large vacuum gaps can be expected to develop and the current closure is not possible. This in turn implies charging up of the star itself, until the growing electric field finds its balance with the pulsar surroundings. The question was posed, if there exists a stable self-consistent solution with such the vacuum gaps, satisfying $\boldsymbol{E}\cdot\boldsymbol{B} = 0$ everywhere.

A self-consistent solution describing the system with a net charge (fixed by the rotation rate) was given by Krause-Polstorff & Michel [112, 111]. In their model, the electrodynamics of an aligned, charged rotator is characterized by the formation of an "electrosphere", i.e., a charge distribution with polar domes filled with one-sign charges, the equatorial torus with the opposite-sign charges, and a huge vacuum gap in between. The electrosphere has a finite extend, well within the light cylinder, hence no plasma can flow (the domes corotate, and the torus rotates differentially). Numerical simulations show that the GJ configuration indeed collapses to the stable electrosphere [195].

However, the aligned rotator in this equilibrium state is inactive. For that reason most of theoretical and numerical attention was paid to wind models, in which the pulsar magnetosphere is filled with a plasma being produced in a self-consistent way. This implies that a real pulsar magnetosphere cannot be force-free everywhere. Crucial for maintaining pulsar activity are limited regions ("gaps"), where the electric field is not screened out, and pair production takes place, being a consequence of particle acceleration, radiation and materialization of photons into leptons. Hence, in plasma-filled models a force-free, global picture of a magnetosphere is closely linked to the dynamics of small charge-starved gaps, which are able to replenish a constantly outflowing plasma.

Avalanche pair production starts when the rotationally-induced electric field rips the primary charges off the stellar surface. They can move only along the magnetic lines, because any perpendicular momentum they had, would be immediately radiated in the synchrotron process (see e.g., [14, 79]). Since a relativistically moving charge emits the synchrotron power $P \approx 2r_0^2 c\gamma^2 B^2/3$, a timescale for radiating away its perpendicular momentum can be estimated as

$$t \sim \frac{\gamma mc^2}{P} = \frac{3m^3c^5}{2e^4\gamma B^2} \approx \frac{5\times 10^{-16}}{\gamma B_{12}^2} \text{ s.} \tag{5.4}$$

where $B = B_{12}\times 10^{12}$ G. Note that the synchrotron radiation in pulsar conditions is characterized by discrete transitions from higher to lower Landau states. This occurs in a very short timescale, hence nearly all the particles must occupy the Landau ground state. However, in a motion along the curved, dipole magnetic field lines, particles undergo acceleration. This inevitably will lead to the curvature emission. If the emitted photons are energetic enough, they can decay into e^-e^+ pairs, initiating electromagnetic cascades. The development of avalanche pair production in a pulsar magnetosphere involves several steps:

(1) acceleration of primary particles by an unscreened electric field – the regions of particle acceleration must contain an electric field component parallel to the magnetic field $\boldsymbol{E}\cdot\boldsymbol{B} \neq 0$. According to the current models, this is possible only in limited "gaps" of an otherwise force-free magnetosphere.

(2) emission of high-energy photons – the dominant radiation mechanisms are the curvature emission (electrons with Lorentz factors $\geq 10^6$), resonant and nonresonant inverse Compton scattering of thermal X-rays from the star by primary electrons, and the synchrotron radiation of secondary pairs. Similarly as for resonant absorption (in which a particle excited to a higher Landau level deexcitates collisionally), in a strong-field regime also the cross section for Compton scattering (in which an incident photon excites an electron to a higher Landau level, from which it then decays spontaneously) has a resonance at the cyclotron (and higher harmonics) energy. In the strongest fields, the cross section for this process increases by few orders of magnitude in comparison to the Thomson cross section (e.g., [50]), what decides about its great efficiency in typical pulsar conditions (i.e. typical surface fields and temperatures). Electrons with Lorentz factors $\gamma \sim 10^2 - 10^6$ can upscatter resonantly thermal photons from the star surface up to energies $\epsilon \approx \gamma Bmc^2/B_{\rm cr}$. [2] When $\gamma \sim 10^6$, the scattered photon can ignite a cascade in a field $B \approx 10^{12}$ G [40]. In case of millisecond pulsars with lower fields, the dominant process is the non-resonant scattering. In this case, for $\gamma \geq 10^5$ the X-ray photons will be upscattered to energies $\epsilon \sim \gamma$ in the Klein-Nishina regime.

(3) photon decay into secondary $e^\pm$ pairs – in the presence of a magnetic field a transverse momentum may not be conserved, because the field can supply or absorb a momentum (however, the total energy and parallel momentum are strictly conserved). Hence, possible becomes one-photon splitting, in which a photon with energy ϵ_γ, moving at a sufficiently large angle $\theta_{\gamma B}$ to

[2] Landau states have energy levels given by $E_n = (1 + p^2 + 2nB/B_{cr})^{1/2}$. In the nonrelativistic regime $p \ll 1$, $B \ll B_{cr}$ and hence the gap between two neighboring levels $\Delta E \approx B/B_{cr}$. Thus, the resonant photon has the energy $\sim B/B_{cr}$ in the electron frame; after the scattering its energy in the lab frame is $\sim \gamma B/B_{cr}$.

the magnetic lines, given by the threshold for the pair production

$$\epsilon_\gamma \sin\theta_{\gamma \mathrm{B}} \approx 2mc^2, \tag{5.5}$$

converts into an e^-e^+ pair. This photon, radiated by a particle accelerated along the field lines, moves initially at a very small angle to the field lines but as their curvature increases with the distance, the angle also increases till the threshold for the pair production is satisfied. Simulations, e.g. [81], show that at this point the pair growth is very rapid, and the thin layer, called the pair formation front (PFF), limits the gap height. Beyond, the voltage of the gap is suppressed, so that an outflowing plasma can be regarded as quasi-neutral. Energetic γ-rays can also undergo two-photon scattering: for GeV photons collisions with X-rays – and for the highest TeV photons collisions with the soft optical and IR photons – play a role. These X-ray and soft photons may come from the synchrotron radiation of pairs. When $B > B_{\mathrm{cr}}$ splitting of an energetic photon into two lower-energy photons dominates over pair production [80].

(4) the synchrotron radiation of secondary pairs,

(5) further pair production by photons and emitting electrons.

However, it is still not clear where these processes really take place in pulsar magnetospheres. First models were focused on the regions (both the vacuum and space-charge limited flow gaps) close to the magnetic poles, from where a plasma escapes along the open field lines, forming a pulsar wind. The existence of the polar gap would naturally account for replenishing of ouflowing charges. Any depletion would result in the rapid growth of an unscreened electric field, until it again reaches the value for a gap breakdown [187, 179]. In this polar-gap picture, the particle acceleration and radiation occurs close to the stellar surface, but other locations of magnetospheric gaps were also proposed, mostly in order to explain the high-energy pulsed emission from pulsars. In fact, the high-energy radiation can be of non-magnetospheric origin, well described in the framework of the pulsar wind models [165] – for review see also [100], and references therein. This possibility we discuss in the next sections, here focusing on the vacuum gap models that involve (see Fig. 5.2):

(1) the slot gap – according to Arons [13], a narrow slot gap is placed in the polar region, but its height varies across the polar cap. The parallel component of a generated electric field well inside the polar cap is large, and the pair formation front is close to the surface. Further from the magnetic axis, on the last closed field line in a magnetosphere, Arons assumed the perfect conducting boundary conditions, so that on this line $E_\parallel$ vanishes. Thus, close to this boundary, large distances are needed to accelerate particles to high energies. The particles accelerated along the gap can gain high Lorentz factors, limited by the curvature radiation losses to $\gamma \sim 10^7$.

(2) the outer gap – in a model suggested by Cheng, Ho & Ruderman [41] both acceleration and particle radiation occurs close to, but still within, the light cylinder. Similarly as in the aligned rotator case of Goldreich & Julian, they argued that the vacuum gaps will be formed beyond the null surface defined by $\boldsymbol{B}\cdot\boldsymbol{\omega} = 0$, along the lines that cross it. Beyond this surface the charge density required to screen the electric field, has the opposite sign to the charges that can be supplied from the star. Cheng et al. considered the pair production model that would limit the growth of the gap, such that the empty outer magnetosphere of Holloway is not achieved, and a vacuum is limited to a narrow region only. Here, plasma generation processes may have a different nature than those relevant in the polar gap, since in the outer magnetosphere the magnetic field is weaker than that close to the stellar surface.

(3) the two-pole caustic model – in the model of Dyks & Rudak [57] the gap, confined to the surface of the last open field line, also extends up to the light cylinder, however starting not from the null surface as in the outer gap model, but from the neutron star itself. To model the high-energy emission in the polar gap models alone, one has to assume small inclination and the right viewing angle to reproduce the observed lightcurves [51]. The models of the gaps that extend to the outer magnetosphere overcome these difficulties. In particular, in the two-pole caustic model, high-energy photons are produced tangentially to the magnetic field lines, uniformly along the

whole gap length. To the distant observer, photons from different altitudes accumulate and the emission pattern is caustic. The accumulation occurs due to caustic effects: phase delay (due to pulsar rotation) of the photons from high altitudes is compensated by the time of flight and aberration of the photons from lower altitudes.

(4) the light cylinder gap – all of the previous models predict a cut-off of emission around GeV. However, in the case of the Crab pulsar (and so far only there) sub-TeV tails in the pulsed high-energy emission were recently detected [9, 7]. It is not clear whether this is a separate spectral component or it links somehow to the GeV emission. Bednarek [22] proposed the model, in which an accelerating gap forms very close to the light cylinder, where the open magnetic field lines bend due to the retardation effect. At this point the electric potential is not shorted out by the GJ charge configuration (the possibility of charge depletion close to the light cylinder was also noted by Holloway [85]), particles get accelerated and radiate the curvature photons in sub-TeV range. The leading (the last open field line in the direction of rotation) and the trailing (the last open field line in the opposite direction) magnetic field lines exhibit different curvature, hence the two peaks of the very high energy lightcurve can have different spectra and structure. In this model, the particles streaming along the intermediate lines would be responsible for the interpulse emission.

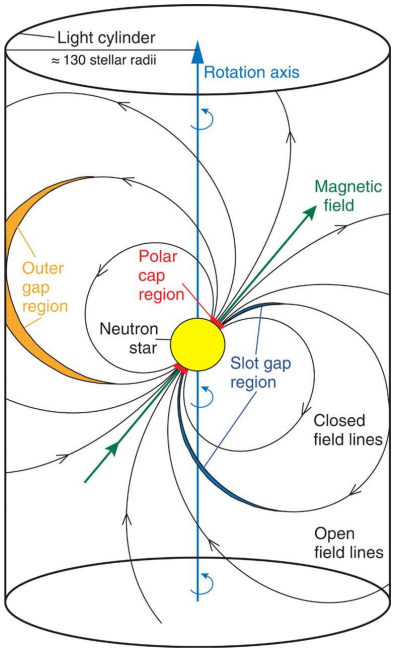

Figure 5.2: Sketch of a pulsar magnetosphere and the location of accelerating gaps. Taken from [8].

According to numerical simulations of the cascade generation [80], only the youngest pulsars, with the largest potential across their vacuum gaps, are able to create pairs by curvature photons [81]. The peak energy of such a photon,

$$\epsilon = \frac{3\lambda_{\rm c}}{2\rho_{\rm c}}\gamma^3 \approx \frac{2\times 10^{-18}}{\hat{\rho}_{\rm c}}\gamma^3 \tag{5.6}$$

where $\lambda_{\rm c} = h/mc$ is the electron Compton wavelength, $\rho_{\rm c} = \hat{\rho}_{\rm c} c/\omega$ is the curvature of a field line (for the last closed one $\rho_{\rm c} \sim c/\omega$ and for Crab $\omega = 190.4$ s^{-1}), is much lower than the IC peak energy in the Klein-Nishina regime, given by $\epsilon \sim \gamma$. Therefore, production of the curvature photon that is able to initiate a cascade, requires large particle Lorentz factors [80]. On the other hand, nearly all radio pulsars are able to produce pairs in nonresonant IC scattering [81].

According to all pulsar models, pair production rate in electromagnetic cascades is supposed to be large, orders of magnitude larger than that required to screen out a vacuum parallel electric field. For the Crab pulsar the latter implies the pair injection rate given by $\dot{N}_{\rm GJ} \sim 10^{34}$ s^{-1}. One can define the multiplicity parameter $\kappa = N/N_{\rm GJ} = \dot{N}/\dot{N}_{\rm GJ}$, which is a number of pairs created per one primary particle. Observational constraints on κ can be provided by nebular synchrotron emission, when one assumes that all the radiating particles are supplied by the pulsar wind. In the following sections we discuss the value of κ that is implied by both direct measurements, and theoretical magnetospheric models.

Let us make a brief remark. In fact, all the magnetospheric models assume that in the closed-field zone a plasma is corotating. However, as pointed out by Yuen & Melrose [147], screening of the parallel component of the electric field in the magnetosphere, does not have to be accompanied by screening of its perpendicular component, as usually assumed. They showed that complete screening is not possible at all, and the magnetosphere is never strictly corotating. This could give an explanation to phenomena like subpulse drifting, observed in the lightcurves of some pulsars.

5.2 The striped wind

5.2.1 Structure

Since close to the neutron star the electromagnetic fields dominates the energetics, particle inertia are usually neglected in the analysis. Plasma is assumed to be cold, in the sense that any transverse motion would be suppressed in the superstrong magnetic field due to synchrotron radiation. In a good approximation, therefore, if only pair production in a magnetosphere is prolific, a force-free electrodynamics (FFE) is applicable. This formulation is a low-inertia limit of MHD, useful for self-consistent modelling of a plasma in strong electromagnetic fields. Plasma particles are assumed to be massless, but they carry charge and currents [75]. Such a limit significantly simplifies the MHD equations, which include inertial terms.

An exact solution for a force-free magnetosphere of an aligned rotator was given by Michel [149]. He noted that the freezing-in MHD condition, together with the force balance in the limit of vanishing particle inertia, imply that a self-consistent current flows in the magnetosphere. The equation governing its generation allowed him to find an equation for the magnetic field lines. In the corotating zone he found a monopole solution, and all the higher, axisymmetric multipole moments he derived by differentiation with respect to z, a coordinate along the symmetry axis. First derivative leads to a dipole field, which describes both the closed, corotating magnetic field lines, entirely contained within the light cylinder, and the open ones, which originate from the polar caps and cross the light cylinder at the right angle. The transition between these two topologies occurs at the critical line that reveals a cusp in the equatorial plane, when it reaches the light cylinder.

Beyond the light cylinder, this magnetospheric solution can be matched to a solution for an MHD wind of an aligned rotator [150, 180]. However, the exact configuration of a magnetic field at the transition region near the light cylinder is not completely understood. Outside the light cylinder rigid corotation of a plasma is not possible, and both the drift velocity across the field lines, and also the velocity component along the field lines, are present. In the limit of negligible particle inertia, a monopole configuration has exactly radial lines in the meridional plane, and in the equatorial plane these lines develop a perfect Archimedean spiral

$$r_{\rm s} = r_{\rm L}\phi \tag{5.7}$$

regardless of a field topology inside the light cylinder. Globally, more appropriate is a split-monopole configuration, in which two half magnetic monopoles of opposite polarity are separated in the equatorial plane. This change in magnetic field direction must be, according to MHD,

accompanied by formation of a current sheet, within which the magnetic field vanishes and the pressure, necessary to keep the equilibrium, is supported by a hot plasma.

This solution was generalized for an oblique rotator by Bogovalov [33]. He was able to reduce the oblique-rotator problem to the axisymmetric one, and used Michel's solution of an aligned rotator. In the oblique case, a current sheet oscillates around the equatorial plane as the pulsar rotates, connecting the equator with field lines of opposite polarity every half a period. The corrugated current sheet is given by the equation $\boldsymbol{e} \cdot \boldsymbol{e}_{\mathrm{M}} = 0$, where the unit vector $\boldsymbol{e} = (\sin\theta\cos\phi, \sin\theta\sin\phi, \cos\theta)$ points in the direction of a sheet surface point, and $\boldsymbol{e}_{\mathrm{M}} = (0, \sin\chi, \cos\chi)$ – in the direction of the stellar magnetic moment, inclined with the an angle χ to the rotational axis. Taking into account (5.7), $r_{\mathrm{s}} = (V/\omega)\phi = \beta r_{\mathrm{L}}\phi$, where $V = \beta c$ is the wind velocity, one gets the equation (see also, e.g., [164])

$$r_{\mathrm{s}} = \beta r_{\mathrm{L}} \left[\pm \arccos\left(-\cot\chi\cot\theta\right) + 2n\pi\right] \tag{5.8}$$

where n is an integer. In the equatorial plane, like in the case of an aligned rotator, a current sheet forms a perfect Archimedean spiral. It is shown in the Fig. 5.3 for an inclination angle $\chi = \pi/6$.

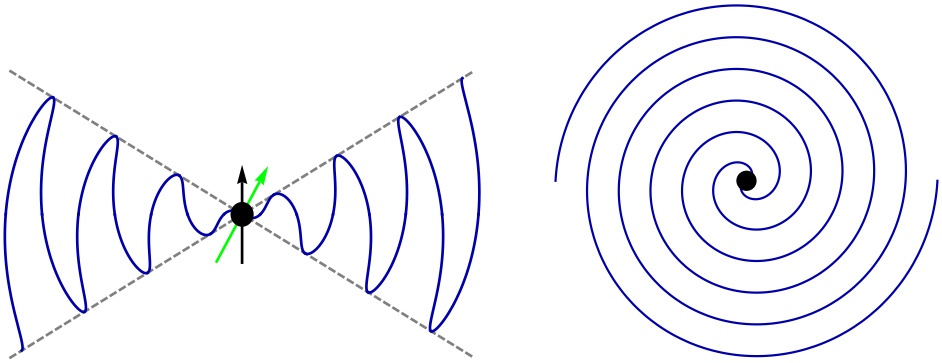

(a) meridional plane (b) equatorial plane

Figure 5.3: A current sheet plotted for an inclination angle $\chi = \pi/6$. In the equatorial plane the sheet forms a perfect Archimedean spiral.

Coroniti [48] and Michel [151] argued that in the physical scenario, in which a current sheet is not only a mathematical discontinuity, but the plasma dynamics becomes important, the wave developed by the oscillating current sheet is not monochromatic. They argued that the toroidal magnetic field and the poloidal current generate $\boldsymbol{j} \times \boldsymbol{B}$ force, that acts on the particles and makes the current sheet thinner and thinner. This interaction would cause the wave to evolve into a square shape, consisting of stripes of a cold, magnetized plasma, separated by the current sheets of a hot, unmagnetized plasma. The magnetic field in each stripe is constant and changes polarity from one stripe to another. In the equatorial plane the stripes have the equal width, hence the average magnetic field vanishes. This is not the case for the higher latitudes, for which a phase-averaged magnetic field is nonzero.

At large distances the azimuthal component of the magnetic field is dominant over the poloidal one. Their radial dependence can be obtained from the magnetic flux conservation $\nabla \cdot \boldsymbol{B} = 0$. Integrating over the volume of a sphere of a radius r, one gets from the Gauss theorem

$$B_r \propto \frac{1}{r^2} \tag{5.9}$$

Similarly, as the number of field lines in the sectional area is constant,

$$B_\phi \propto \frac{1}{r} \tag{5.10}$$

The poloidal component, which in this solution is purely radial, decreases much faster than the toroidal one. Observations of synchrotron radiation at the edge of the dark cavity, show uniform linear polarization in the optical and radio bands, which is consistent with the toroidal magnetic field structure, predicted in the wind.

However, as pointed out by Usov [200] and Michel [151], according to the mass continuity $r^2 N v_r = \text{const}$, the density of current carriers N, as measured in the laboratory frame, drops as

$$N \propto \frac{1}{r^2} \tag{5.11}$$

hence, faster than the magnetic field they are required to maintain. In the plasma frame, integrating Ampère's law over the toroidal ring of thickness Δ' (which is the thickness of a current sheet), one obtains

$$2B'_\phi = \frac{4\pi}{c} j'_\theta \Delta' \tag{5.12}$$

where $j'_\theta = eN'v_\theta$. In the lab frame $B_\phi = \gamma_\mathrm{w} B'_\phi$, $N = \gamma_\mathrm{w} N'$, $\Delta = \Delta'/\gamma_\mathrm{w}$, hence

$$B_\phi \propto \gamma_\mathrm{w} N v_\theta \Delta \tag{5.13}$$

The left hand side decreases as $1/r$, but the right hand side would fall as $1/r^2$ if γ_w and Δ were constant (v_θ is limited by c). Speed of an ideal MHD radial wind does not change indeed, because the outward pressure gradient of the magnetic field lines is exactly balanced by the inward tension force [133]. As discussed by Coroniti [48], Michel [151], and also Lyubarsky & Kirk [133], if the wind speed does not change, the particles are forced to stream with higher and higher drift-speed, but, since it cannot reach c, the anomalous resistivity arises, which in turn may lead to magnetic reconnection. As a result, magnetic energy would be released into heating of a plasma. Lyubarsky & Kirk pointed out that this heated plasma will perform work on the flow, leading to its acceleration. The reason is that a hot plasma exerts an outward pressure gradient, but there is no inward tension force. In particular, their asymptotic solution is $\gamma_\mathrm{w} \propto r^{1/2}$ and $\Delta \propto r^{1/2}$. The radius at which reconnection can start r_rec, depends on the initial particle density in the sheet [133]. They argued that, if it is small compared to the density in the cold magnetized stripes, the sheet can maintain the required current at $r > r_\mathrm{rec}$ by absorbing particles from the cold phase during expansion. In this case, MHD description retains its validity, but there also exist regions of magnetic field annihilation. This reduces the magnetic field in a wind frame, and also the required current, so that the MHD solution can indeed exist at much larger distances. They showed that for an MHD picture to be valid all the way to the termination shock, a minimum multiplicity is required, however (for the Crab $\kappa > 10^4$, which is not very demanding). In general, no significant dissipation occurs before the MHD wind arrives at the shock, which must be then itself responsible for the wave dissipation.

Apart from acceleration due to reconnection, another possibility arises. The flow may indeed become charge-starved, and therefore non-stationary, so that the displacement current in Ampère's law cannot be neglected any more. Usov [200] and Melrose & Melatos [146] suggested that when the MHD description loses validity, the wind may convert to another, electromagnetic wave whose propagation would be described by a non-MHD approach. In the striped wind scenario the distance r_max, beyond which the available charge carriers are unable to carry the necessary current, Lyubarsky & Kirk [133] calculate as

$$r_\mathrm{max} = \frac{\pi}{2} a_\mathrm{L} \frac{c}{\omega} \tag{5.14}$$

which for the Crab nebula is $r_\mathrm{max} = 1.9 \times 10^{19}$ cm (for definition of a_L see Eq. 5.17 below), much larger than the distance to the termination shock. Thus, the MHD description is formally valid up to this radius. Despite that the possibility of a mode conversion will be still open, if strong

electromagnetic waves can propagate at distances smaller than the shock radius. For this, the shock has to be sufficiently far – a condition, satisfied for the wind shocks from isolated pulsars. In fact, this scenario might provide a solution to the problems that the ideal MHD description cannot account for, and which we discuss in the next sections.

5.2.2 Parameters

A rotating magnetic dipole, the simplest model of a pulsar, losses its rotational energy due to magnetic dipole radiation; if the rotator is immersed in a plasma, it always losses energy, but if it is surrounded by a vacuum, the rotational and magnetic axes have to be misaligned [158, 76]. This radiation is emitted at the light cylinder distance $r_{\rm L} = c/\omega$, beyond which the corotation velocity exceeds the speed of light, and the information about a time-dependent changing field arrives with retardation. It is convenient to express the pulsar spin-down luminosity L in terms of the energy (Poynting) flux $\langle F \rangle$ of the emitted wave, which carries the entire pulsar energy flux

$$\frac{L}{4\pi r^2} = \langle F \rangle = \frac{cB^2}{4\pi} \tag{5.15}$$

Here we also assumed that the pulsar luminosity is isotropic. One can define the strength parameter of this radiated wave as [97, 10]

$$a \equiv \frac{eB}{mc\omega} = a_{\rm L}\frac{c}{\omega r} \tag{5.16}$$

where the dimensionless luminosity

$$a_{\rm L} = \left(\frac{e^2 L}{m^2 c^5}\right)^{1/2} \tag{5.17}$$

The latter is in fact an observable. Modelling a pulsar as a spherical neutron star, one can estimate its rotational energy $E_{\rm rot} = \frac{1}{2} I\omega^2$, where the moment of inertia $I = \frac{2}{5} M_* r_*^2 \approx 10^{45}$ g cm^2, given that $M_* \approx 1.4{\rm M}_\odot$, $r_* \approx 10$ km. If the rotator slows down, the emitted spin-down power is $L = \dot{E}_{\rm rot} = I\omega\dot{\omega}$, where the pulsar's rotational frequency ω can be measured directly from lightcurves, and its derivative $\dot{\omega}$ – from phase timing. For Crab $\dot{\omega}/\omega \approx 1/2400$ yr^{-1} (see, e.g., [70] and references therein) implies $L = 4.8 \times 10^{38}$ erg s^{-1} and hence

$$a_{\rm L} = 3.4 \times 10^{10} L_{38}^{1/2} \tag{5.18}$$

The magnetic field at the light cylinder, as given by (5.16), is

$$B_{\rm L} = 3.7 \times 10^5 \,{\rm G} \tag{5.19}$$

This calculation is accurate if the pulsar spin-down were purely due to the dipole emission in a vacuum. In reality, other processes may contribute. This problem has been investigated in observations and simulations. The most accurate observational verification is based on coherent phase timing (for discussion see [129]). One measures pulse times of arrival and fits them into the Taylor expansion of the pulse phase $\phi(t) = \phi(t_0) + \omega_0(t-t_0) + \frac{1}{2}\dot{\omega}_0(t-t_0)^2 + \frac{1}{6}\ddot{\omega}_0(t-t_0)^2 + ...$ The first and the second derivative of the rotational frequency determine the braking index n of a pulsar, defined as

$$\dot{\omega} \propto \omega^n \quad \Rightarrow \quad n = \frac{\omega\ddot{\omega}}{\dot{\omega}^2} \tag{5.20}$$

Measurements for Crab give $n = 2.515 \pm 0.005$, for Vela $n = 1.4 \pm 0.2$ (see, e.g., [21]). These values encode information about the physics involved in the pulsar slow-down. In the pure magnetic dipole case, in which (e.g., [115])

$$\dot{E} = -\frac{2}{3}\frac{d_0^2 \omega^4 \sin^2\chi}{c^3}, \qquad d_0 = \frac{\Phi r_*}{2\pi} = \frac{1}{2} B_* r_*^3 \tag{5.21}$$

(Φ is the magnetic flux and χ is the angle between the magnetic and rotational axes), one obtains $\dot{\omega} \propto \omega^3$, i.e., $n = 3$, by equating $\dot{E} = \dot{E}_{\rm rot}$. On the other hand, the torque exerted on a pulsar due to launching of a wind can be estimated by a unipolar inductor. The dissipated power of a rotating Faraday disk is given by $\dot{E} = U^2/Z$, where $U = \Phi\omega/2\pi$ is the potential difference across the magnetic field lines and Z is the resistance of a medium. In this case $\dot{\omega} \propto \omega$ ($n = 1$). In reality n should be determined by a combination of the dipole emission and the wind outflow (for discussion of this model see e.g. [208]). In the numerical simulations Contopoulos & Spitkovsky [45] showed that an important role may be played by the inclination angle χ and the angular velocity of the field lines $\omega_{\rm F}$, which, in general, is different from the pulsar rotational frequency ω. Values $n < 3$ are usually taken as a proof that the pulsar wind carries away a significant portion of the pulsar spin-down energy [21].

Another important parameter characterizing a pulsar wind is the energy per particle μ that it carries, first introduced by Michel [148] as the mass-loading parameter $\mu = L/\dot{M}c^2$. As it is a constant of the flow, its value can be determined at the light cylinder, where $J = \kappa(2J_{\rm GJ}) = \kappa(2N_{\rm GJ})ec$, and related to the multiplicity coefficient κ

$$\mu = \frac{a_{\rm L}}{4\kappa} \tag{5.22}$$

κ is not well constrained, however. According to theoretical pulsar models [83] and numerical simulations [49, 199] it is expected to be large $\sim 10^3 - 10^5$, especially for young pulsars, which, due to higher voltage, are able to create pairs by the curvature photons. Lower limits on multiplicities from the HESS observations of PSR B1823-13, PSR B1509-58 and Vela X were put by de Jager [52]. Lower limits for PSR B1823-13 and PSR B1509-58 give ~ 500 and 2000, respectively. Since these objects are not detected in radio, de Jager used also extrapolation of the spectrum to this range and, when he added the radio emitting electrons, he obtained much higher multiplicities $\sim 10^5$.

On the other hand, from the observations of the Crab nebula it is not quite clear if the radio emitting synchrotron electrons are still being injected into the nebula together with the more energetic particles, or they were supplied only at the early stages of the nebula history [159, 90]. Their lifetime is longer than the nebula age and any possibility cannot be excluded a priori. However, there are strong indications that the radio electrons are still supplied. Recent observations of wisps in the radio and optical bands [25] suggest that the electrons emitting radio photons are accelerated at present in the same regions as the ones emitting optical and X-rays. This conclusion is also implied by the analysis of Gallant & Tuffs of IR observations [61, 62]. If this is indeed the case, the total radio brightness of the Crab nebula implies multiplicities $\sim 10^6$ [174, 25], assuming equipartition of magnetic and particle energy in the nebula. This value is larger than any of those that theoretical models predict.

The last parameter characterizing pulsar winds is the magnetization σ, a ratio of the energy flux carried by the fields to that carried by the particles,

$$\sigma = \frac{B^2}{8\pi n m c^2 \gamma_{\rm w}^2} \gg 1 \tag{5.23}$$

where $\gamma_{\rm w} = (1 - \beta_{\rm w}^2)^{-1/2}$ is a wind Lorentz factor and n is a proper density of each of two plasma species $e^{\pm}$. Using (5.15), (5.16) and (5.17) one obtains $N = N_{\rm L}(r_{\rm L}/r)^2$, $B = B_{\rm L} r_{\rm L}/r$ and

$$\sigma = \frac{B_{\rm L}^2}{8\pi N m c^2 \gamma_{\rm w}} \left(\frac{r_{\rm L}}{r}\right)^2 \tag{5.24}$$

and at the light cylinder [133]

$$\sigma_{\rm L} = \frac{\omega_{\rm L}}{4\gamma_{\rm L}\kappa\omega} \tag{5.25}$$

(The factor of 2 difference in the result of the cited paper, is a consequence of our definition of density). $N_{\rm L} = \kappa N_{\rm GJ} = \kappa B_{\rm L}\omega/2\pi ec$, $\omega_{\rm L} = eB_{\rm L}/mc$ is the Larmor frequency, ω – frequency of star rotation, and $\gamma_{\rm L}$ is the wind Lorentz factor at the light cylinder. Assuming purely dipole emission from a pulsar, we estimate the magnetic field at the light cylinder according to (5.19). The Lorentz factor of the wind at the light cylinder $\gamma_{\rm L}$ is usually estimated to be a few hundred [179]. Taking for Crab $\gamma_{\rm L} \sim 100$, and the upper limit on the multiplicity implied by the observations $\kappa \sim 10^6$, we get

$$\sigma_{\rm L} \sim 100 \tag{5.26}$$

However, there is no direct measurement of σ upstream of the termination shock. Upstream values are always calculated from the jump conditions at the shock, since the observational limits on σ can be put downstream.

These parameters can be related to the conserved quantities in a striped wind. To show it, one can define the energy-momentum tensor of the wind

$$T^{\mu\nu} = T^{\mu\nu}_{\rm p} + T^{\mu\nu}_{\rm f} \tag{5.27}$$

which is a sum of the plasma and field components

$$T^{\mu\nu}_{\rm p} = mc^2 \left(n_+ u^\mu_+ u^\nu_+ + n_- u^\mu_- u^\nu_- \right) \tag{5.28}$$

$$T^{\mu\nu}_{\rm f} = \frac{1}{4\pi} \left(F^{\mu\alpha} F^\nu{}_\alpha - \frac{1}{4} g^{\mu\nu} F_{\alpha\beta} F^{\alpha\beta} \right) \tag{5.29}$$

We consider only a cold, pair plasma, that is expected to be produced in a pulsar magnetosphere, and "+/−" refers to positrons/electrons. Quasi-neutrality requires $n_+ = n_- = n$, and both the electron and positron fluids to move in the same manner, hence also $u_+ = u_- = u$. In such a wind the electromagnetic field is purely transverse. The flow as a whole expands radially, so that $u_\alpha = u_r$, and we denote it by $\beta_{\rm w}$. With these assumptions, in the laboratory frame the only nonvanishing components of the stress-energy tensor are: the energy density

$$T^{00} = 2mc^2 n \gamma_{\rm w}^2 + \frac{1}{8\pi} \left(\boldsymbol{E}^2 + \boldsymbol{B}^2 \right), \tag{5.30}$$

the energy flux

$$T^{01} = 2mc^2 n \gamma_{\rm w}^2 \beta_{\rm w} + \frac{1}{4\pi} \boldsymbol{E} \times \boldsymbol{B}, \tag{5.31}$$

and the radial momentum flux

$$T^{11} = 2mc^2 n \gamma_{\rm w}^2 \beta_{\rm w}^2 + \frac{1}{8\pi} \left(\boldsymbol{E}^2 + \boldsymbol{B}^2 \right). \tag{5.32}$$

Moreover, in the wind frame the electric field vanishes, so that in the lab frame $\boldsymbol{E} = -\boldsymbol{\beta}_{\rm w} \times \boldsymbol{B}$. The magnetic field has constant magnitude in each stripe, but changes sign across each current sheet. Thus, the flow quantities change periodically with the rotational phase. At distances much larger than a wavelength, we can consider only quantities averaged over the pulsar period (for detailed discussion see Lyubarsky & Kirk [133]). Since the energy and momentum are transported only in the radial direction, they are conserved in the spherical expansion:

$$\frac{1}{r^2} \frac{d}{dr} \left(r^2 \left\langle T^{10} \right\rangle \right) = 0 \tag{5.33}$$

$$\frac{1}{r^2} \frac{d}{dr} \left(r^2 \left\langle T^{11} \right\rangle \right) = 0 \tag{5.34}$$

Apart from these conservation laws, the mass continuity holds

$$\frac{1}{r^2} \frac{d}{dr} \left(r^2 \left\langle J \right\rangle \right) = 0 \tag{5.35}$$

where $\boldsymbol{J} = 2nc\gamma_{\rm w}\boldsymbol{\beta}_{\rm w}$ is the particle flux. Since the particle number is constant, we can write the conserved quantities in a form

$$\mu = \frac{\langle T^{01}\rangle}{mc\,\langle J\rangle} = \gamma_{\rm w}(1+\sigma) \tag{5.36}$$

$$\nu = \frac{\langle T^{11}\rangle}{mc\,\langle J\rangle} = \frac{1}{\gamma_{\rm w}\beta_{\rm w}}\left(\gamma_{\rm w}^2(1+\sigma) - 1 - \frac{\sigma}{2}\right) \approx \mu - \frac{1+\sigma}{2\mu} \tag{5.37}$$

$$\langle J\rangle\, r^2 = \frac{c\,\langle T^{01}\rangle}{mc^2\mu} r^2 = \frac{a_{\rm L}^2}{\mu}\frac{mc^3}{4\pi e^2} \tag{5.38}$$

– respectively: the energy and the radial momentum fluxes per particle, and the particle number. Here we also used $c\,\langle T^{01}\rangle = \langle F\rangle = L/4\pi r^2$.

Thus, the wind is uniquely described by three quantities: μ, σ (equivalently ν) and $a_{\rm L}$.

5.2.3 MHD shocks of pulsar winds

Since neutron stars are the final products of the supernova explosions, pulsars are surrounded by the progenitor's (unshocked) ejecta, which expand in the interstellar medium. A supersonic pulsar wind that impacts on the slowly moving ejecta, drives a forward shock, and at the same time a second shock propagates backwards in the wind, decelerating it and compressing in order to adjust its properties to the expansion of the shocked ejecta. Between the shocked wind (nebula), downstream of the backward-moving shock, and the shocked supernova ejecta, downstream of the forward shock, a contact discontinuity appears. The shape of this discontinuity is strongly distorted by Rayleigh-Taylor instability operating on the ejecta, accelerated by the pulsar-driven wind (see, e.g., [89]). The reverse shock is called the termination shock and is located at the distance, where the ram pressure of the pulsar wind is balanced by the confining pressure of the nebula. The model of supernova remnant is shown in Fig. 5.4.

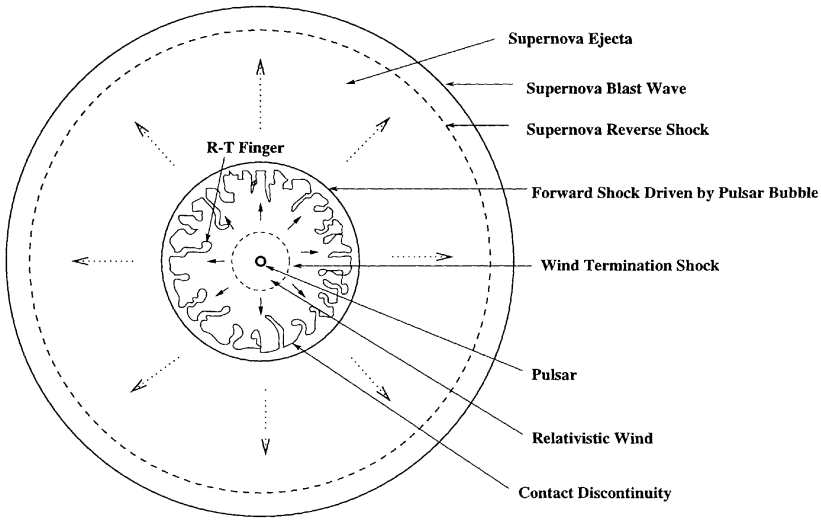

Figure 5.4: Sketch of a type-II supernova remnant. Taken from [89].

Broad-band (radio to γ-rays) observations of synchrotron radiation downstream of the termination shock suggest that a significant fraction of the pulsar spin-down power is converted into particles. In a consistent picture they are carried by a wind away from a pulsar magnetosphere, and they are injected into the nebula at the termination shock. In the Crab spectrum synchrotron emission extends up to a few hundred MeV. At higher energies, up to a few TeV, emission is attributed to the IC scattering of the synchrotron photons. The implied energies of

electrons, which reproduce the Crab spectral energy distribution, are in the range ≤ 100 MeV to ~ 1 PeV. Most of the energy density is in the particles with energies ~ 100 GeV, but, at the same time, majority of the particles is in the low-energy range. The acceleration process that would reproduce these features is not well understood (for detailed discussion see, e.g., [100]). In the standard shock acceleration mechanisms only a fraction of the total available energy is converted to very few energetic particles. An interesting possibility was noted by Lyubarsky [134], according to which the nonthermal low-energy component is produced at the shock during reconnection of the alternating magnetic field in the striped wind. It predicts formation of a particle spectrum that would reproduce the flat observed distribution of the radio and IR emitting particles in the nebula. On the other hand, the high energy tail, in the Crab spectrum – above 1 TeV, may be produced in the first order Fermi process, as discussed in [100]. They note that (1) annihilation of the alternating magnetic field may indeed leave a turbulent, small-scale magnetic field, which, in turn, may provide a scattering medium for the 1st order Fermi process; (2) however, this mechanism of particle acceleration is not very efficient at perpendicular shocks until the cross-field diffusion occurs; (3) interestingly, for isotropic diffusion of accelerated particles it predicts the energy spectrum with an index -2.2, which well explains the X-ray Crab spectrum.

5.2.4 σ-problem

Above in Eq. 5.26 we estimate the magnetization parameter of a wind at the light cylinder, assuming the wind Lorentz factor of the order of a hundred. Initially, however, a plasma created by ultrarelativistic primary particles accelerated in a polar gap, is expected to move subsonically. Such a flow in the force-free approximation accelerates with radius as $\gamma_{\rm w} \propto r$ [100] till it reaches the fast magnetosonic speed, which, for magnetically dominated flow $\sigma \gg 1$, is determined by $\gamma_{\rm fms} = \sqrt{\sigma}$ [99]. Because in a radial flow B^2/N is constant, $\sigma \propto 1/\gamma_{\rm w} \propto 1/r$ as the flow accelerates. It passes the magnetosonic point somewhere close to the light cylinder[3] [133]. From that point the wind has to be described by full relativistic MHD (not only force-free, because propagation of the fast magnetosonic wave is an interplay between particle inertia and magnetic tension, implying that the former already is important) [100]. In this MHD wind the outward pressure gradient of the magnetic field lines is exactly balanced by the inward tension force, hence the flow is ballistic (i.e., its speed is constant) and σ does not decrease. The electromagnetic energy is not transferred to the plasma any longer. Therefore, all the way up to the termination shock, the magnetization of the ideal MHD wind retains its initial value $\sigma_{\rm L} \gg 1$.

The observational limits can be put on σ only downstream of the termination shock. There are two ways to do this. Firstly, a downstream flow should match to the nonrelativistic expansion of a nebula [90]. Secondly, the same value of magnetization which is determined by this boundary condition, must also account for the intensity, spatial distribution and the correct spectral index of the nebular synchrotron radiation [91].

Since the wind has to match to the nonrelativistically expanding nebula, it must be decelerated at the termination shock, beyond which the communication with the outer edge of the nebula is maintained by the sound waves [174]. This communication will adjust a subsonic shocked flow to the expansion speed of the outer edge of the nebula. Deceleration of the wind can be determined from the Rankine-Hugoniot jump conditions across the perpendicular MHD shock. The downstream quantities, expressed in terms of σ, have very different behavior, depending on the value of magnetization [90]. When $\sigma > 1$ an MHD shock is weak, in the sense that, despite the large jump of the flow velocity across the shock, the downstream value is still relativistic $\sim \sqrt{\sigma}$, and, consequently, the downstream pressure is magnetically dominated. All the energy released at the shock goes to a small build up of the magnetic field strength, according to the magnetic flux conservation. Only for $\sigma < 0.1$ the significant energy can be dissipated into the plasma, which gives it off in a synchrotron process. For the Crab nebula Kennel &

[3]Since $\gamma \sim \gamma_* r/r_*$ and $r_{\rm L} \approx 10^2 r_*$ one can estimate that $\gamma \sim \gamma_{\rm L} \sim 10^2$ when $r \sim r_{\rm L}$.

Coroniti [90] estimated the averaged nebular expansion velocity and pressure from observations, and comparing them with the solution of the Rankine-Hugoniot conditions at the termination shock in the limit of small σ, they obtained a best-fitting value $\sigma \approx 3 \times 10^{-3}$.

An independent way of estimating σ is provided by investigation of the synchrotron-emitting electrons. Kennel & Coroniti [91] assumed the power-law distribution of particles in the downstream region and required it to satisfy the Rankine-Hugoniot jump conditions at the shock. This enabled them to connect the synchrotron radiation of the nebula with the pulsar wind parameters. Next, this synchrotron spectrum, calculated as a function of σ, wind four-velocity u and a photon index α, was evolved in space, assuming adiabatic expansion and synchrotron energy losses, and compared with the observations of the continuum from optical to γ-rays. The authors were able to constrain u from the requirement that the downstream flow radiates the total observed nebular luminosity. In particular, they found that it is possible only in the models with small σ and high u. From their analysis of the photon index, they concluded that the MHD model of the flow transport correctly describes the observations. Kennel & Coroniti investigated also the extend to which the value $\sigma = 3 \times 10^{-3}$ can reproduce the spatial and spectral distribution of the Crab nebula continuum. The spatial size of the nebula is a result of an interplay between the efficiency of radiation losses in the flow and its speed in the downstream region. The high-σ flows have rapid synchrotron burn-off, but at the same time they are relativistic downstream so that moderate-energy particles, emitting UV and X-ray photons, can flow to large distances from the shock; when σ is low, the burn-off is not severe, but the shocked flow is slow and X-rays can be emitted only close to this shock. Hence, in general, low-σ flows have more compact X-ray emission. For the best fitting value $\sigma = 3 \times 10^{-3}$, $u = 3 \times 10^6$ seemed to satisfactorily reproduce all the features, being also consistent with the earlier estimates.

Summarizing, the magnetization in the downstream region must be very small to reproduce the observations. Therefore, there must be a mechanism at work that allows a transition between high- and low-σ regimes in the wind expansion, but its nature is unclear. This is known as the "σ-problem". A solution can be found only by looking beyond the ideal MHD description.

Lyubarsky [134] proposed that in the case of a striped wind the upper limits on σ, found from the MHD jump conditions, should be related not to the total Poynting flux in the flow, but to its fraction, associated with the average magnetic field. Upstream, the wind is Poynting-flux dominated indeed, but as long as the electromagnetic energy is carried by the alternating magnetic field, it will be released into the plasma when the field lines annihilate at the shock. This reconnection might result from the abrupt deceleration of the wind, caused by the pressure of the hot downstream plasma and magnetic field. The crucial point is the difference between the collisionless MHD shock and the striped wind shock. In the former, the downstream pressure is determined by the downstream temperature, which is roughly the upstream particle kinetic energy. Downstream particles penetrate the shock on the Larmor radius and, therefore, decelerate the flow on this lengthscale. In the second case, the downstream pressure is exerted by the particles that gained the energy from the annihilating magnetic field, so their energy exceeds the upstream kinetic energy. Their Larmor radius exceeds the upstream Larmor radius (and also the stripe width) – thus the deceleration scale is longer. In the proper frame the annihilation looks as if the upstream plasma was compressed by an external force. When the alternating field dissipates completely, the particle Larmor radius becomes equal to the shock width, and the shock behaves as a standard MHD one. This scenario is also attractive, because, as already mentioned, it predicts that the particles produced at the striped wind shock have a very flat distribution, in which the energy of a majority of the particles is less than the upstream particle kinetic energy.

Another possibility is a scenario, in which the MHD wind converts into a large-amplitude strong electromagnetic (EM) wave before reaching the shock [200, 146]. This mode is able to accelerate particles to relativistic energies in a plane transverse to the direction of motion and, therefore, to transfer the flow energy from the fields into the plasma. In the following we discuss

the details and closely investigate this solution for the σ-paradox.

5.3 Relativistically strong waves in pulsar winds

First suggestions of the presence of large-amplitude electromagnetic waves in pulsar's surroundings appeared in papers of Pacini [158] and Gunn & Ostriker [76], who attributed pulsar spin-down to the emission of dipole radiation at the rotational frequency. Pulsar periods range from milliseconds to almost ten seconds, which implies extremely low radio frequencies of the emitted radiation. According to the model of Gunn & Ostriker, such a wave when launched by a misaligned dipole, would propagate in a vacuum. It was also realized that its great intensity should be responsible for strong acceleration, as it always imparts relativistic speeds to the particles [77]. Moreover, motion of a test charge in the large-amplitude fields of an electromagnetic wave is strongly affected by radiation reaction, a consequence of the nonlinear inverse Compton scattering. Wave intensities estimated from the pulsar parameters lead to the emission spectrum resembling closely the synchrotron one. Gunn & Ostriker suggested that the continuum emission from the Crab nebula can be explained by this process.

Also Rees [173] considered the same mechanism for the nebular emission. He noted that the dipole radiation is linearly polarized at the equator and circularly polarized along the rotational axis. Radiation from the other latitudes has elliptical polarization. This property implies that also the NIC radiation is polarized. Uniform direction of polarization from the inner nebula supported this idea, since the linear component has the same direction at all latitudes. However, a contribution from the polar regions was predicted to give a few percent of circular polarization in radio, optical and X-rays. Measurements of Landstreet & Angel [116] showed that no such polarization appears, making the model rather improbable. On the other hand, the observations excluded only the vacuum dipole radiation. Additionally, model of the pulsar magnetosphere proposed by Goldreich & Julian [71] brought into consideration the prolific pair production and the existence of a plasma around a rotating neutron star. The need for a self-consistent treatment of large-amplitude electromagnetic waves propagating in plasmas was realized. Early papers, however, showed that the propagation of such waves in the vicinity of pulsars is strongly restricted, e.g., [142].

The aforementioned restrictions have several origins. (1) Firstly, the plasma, produced in a magnetosphere and outflowing through the light cylinder, is overdense, and the propagation condition for large-amplitude EM waves cannot be satisfied close to the light cylinder (see section 5.3.1). (2) Secondly, investigations of the possible wave damping mechanisms showed that the waves are quenched almost immediately after the launch. Radiation damping due to the synchro-Compton (i.e., nonlinear inverse Compton) process, studied by Asseo et al. [15], seemed to be able to damp a wave within a few wavelengths. (3) Finally, superluminal modes were shown to be unstable against density perturbations in the direction of motion [141, 55, 178, 118]

For these reasons, strong electromagnetic waves went out of fashion in modelling of pulsar winds. Kennel & Coroniti [90, 91] constructed a purely MHD model of a wind, its termination shock and a nebula. In this description the entire post-supernova system is tightly coupled, in particular, an MHD pulsar wind is responsible for loading a nebula with particles and large-scale magnetic fields. Assumption that the particles are accelerated at the MHD shock reproduces the nebular synchrotron emission from optical to X-rays, and the relativistic MHD simulations [110] explain the observed nebular morphology. These models, however, are known to suffer from several serious problems, from which still unknown is the solution for the σ-paradox. As suggested in [200, 146], and investigated in details in [97, 10], strong EM waves may be capable of providing such a solution, because they effectively accelerate particles at the expense of the electromagnetic energy.

Since an overdense plasma prohibits the EM wave propagation close to a pulsar (even in a

strong-wave regime), Kirk [97] proposed the model which assumes that from the light cylinder it is the striped wind that emerges, but further, before reaching a shock, it converts into an EM wave, when the propagation of this mode becomes possible due to the decrease of the plasma density with a distance. Due to the great complexity of the physics involved, the mode conversion process itself has not been considered so far. Presumably it can be investigated only in two-fluid or PIC simulations. However, just like in the case of an MHD shock, the transition from one mode to another can be described without using the microphysics, by solving the jump conditions across the transition region [97, 10].

In fact, there is also a loophole in the results that concern the damping of strong waves. The fast damping rate due to the NIC process, reported by Asseo et al. [15], was considered only in the case of linear polarization. They used the expansion in a small parameter q, defined as the ratio of the energy density in fluids to that in the electric field, evaluated at the phase at which the field has the maximum [93]. Arka & Kirk [10] noted that in fact this phase is very special and it corresponds to the turning points of the sawtooth waveform. These points cannot determine the average properties of the wave and expansion of the fluxes, carried by the wave, in the limit $q \to 0$ is not appropriate in pulsar conditions.[4] Consequently, the damping of strong waves is not as rapid as previously thought. In a general case, a wave can propagate over many wavelengths, slowing down with the distance. Finally, when the streaming of the particles through the wave is sufficiently slow, instabilities are expected to set in [118, 178, 184]. They can disrupt the wave within only one period. Such a rapid disruption provides, in turn, a natural mechanism that leads to formation of the shock, where the energy is randomized and deposited into the particles.

Thus, by re-examining the properties of strong EM waves and their ability to propagate in pulsar winds, we can construct a new, fully consistent picture, in which the superluminal modes are launched not close to the pulsar, but they play a role in formation of the termination shocks. In pulsar conditions these waves are not plane, but spherical, and in a self-consistent solution the spherical geometry should be accounted for. The radial evolution of strong, linearly polarized modes, was investigated by Asseo et al. [17], who used a perturbative approach to expand the nonlinear equations is a small parameter $\epsilon = \lambda/r \ll 1$ (short-wavelength approximation). The lowest order equations gave the known self-consistent, plane wave solution, and the effects of spherical geometry appeared in the first order. However, in their calculations one of the Christoffel symbols for the spherical geometry was omitted, and, as a result, the radial momentum of the flow appeared to be a conserved quantity. This is not the case when the calculation is corrected, and, as a consequence, radial evolution of the wave quantities is different than reported.

These problems motivate a new investigation of the properties of large-amplitude EM waves. Our contribution will be presented in the next chapter. Here, in the remaining two sections, 5.3.1 and 5.3.2, we discuss the critical distance [97], beyond which strong EM waves can propagate in pulsar winds, and we summarize the jump conditions that determine the mode conversion process [10].

5.3.1 Propagation condition

As discussed in Sect. 2.2.3, a plasma can support the electromagnetic wave propagation, when the wave frequency is larger than the proper plasma frequency. In the lab frame

$$\frac{\omega'^2}{\omega_{\rm p}^2} \geq \frac{1}{\gamma} \tag{5.39}$$

[4]Most readily it can be shown for a circularly polarized wave, for which all the quantities are phase independent. Since q, Eq. 2.69, is a Lorentz invariant, we can calculate it in the special frame (where $\omega = \omega_{\rm p}$):

$$q = \frac{32\pi\gamma_0^2 n_0 mc^2}{E_0^2} = 4\frac{\omega_{\rm p}^2}{\omega^2}\frac{\gamma_0^2}{a^2} = 4\frac{1+a^2+p_{\parallel 0}^2}{a^2} > 4$$

In pulsars, the frequency of a wave is fixed, and determined by the rotational frequency ω' (here we add "prime", because later we use it to denote the quantities measured in the lab frame), but the plasma density (and, what follows, the plasma frequency) decreases with the distance from a pulsar. Therefore, it is more appropriate to express the propagation condition in terms of a critical radius rather than a critical frequency [97, 10].

The critical radius is defined as the one beyond which an electromagnetic strong wave, emitted by a pulsar, can propagate. Up to that point the wind density, as measured in the lab frame, drops as $N = N_{\rm L}(r_{\rm L}/r)^2$ with $N_{\rm L} = \kappa N_{\rm GJ} = \kappa B_{\rm L}\omega'/2\pi ec$, and we get

$$\frac{\omega'^2}{\omega_{\rm p}^2} = \frac{\omega'^2}{8\pi e^2 N/m} = \frac{r^2}{r_{\rm L}^2}\frac{1}{4\kappa a_{\rm L}} \tag{5.40}$$

where we also used the definition $a_{\rm L} = eB_{\rm L}/mc\omega'$. On the other hand, the flow is required to carry the finite energy flux per particle, so that a launched EM wave cannot impart to the particles arbitrarily large Lorentz factors, but the condition $\gamma < \mu$ must hold. It yields

$$\frac{\omega'^2}{\omega_{\rm p}^2} > \frac{1}{\mu} \tag{5.41}$$

When comparing these two expressions and using (5.22), we find it convenient to define

$$R = \rho\frac{\mu}{a_{\rm L}} = r\frac{\omega'}{c}\frac{\mu}{a_{\rm L}} \tag{5.42}$$

for which the propagation condition is $R > 1$, where $R_{\rm cr} = 1$ ($\rho_{\rm cr} = 4\kappa$) is the critical radius.

As already mentioned, this distance $\rho_{\rm cr}$ is smaller than $\rho_{\rm max} = \pi a_{\rm L}/2$, beyond which the available charge carriers in the striped wind are unable to carry the necessary current to keep the MHD approximation valid. In particular, for the Crab pulsar with a multiplicity $\kappa \sim 10^6$, and the termination shock at the distance $\rho_{\rm ts} \approx 10^9$, one gets $\rho_{\rm cr} \sim 4 \times 10^6 \ll \rho_{\rm ts}$ and $\rho_{\rm max} \sim 5 \times 10^{10} \gg \rho_{\rm ts}$.

Since the critical radius can be much smaller than the distance to the termination shock, a possibility arises that a strong wave is launched in front of the shock. In principle, it may happen either spontaneously, or as a result of the boundary conditions imposed on a pulsar wind by the downstream medium. In the latter case, one can think of an EM wave as a shock precursor. In a physical picture it is causally connected to the surroundings, which means that the information about a pressure perturbation in the external medium can reach the wind fast enough to enable its adjustment, by launching of the precursor.

5.3.2 Conversion

A strong EM wave, which emerges from this conversion process, carries the same energy, radial momentum and particle fluxes as a striped wind [97, 10]. Conservation of these fluxes in a flow leads to the jump conditions, in analogy with the familiar jump conditions, solved usually for MHD shocks. Unlike for the shocks, however, there is no plasma heating involved in the mode transition, but the entropy is generated as the new, perpendicular degrees of freedom appear.

It is convenient to introduce the energy-momentum tensor of a self-consistent electromagnetic wave $T^{\mu\nu}$. In analogy to the striped wind case, one can express it is a sum of the particle (5.28) and the field (5.29) components. In the special, homogeneous frame[5] these components are

[5]This is a frame moving with the wave group speed, where no spatial dependence appears, and the electromagnetic field is purely electric. See Sect. 2.2.1.

explicitly given by [10]

$$T^{00} = 2mc^2 n\gamma^2 + \frac{E^2}{8\pi} \tag{5.43}$$

$$T^{10} = 2mc^2 n\gamma p_{\parallel} \tag{5.44}$$

$$T^{11} = 2mc^2 n p_{\parallel}^2 + \frac{E^2}{8\pi} \tag{5.45}$$

$$T^{22} + T^{33} = 2mc^2 n p_{\perp}^2 \tag{5.46}$$

The particle flux in this frame is

$$J = 2ncp_{\parallel} \tag{5.47}$$

Since the particle flux is conserved in the transition, one can write the jump conditions in terms of the fluxes per particle, in an MHD wind defined by μ (5.36) and ν (5.37). On the other hand, they are given by the stress-energy tensor of an EM wave:

$$\left\langle J' \right\rangle R^2 = \frac{\mu mc\omega'^2}{4\pi e^2} \tag{5.48}$$

$$\mu = \frac{\left\langle T'^{01} \right\rangle}{mc^2 \left\langle J' \right\rangle} \tag{5.49}$$

$$\nu = \frac{\left\langle T'^{11} \right\rangle}{mc^2 \left\langle J' \right\rangle} \tag{5.50}$$

where we also used definition (5.42).

Prime denotes quantities measured in the laboratory frame. To obtain the fluxes in this frame, one can Lorentz transform the ones from the homogeneous frame [10]

$$J' = \gamma_*(2c\beta_* n\gamma + J) \tag{5.51}$$

$$T'^{00} = \gamma_*^2 \left[T^{00} + 2\beta_* T^{01} + \beta_*^2 T^{11})\right] \tag{5.52}$$

$$T'^{10} = \gamma_*^2 \left[(1+\beta_*^2)T^{10} + \beta_*(T^{00} + T^{11})\right] \tag{5.53}$$

$$T'^{11} = \gamma_*^2 \left(T^{11} + 2\beta_* T^{10} + \beta_*^2 T^{00}\right) \tag{5.54}$$

$$T'^{22} = T^{22} \tag{5.55}$$

$$T'^{33} = T^{33} \tag{5.56}$$

If the phase-averaged magnetic field does not vanish in a flow, jump conditions (5.48), (5.49), (5.50) are complemented by the magnetic flux conservation [10]

$$\eta = \frac{\left\langle E' \right\rangle^2 / 4\pi}{mc^2 \left\langle J' \right\rangle} \tag{5.57}$$

where $\eta = \sigma\beta_{\rm w}\gamma_{\rm w} \left\langle B' \right\rangle^2 / \left\langle B'^2 \right\rangle$ is the averaged magnetic field in an MHD wind. In fact, the average of the field vanishes only in the equatorial plane (where the stripes have equal width) and increases towards higher latitudes. It achieves its maximum value when the latitude is equal to the inclination angle between the rotational and magnetic axes of a pulsar. Since the magnetic flux is conserved during the mode conversion process, it contributes also to the total energy and momentum of a strong EM wave, thus the new terms in the components (5.43), (5.44), (5.45) of the stress-energy tensor must be taken into account.

Arka & Kirk [10] solved the algebraic equations (5.48), (5.49), (5.50) and (5.57) numerically for both linearly and circularly polarized waves. In the latter case, if $\eta = 0$, also an analytic

solution is available [97]. Alternatively, instead of solving algebraic equations one can integrate the ordinary differential equations that express the conservation laws:

$$\frac{d}{dR}\left(R^2 \left\langle J' \right\rangle\right) = 0 \tag{5.58}$$

$$\frac{d}{dR}\left(\frac{\left\langle T'^{01} \right\rangle}{\left\langle J' \right\rangle}\right) = 0 \tag{5.59}$$

$$\frac{d}{dR}\left(\frac{\left\langle T'^{11} \right\rangle}{\left\langle J' \right\rangle}\right) = 0 \tag{5.60}$$

The initial conditions for integration are given by the MHD wind parameters. The results for circularly polarized waves are plotted in Fig. 5.5. Red curves trace the wave Lorentz factor

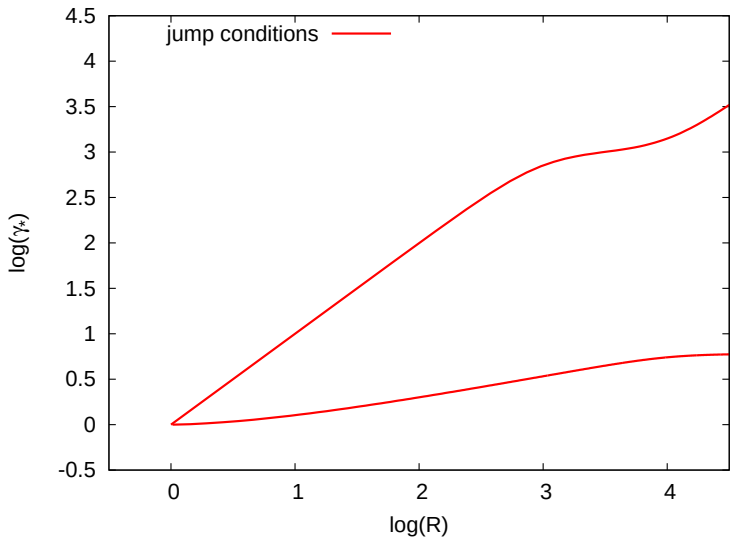

Figure 5.5: The Lorentz factor of a circularly polarized strong wave that is launched from an MHD wind with $a_{\rm L} = 3.4 \times 10^{10}$, $\mu = 10^4$, $\sigma = 100$, $\eta = 0$. The Lorentz factor is implied by the jump conditions between these two modes (R is the conversion radius).

at launch as a function of the conversion radius. For a given conversion radius there are two solutions of the jump conditions, which define two possible modes: the confined (lower branch) and the free-escape one (upper branch).

Chapter 6

Superluminal waves in pulsar winds

In this chapter we present our studies of the nonlinear electromagnetic modes in pulsar winds – in particular their role in the formation of termination shocks. The motivation is to gain new insight into the shock structure, providing a self-consistent picture, that is free of the σ-problem.

In section 6.1 we investigate the radial propagation of a spherical wave, for both circular and linear polarizations, for the case of a vanishing averaged magnetic field. Similar to our study of magnetic shear in blazar jets, we use a perturbative approach, in which the spherical effects are treated as a perturbation to the known, plane wave solution. We find that the total energy and the particle number are conserved during expansion, but the radial momentum changes due to the motion of particles in the perpendicular plane. Consequently, the wave slows down as it propagates and the ram pressure of the outflow converges to a constant value at large radii. For a generic solution this value should be equal to the pressure of the external medium.

In section 6.2 we find that matching of a wave to the surroundings can be obtained from a set of algebraic equations, due to the existence of a conserved quantity in the flow that connects the asymptotic values of the wave parameters, fixed by the medium pressure, with those at the launch site. The latter are determined from the striped wind μ, σ, $a_{\rm L}$, but the conversion radius is not constrained uniquely. Since only the wave that is launched at a specific radius has the required asymptotic pressure, the matching procedure allows us to define the conversion radius uniquely. We find that the integral of motion for this system is the phase-averaged particle Lorentz factor, measured in the laboratory frame. The main conclusion is that the shock precursor is determined not only by the MHD wind parameters, but also by the pressure of the external medium. Thus, in our scenario, the mode conversion process is determined by the boundary conditions, which the striped wind itself cannot satisfy.

Further in section 6.3 we examine damping of strong waves due to the nonlinear inverse Compton process. This effect is also treated as a perturbation to the known, plane wave solution. Since the drag force due to radiation reaction depends on the wave amplitude, and that, in turn, is determined by the external pressure when the wave is launched, we find that the efficiency of the wave damping is determined by the pressure of the surrounding medium. Winds of isolated pulsars, confined by the low-pressure nebulae, are not affected by the radiative damping. However, for a pulsar/Be-star binary system, where the high-pressure environment is guaranteed by the wind of a companion star, the interaction of particles with photons can be very efficient and the wave may diminish very quickly after it has been launched. In our model, the wave slow-down due to spherical expansion and radiation damping, is followed by the instabilities that can set in when the streaming of the particles through the wave becomes sufficiently small. The point where the streaming vanishes we identify with the shock, beyond which the wave is disrupted and its energy is randomized. We find the expression for the fraction of the total energy that is radiated before the shock is formed and it turns out to be dependent only on the external pressure. Finally, we apply this model to the binary PSR B1259-63.

6.1 Radial propagation

In analogy to the subluminal waves in blazar jets, we investigate here the radial propagation of a superluminal wave using perturbation analysis. The lowest and the first order equations can be obtained directly from the previous analysis by putting $M = 0$ and $a = 0$, i.e. neglecting the spacetime curvature caused by the presence of a rotating mass.

The two different timescales, on which the outflow quantities change, are the following: a short one – determined by the pulsar rotation period $P = 2\pi/\omega'$, and a long one $t \gg P$, on which the wave parameters evolve slowly due to the spherical expansion. A fast variable given by the WKB-like phase of a wave takes a form

$$\phi = \omega' \left(t - \int^r \frac{dr'}{c\beta(r')} \right) \tag{6.1}$$

where $\beta = 1/\beta_*$ is the superluminal phase velocity of a wave, β_* is the subluminal group speed. The slow radial variable is defined by the light cylinder distance $r_{\rm L}$ as

$$\rho = \epsilon \frac{r}{r_{\rm L}} \tag{6.2}$$

where $\rho \sim 1$ and $\epsilon = r_{\rm L}/r \ll 1$ is a small parameter (the short wavelength approximation).

In the next step we change the independent variables from (t, r) into the new coordinates (ϕ, ρ). The time and space derivatives are expressed in terms of ϕ and ρ as

$$\frac{\partial}{\partial t} \to \omega' \frac{\partial}{\partial \phi} \tag{6.3}$$

$$\frac{\partial}{\partial r} \to \epsilon \frac{\omega'}{c} \frac{\partial}{\partial \rho} - \frac{\omega' \beta_*}{c} \frac{\partial}{\partial \phi} \tag{6.4}$$

$$\gamma' \frac{d}{dt} \to \epsilon \frac{\omega'}{c} p'_{\parallel} \frac{\partial}{\partial \rho} - \omega' \Delta' \frac{\partial}{\partial \phi} \tag{6.5}$$

where $\Delta' = \gamma' - \beta_* p'_{\parallel}$.

Expanding all the dependent variables to the first order, i.e. $\gamma' = \gamma'^{(0)} + \epsilon \gamma'^{(1)}$ etc., and substituting (6.3), (6.4) and (6.5) into the fluid and Maxwell equations, one obtains a set of equations that describes the system in the lowest, and in the first order. Since we already know the lowest order solution for the strong, plane waves (see Sect. 2.2.4), we can concentrate on the radial evolution governed by the first order equations.

They, in turn, are equivalent to the conservation of the energy-momentum tensor $\nabla_\mu T'^{\mu\nu} = \partial_\mu T'^{\mu\nu} + \Gamma^\mu_{\mu\alpha} T'^{\alpha\nu} + \Gamma^\nu_{\mu\alpha} T'^{\mu\alpha} = 0$, where the Christoffel symbols for the spherical geometry (in the orthonormal basis the coordinates are denoted by numbers) are given by (e.g. [152], p. 213)

$$\Gamma^1_{22} = \Gamma^1_{33} = -\Gamma^2_{21} = -\Gamma^3_{31} = -\frac{1}{r}, \quad \Gamma^2_{33} = -\Gamma^3_{23} = -\frac{\cot\theta}{r}, \qquad \frac{1}{r} = \frac{\omega'}{c}\frac{\epsilon}{\rho} \tag{6.6}$$

In the first order, one obtains

$$\frac{\partial}{\partial \phi} T'^{0\nu}_{(1)} + \frac{\partial}{\partial \rho} T'^{1\nu}_{(0)} + \frac{2}{\rho} T'^{1\nu}_{(0)} - \delta^\nu_1 \frac{1}{\rho} \left(T'^{22}_{(0)} + T'^{33}_{(0)} \right) + \frac{\cot\theta}{\rho} T'^{2\nu}_{(0)} - \delta^\nu_2 \frac{\cot\theta}{\rho} T'^{33}_{(0)} = 0. \tag{6.7}$$

Next, we average (6.7) over the phase. Elimination of secular terms demands all the first order quantities be periodic, thus the first term vanishes immediately

$$\int_0^{2\pi} \frac{\partial}{\partial \phi} T'^{0\nu}_{(1)} d\phi = 0 \tag{6.8}$$

For the component $\nu = 0$ and $\nu = 1$ we get the energy and momentum equations, respectively

$$\frac{1}{\rho^2}\frac{d}{d\rho}\left(\rho^2 \left\langle T'^{10}_{(0)} \right\rangle\right) = 0 \tag{6.9}$$

$$\frac{1}{\rho^2}\frac{d}{d\rho}\left(\rho^2 \left\langle T'^{11}_{(0)} \right\rangle\right) = \frac{1}{\rho}\left\langle T'^{22}_{(0)} + T'^{33}_{(0)} \right\rangle \tag{6.10}$$

They are complemented by the continuity equation $\nabla_\mu J'^\mu = \partial_\mu J'^\mu + \Gamma^\mu_{\mu\nu} J'^\nu = 0$, which in the same manner, in the first order, gives

$$\frac{1}{\rho^2}\frac{d}{d\rho}\left(\rho^2 \left\langle J'^1_{(0)} \right\rangle\right) = 0 \tag{6.11}$$

Note that the transverse momenta of the fluids ensure that T'^{22} and T'^{33} do not vanish, and the terms involving Christoffel symbols Γ^1_{22} and Γ^1_{33} contribute (as opposed to the case of an MHD wind). As a consequence, radial momentum (6.10) of a flow is not conserved (i.e., the radial momentum flux does not decrease as r^{-2}). It reflects the fact that the flow does work in both the parallel and transverse directions, and, even that the total energy is conserved, its division between the parallel and transverse degrees of freedom changes.

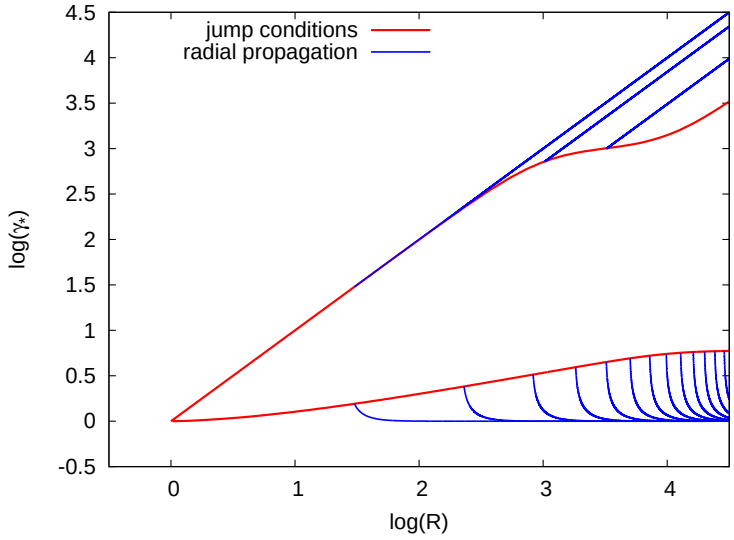

Figure 6.1: The Lorentz factor of a circularly polarized strong wave that is launched from an MHD wind with $a_{\rm L} = 3.4 \times 10^{10}$, $\mu = 10^4$, $\sigma = 100$, $\eta = 0$. Red curves show the Lorentz factor implied by the jump conditions, and the blue curves show the radial propagation of a wave, launched at a point on the red curve.

Radial evolution of the wave Lorentz factor, obtained by integration of (6.9), (6.10) and (6.11), is shown in Fig. 6.1. As before, red curves show the wave Lorentz factor at launch as a function of the conversion radius. Blue curves trace the radial evolution of the wave Lorentz factor, launched at a point on the red curve. The propagation is very different for each of two superluminal modes: at large distances the free-escape wave accelerates, whereas the confined one decelerates. The latter may have an application to the pulsar wind nebulae, which confine the wind outflows, demanding its slow-down to the nonrelativistic speeds at the termination shocks. In the following we concentrate on this mode.

6.2 Matching to the external pressure

By integrating equations (6.9), (6.10), and (6.11), one obtains the radial evolution of the quantities measured in the special (homogeneous) frame (see §2.2.1): $\beta_*(R)$, $p_\perp(R)$, $p_\parallel(R)$ for

circular polarization, or $\beta_*(R)$, $q(R)$, $p_\parallel(R)$ for linear polarization. As discussed in Sect. 5.3.2, to find the initial conditions for integration, one has to solve jump conditions between an MHD and an EM wave, to ensure that they carry the same particle, energy and radial momentum fluxes [97, 10]. However, the conversion radius is not constrained uniquely, and, since the mode conversion is causal, an additional equation should encode information about the physical conditions in the surroundings. This information is the external pressure $p_{\rm ext}$, to which the wind pressure $\langle T'^{11}\rangle$ should match. Since the wind impacts on the surroundings very far from the pulsar, e.g., in the Crab case the nebula is located beyond $10^9 r_{\rm L}$, a generic solution converges to the external pressure asymptotically $R \to \infty$. We find that it is possible to connect the asymptotic pressure of a wave with its initial parameters, because $\langle\gamma'\rangle$ is conserved during the spherical expansion, for both the circular and linear polarizations. We show it in the next section 6.2.1. Taking advantage of this integral of motion, the full set of algebraic equations that determine uniquely the initial parameters of a wave, is as follows

$$\begin{aligned}\langle J'\rangle &= \left\langle 2np'_\parallel \right\rangle \\ &= \mu\langle F'\rangle = \frac{2n\omega'^2 a_L^2}{\rho^2\omega_p^2\mu} = \frac{2n\mu\gamma_*^2}{R^2}\end{aligned} \tag{6.12}$$

$$\mu = \frac{\langle T'^{10}\rangle}{mc^3\langle J'\rangle} \tag{6.13}$$

$$\nu = \left.\frac{\langle T'^{11}\rangle}{mc^2\langle J'\rangle}\right|_0 \tag{6.14}$$

$$\langle\gamma'\rangle|_0 = \langle\gamma'\rangle|_\infty \tag{6.15}$$

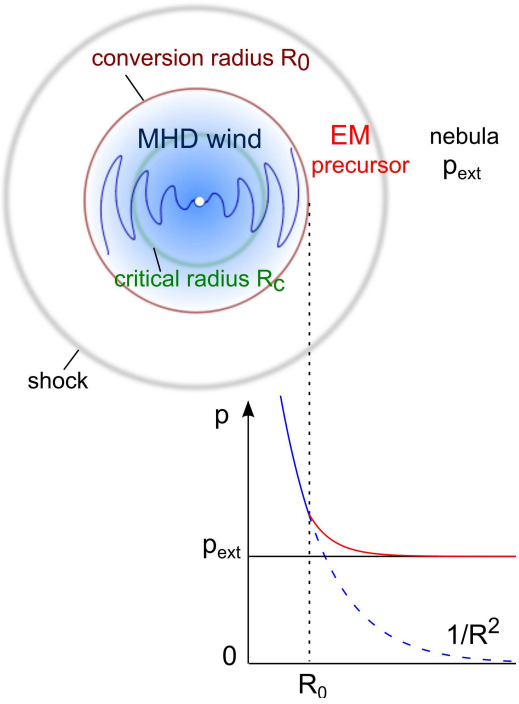

Figure 6.2: Sketch of the model. An MHD striped wind converts at the conversion radius R_0 to an EM precursor before reaching the shock. The pressure of the striped wind drops as $1/R^2$ (blue line), whereas the pressure of the precursor asymptotically goes to a constant value (red line), allowing smooth matching to the external value $p_{\rm ext}$.

6.2.1 Conservation of $\langle\gamma'\rangle$

Here we omit all "0" subscripts – wherever quantities come out of averaging, they should be understood as phase independent. Thus, according to the calculations shown in Sect. 2.2.4, we

use $\langle p_\parallel \rangle = p_{\parallel 0} \equiv p_\parallel$, $\langle n\gamma \rangle = n_0\gamma_0 \equiv n\gamma$.

By taking

$$\langle T'^{10} \rangle = 2mc^2\gamma_*^2 \left[(1+\beta_*^2) n\gamma p_\parallel + \beta_* \left(n\gamma \langle \gamma \rangle + \frac{\langle E^2 \rangle}{8\pi mc^2} + p_\parallel^2 \langle n \rangle \right) \right] \tag{6.16}$$

$$\langle T'^{11} \rangle = 2mc^2\gamma_*^2 \left[2\beta_* n\gamma p_\parallel + \frac{\langle E^2 \rangle}{16\pi mc^2}(1+\beta_*^2) + p_\parallel^2 \langle n \rangle + n\gamma\beta_*^2 \langle \gamma \rangle \right], \tag{6.17}$$

multiplying (6.9) by β_*, and subtracting (6.10), we get

$$\frac{2}{R}\left(\beta_* n\gamma p_\parallel + \frac{\langle E^2 \rangle}{16\pi mc^2} + p_\parallel^2 \langle n \rangle \right) + \frac{d}{dR}\left(\frac{\langle E^2 \rangle}{16\pi mc^2} + p_\parallel^2 \langle n \rangle + \beta_* n\gamma p_\parallel \right) + \frac{d\beta_*}{dR}\gamma_*^2 \left[(1+\beta_*^2) n\gamma p_\parallel + \beta_* n\gamma \langle \gamma \rangle + \frac{\beta_* \langle E^2 \rangle}{8\pi mc^2} + \beta_* p_\parallel^2 \langle n \rangle \right] = \frac{\langle np_\perp^2 \rangle}{R} \tag{6.18}$$

First simplification comes from the fact, that the term on the RHS is cancelled by the second term on the LHS. It is straightforward for the circular polarization, since

$$|p_\perp| = \frac{e|E|}{mc\omega} \qquad \rightarrow \qquad \frac{\langle E^2 \rangle}{8\pi mc^2} = \frac{E^2}{8\pi mc^2} = \frac{\omega^2}{\omega_p^2} np_\perp^2 = np_\perp^2 \tag{6.19}$$

where we used $\omega = \omega_p$, holding in the homogeneous frame. For the linear polarization we have to calculate averages explicitly

$$\langle np_\perp^2 \rangle = n\gamma \left(\langle \gamma \rangle - \gamma^2 \left\langle \frac{1}{\gamma} \right\rangle \right) = n\gamma^2 \frac{F(q)}{2F_1(q)} \tag{6.20}$$

$$\frac{\langle E^2 \rangle}{8\pi mc^2} = \frac{E_0^2 \langle y^2 \rangle}{8\pi mc^2} = \frac{4n\gamma^2}{q} \langle y^2 \rangle = n\gamma^2 \frac{F(q)}{2F_1(q)} = \langle np_\perp^2 \rangle \tag{6.21}$$

where

$$F(q) = 2F_1(q) \left(\frac{1}{\gamma} \langle \gamma \rangle - \gamma \left\langle \frac{1}{\gamma} \right\rangle \right) \tag{6.22}$$

For later use, we also define $G(q)$ as

$$G(q) = 2F_1(q) \left(\frac{1}{\gamma} \langle \gamma \rangle + \gamma \left\langle \frac{1}{\gamma} \right\rangle \right) \tag{6.23}$$

Another simplification will come from the continuity equation (6.11)

$$\frac{1}{R^2}\frac{d}{dR}\left[R^2\gamma_* \left(\beta_* n\gamma + p_\parallel \langle n \rangle \right) \right] = 0 \tag{6.24}$$

$$\frac{2}{R}\left(\beta_* n\gamma + p_\parallel \langle n \rangle \right) + \beta_*\gamma_*^2 \frac{d\beta_*}{dR}\left(\beta_* n\gamma + p_\parallel \langle n \rangle \right) + \frac{d}{dR}\left(\beta_* n\gamma + p_\parallel \langle n \rangle \right) = 0 \tag{6.25}$$

Cancelling those terms in (6.18) and noting that $\gamma_*(\gamma + \beta_* p_\parallel) = \gamma'$ we get

$$\frac{n\gamma}{\gamma_*}\frac{d\langle \gamma' \rangle}{dR} + \beta_*\gamma_*^2 \frac{d\beta_*}{dR}(n\gamma \langle \gamma \rangle - \gamma^2 \langle n \rangle) - \frac{1}{2}\gamma^2 \frac{d\langle n \rangle}{dR} + \frac{1}{2}\gamma \langle \gamma \rangle \frac{dn}{dR} - \frac{1}{2}n\gamma \frac{d\langle \gamma \rangle}{dR} + \frac{1}{2}n \langle \gamma \rangle \frac{d\gamma}{dR} = 0 \tag{6.26}$$

For the circular polarization $\langle n \rangle = n$, $\langle \gamma \rangle = \gamma$ so all the terms – apart from the first one – cancel and we get

$$\frac{d\gamma'}{dR} = 0 \tag{6.27}$$

For the linear polarization, expressing averages explicitly as integrals and using

$$\frac{1}{\gamma_*}\frac{d\gamma_*}{dR} = \beta_*\gamma_*^2\frac{d\beta_*}{dR} \ , \qquad \langle n\rangle = n\gamma\left\langle\frac{1}{\gamma}\right\rangle \tag{6.28}$$

we get

$$\frac{n\gamma}{\gamma_*}\frac{d\langle\gamma'\rangle}{dR} + \frac{\gamma^2}{2}\left[\frac{1}{\gamma_*}\frac{d\gamma_*}{dR}\frac{nF(q)}{F_1(q)} + \frac{1}{2}\frac{F(q)}{F_1(q)}\frac{dn}{dR} - \frac{n}{2}\frac{d}{dR}\left(\frac{G(q)}{F_1(q)}\right)\right] = 0 \tag{6.29}$$

Because ω' is a fixed pulsar rotation frequency, we use

$$\frac{n}{n'} = \frac{n}{\tilde{n}\gamma_*^2} = \frac{16}{\pi^2}\frac{F_1^2(q)}{q}\frac{1}{\gamma_*^2} \tag{6.30}$$

to get

$$\frac{n\gamma}{\gamma_*}\frac{d\langle\gamma'\rangle}{dR} + \frac{4}{\pi}\frac{n'}{\gamma_*^2}\left[\frac{F}{F_1}\frac{d}{dR}\left(\frac{F_1^2}{q}\right) - \frac{F_1^2}{q}\frac{d}{dR}\left(\frac{G}{F_1}\right)\right] = 0 \tag{6.31}$$

Expression in the bracket gives 0, so we are left with

$$\frac{d\langle\gamma'\rangle}{dR} = 0 \tag{6.32}$$

6.2.2 Matching of a circularly polarized wave

For the circularly polarized waves

$$\begin{aligned}\left\langle T'^{11}\right\rangle &= 2mc^2np_\parallel'^2 + \frac{1}{2}\frac{E'^2+B'^2}{4\pi}\\ &= 2mc^2np_\parallel'^2 + (1+\beta_*^2)\frac{E'^2}{8\pi}\end{aligned} \tag{6.33}$$

From (6.12)

$$\begin{aligned}p_\parallel' &= \gamma_*(\beta_*\gamma + p_\parallel)\\ &= \frac{\mu\gamma_*^2}{R^2}\end{aligned} \tag{6.34}$$

In the limit $R\to\infty$, $\beta_*\to 0$, so we get

$$p_{\rm ext} = \left\langle T'^{11}\right\rangle\Big|_\infty = \left.\frac{E^2}{8\pi}\right|_\infty = mc^2n'p_{\perp\infty}^2 \tag{6.35}$$

where $n' = m\omega'^2/(8\pi e^2)$ is the asymptotic value of $\tilde{n} = m\omega^2/(8\pi e^2) = m\omega'^2/(\gamma_*^2 8\pi e^2)$. Hence

$$p_{\perp\infty}^2 = \frac{p_{\rm ext}}{n'mc^2} \tag{6.36}$$

From (6.15) we get

$$\begin{aligned}\gamma'^2 &= 1 + p_{\parallel 0}'^2 + p_{\perp 0}^2\\ &= 1 + p_{\perp\infty}^2\end{aligned} \tag{6.37}$$

The algebraic equations that determine an electromagnetic wave at launch are: (6.13), (6.14), (6.34), (6.37). The roots can be found numerically, but to gain some intuition how the initial values depend on the MHD wind parameters, we can also approximate them analytically. From (6.37) and (6.34)

$$p_{\perp 0}^2 = p_{\perp\infty}^2 - \frac{\mu^2\gamma_{*0}^4}{R_0^4} \tag{6.38}$$

and from (6.14), (6.33)

$$p_{\perp 0}^2 = \frac{\left(\nu - \mu\frac{\gamma_{*0}^2}{R_0^2}\right) 2\mu\frac{\gamma_{*0}^2}{R_0^2}}{2\gamma_{*0}^2 - 1} \tag{6.39}$$

These two equations can be combined to give a quadratic equation for R_0^2 as a function of γ_{*0}. A solution we expand in a small parameter $1/\mu \sim 1/\nu$ and in the lowest order

$$R_0^2 \approx \frac{2\mu\nu\gamma_{*0}^2}{p_{\perp\infty}^2(2\gamma_{*0}^2 - 1)} \tag{6.40}$$

In analogy with this, from (6.13) we also get a quadratic equation for R_0^2, and after expanding

$$R_0^2 \approx \frac{\mu^2\gamma_{*0}}{p_{\perp\infty}^2\sqrt{\gamma_{*0}^2 - 1}} - \frac{\mu\gamma_{*0}\sqrt{1 + p_{\perp\infty}^2}}{p_{\perp\infty}^2\sqrt{\gamma_{*0}^2 - 1}} \tag{6.41}$$

$p_{\perp\infty}$ is given by (6.36). Combining (6.40) and (6.41), we finally obtain

$$\gamma_{*0}^2 \approx \frac{1}{2}\left(1 + \frac{\nu}{\sqrt{\nu^2 - (\mu - \gamma_0)^2}}\right), \qquad \gamma_0 = \sqrt{1 + p_{\perp\infty}^2} \tag{6.42}$$

$$R_0^2 \approx \frac{\mu}{p_{\perp\infty}^2}\left(\nu + \sqrt{\nu^2 - (\mu - \gamma_0)^2}\right) \tag{6.43}$$

6.2.3 Matching of a linearly polarized wave

For linearly polarized waves

$$\left\langle T'^{11}\right\rangle = 2mc^2\gamma_*^2\left\langle 2\beta_* n\gamma p_\parallel + \frac{E^2}{16\pi mc^2}(1 + \beta_*^2) + np_\parallel^2 + n\gamma^2\beta_*^2\right\rangle \tag{6.44}$$

$$= 2mc^2\gamma_*^2\left[2\beta_* n_0\gamma_0 p_{\parallel 0} + \frac{1}{2}n_0\gamma_0\left\langle\frac{p_\perp^2}{\gamma}\right\rangle(1 + \beta_*^2) + n_0\gamma_0 p_{\parallel 0}^2\left\langle\frac{1}{\gamma}\right\rangle + n_0\gamma_0\beta_*^2\left\langle\gamma\right\rangle\right] \tag{6.45}$$

where we used (6.21), (6.20) and (6.28) (see below). From (6.12)

$$\begin{aligned}\left\langle J'\right\rangle &= 2\gamma_* n_0\gamma_0\left(\beta_* + p_{\parallel 0}\left\langle\frac{1}{\gamma}\right\rangle\right)\\ &= 2\gamma_* n_0\gamma_0\left(\beta_* + \frac{p_{\parallel 0}}{\gamma_0}\frac{G(q) - F(q)}{4F_1(q)}\right)\\ &= \frac{2n_0\mu\gamma_*^2}{R^2}\end{aligned} \tag{6.46}$$

and in the limit $R \to \infty$, $\beta_* \to 0$ we get

$$n_0\gamma_0 p_{\parallel 0}\left\langle\frac{1}{\gamma}\right\rangle \to 0 \tag{6.47}$$

Hence, in this limit and we also get from (6.45)

$$p_{\text{ext}} = \left\langle T'^{11}\right\rangle\Big|_\infty = mc^2 n_0\gamma_0\left\langle\frac{p_\perp^2}{\gamma}\right\rangle\Big|_\infty \tag{6.48}$$

$$= mc^2 n_0\gamma_0^2\left(\frac{1}{\gamma_0}\left\langle\gamma\right\rangle - \gamma_0\left\langle\frac{1}{\gamma}\right\rangle\right)\Big|_\infty \tag{6.49}$$

$$= mc^2 n_0\gamma_0^2\frac{F(q)}{2F_1(q)}\Big|_\infty \tag{6.50}$$

where $F_1(q)$, $F(q)$ are given by (2.76) and (6.22), respectively. Taking into account (2.78) and limiting value $\gamma_0 \to 1$ as $R \to \infty$, we have the final form

$$\frac{8}{\pi^2}\frac{F(q)F_1(q)}{q}\bigg|_\infty = \frac{p_{\rm ext}}{mc^2 n'} \tag{6.51}$$

From this equation we calculate q_∞, which, in turn, allows to obtain $\langle\gamma'\rangle|_\infty$, and therefore the initial value $\langle\gamma'\rangle|_0$

$$\begin{aligned}\langle\gamma'\rangle\big|_\infty = \langle\gamma\rangle|_\infty &= \frac{F(q)+G(q)}{4F_1(q)}\bigg|_\infty \\ &= \langle\gamma'\rangle\big|_0 = \gamma_0\,\frac{F(q)+G(q)}{4F_1(q)}\bigg|_0\end{aligned} \tag{6.52}$$

The wave at launch is determined by (6.13), (6.14), (6.46), (6.52).

6.2.4 External pressure

Instead of $p_{\rm ext}$, one can define another parameter $r_{\rm ext}$, which characterizes the distance, at which $p_{\rm ext}$ is equal to the ram pressure $p_{\rm ram}$ of the MHD wind (i.e., the distance from a pulsar to the MHD-shock)

$$p_{\rm ram} = \frac{L}{4\pi r_{\rm ext}^2 c} = \frac{m^2c^2\omega'^2}{4\pi e^2}\frac{a_{\rm L}^2}{\rho_{\rm ext}^2} = \frac{m^2c^2\omega'^2}{4\pi e^2}\frac{\mu^2}{R_{\rm ext}^2} \tag{6.53}$$

$$= p_{\rm ext} \tag{6.54}$$

Asymptotically $p_{\rm ram} \to 0$. Thus, asymptotic, constant, but nonvanishing pressure of the EM wave is always higher than that of the MHD wind. The upper limit for this value $p_{\rm ext}^{\rm up}$ is determined by the critical radius $R_{\rm ext} = R_{\rm c} = 1$, i.e., $p_{\rm ext}^{\rm up} = m^2c^2\omega'^2\mu^2/4\pi e^2$. It corresponds to the wave that is launched almost at the cut-off. If the external pressure is higher than $p_{\rm ext}^{\rm up}$, the EM precursor cannot be formed because the required conversion radius would fall below the critical one. Hence, the larger is μ, the higher can be the external pressure for which the precursor still exist.

Rewriting the initial conditions (6.42), (6.43) for a circularly polarized mode in terms of $\rho_{\rm ext}$, we get

$$\gamma_0^2 = 1 + p_{\perp\infty}^2 = 1 + 2\frac{a_{\rm L}}{\rho_{\rm ext}} \tag{6.55}$$

$$\rho_0^2 \approx \frac{\rho_{\rm ext}^2}{2\mu}\left(\nu + \sqrt{\nu^2 - (\mu-\gamma_0)^2}\right) \tag{6.56}$$

This implies that the smaller the external pressure (or equivalently the larger $\rho_{\rm ext}$), the further from the pulsar the wave is launched, and the larger group speed, and the smaller amplitude it has. The amplitude is the largest, when the wave conversion occurs close to the cut-off.

Fig. 6.3 shows the example of matching for $a_{\rm L} = 3.4\times10^{10}$, $\mu = 10100$, $\sigma = 100$ and $\rho_{\rm ext} = 4.6\times10^7$; note that the distance $\rho_{\rm ext}$ is smaller than the radius of the termination shock in the Crab nebula $\rho_{\rm ts} \approx 10^9$.

6.3 EM precursors of pulsar wind shocks

Superluminal waves are known to be unstable. Small density perturbations propagating in the direction of motion become amplified and grow at extremely fast rates, of the order of the plasma frequency $\Gamma \sim \omega_p$ [141, 118]. When this happens, the wave is disrupted and its energy becomes thermalized. In our approach, a shock is a region, in which the instabilities set in

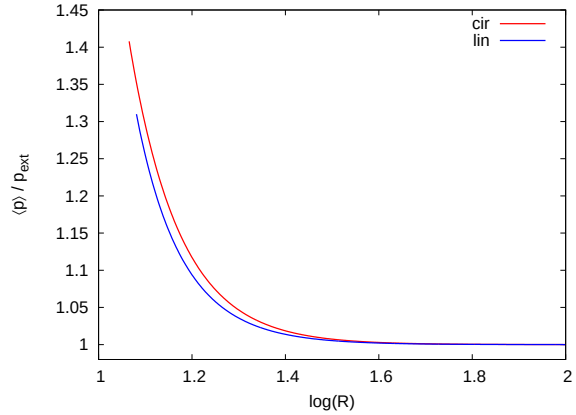

(a) pressure p

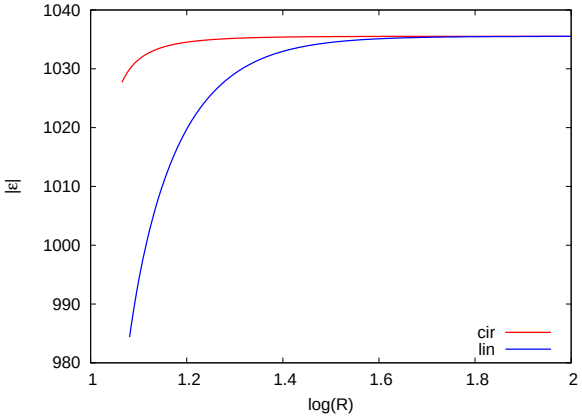

(b) magnitude of the normalized electric field $|\varepsilon| \equiv \left\langle (eE/mc\omega)^2 \right\rangle^{1/2} = a \left\langle y^2 \right\rangle^{1/2}$

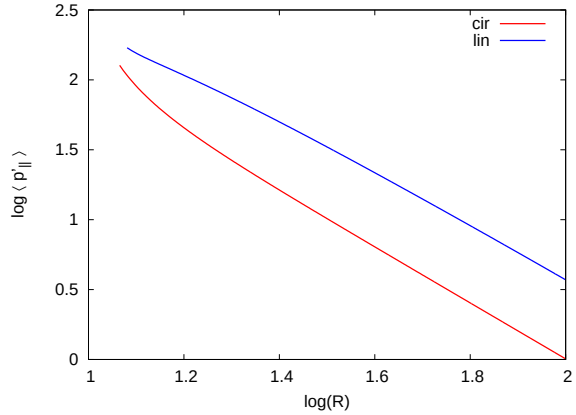

(c) parallel momentum in the lab frame $p'_{\parallel}$

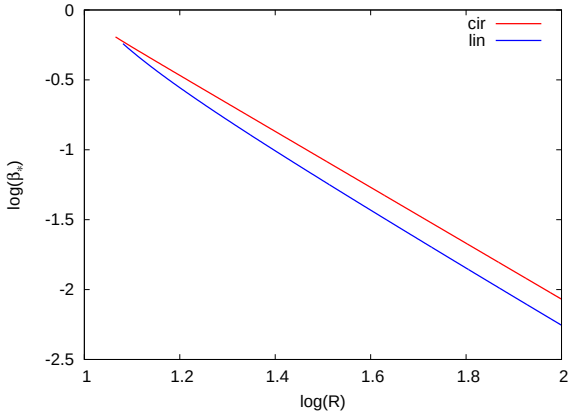

(d) wave group velocity β_*

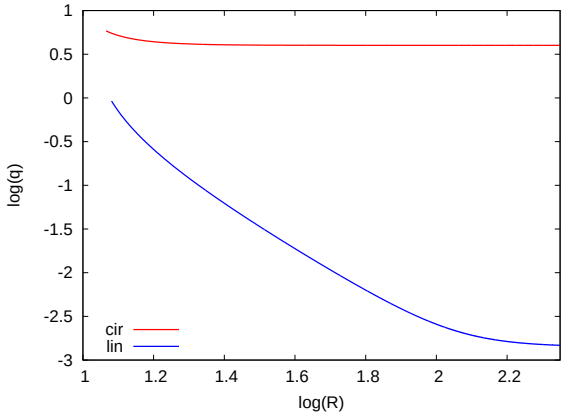

(e) nonlinearity parameter q

Figure 6.3: Radial evolution of a strong wave, whose pressure is matched asymptotically to the external pressure $p_{\rm ext}$. Exemplary values for the matching were chosen to be $a_{\rm L} = 3.4 \times 10^{10}$, $\mu = 10100$, $\sigma = 100$ and $\rho_{\rm ext} = 4.6 \times 10^7$ ($R_{\rm ext} = 13.8$).

and the total energy carried by the cold fluids and the Poynting flux is randomized. Based on calculations [118] and simulations [178, 184] in the literature, we expect the instabilities to set in when the particles stream through the wave sufficiently slowly, i.e., when the wave group speed becomes approximately equal to the parallel component of the particle velocity.

We have already showed that as a large-amplitude wave propagates, it slows down gradually due to the spherical sideways expansion. Here we examine its radiative damping, a consequence of the nonlinear inverse Compton process. This mechanism also makes the wave slow down, and, as a result, it leads to a decrease of the streaming. We expect, however, that it has the radiative signatures that differ from those of the standard MHD-shock.

6.3.1 Damping due to radiation reaction

Inhomogeneities introduced by the radiation reaction force acting on the particles are added as a first order correction to the plane-wave solution, in analogy with the analysis of the spherical effects. We assume that the damping in one wavelength is small, thus the small parameter $\epsilon = r_0/r_{\rm L} = (e^2/mc^2 r_{\rm L}) < c/r\omega \ll 1$, where r_0 is the classical radius of an electron. As a fast variable we again choose the WKB-like phase (6.1), and a slow distance is $\rho = \epsilon r/r_{\rm L}$. Writing the radiation reaction force density in a way discussed in §2.3.1, we have

$$f'^{\mu} = -\frac{2}{3}\frac{m^2c^3}{\hbar} n_0 \alpha_{\rm f} \eta^2(\gamma', p'_{\parallel}, p'_{\perp}) \tag{6.57}$$

where

$$\eta = \frac{1}{E_{\rm cr}}\sqrt{(p_\mu F^{\mu\nu})^2} = \frac{e\hbar}{m^2c^3}\Delta'|E'| \tag{6.58}$$

From (6.9) and (6.10), we find the equations

$$\frac{1}{R^2}\frac{d}{dR}\left[R^2\left(n_0 mc^2 p'_{\parallel}\gamma' + \frac{\beta_* E'^2}{8\pi}\right)\right] = \frac{c}{\omega'}\frac{a_{\rm L}}{\mu} f^0 \tag{6.59}$$

$$\frac{1}{R^2}\frac{d}{dR}\left[R^2\left(n_0 mc^2 p'^2_{\parallel} + \frac{1}{2}(1+\beta_*^2)\frac{E'^2}{8\pi}\right)\right] = n_0 mc^2 \frac{p_\perp^2}{R} + \frac{c}{\omega'}\frac{a_{\rm L}}{\mu} f^1 \tag{6.60}$$

where we rescaled the radial coordinate according to (5.42). Using $E' = \gamma_* E$ and (6.19), we get

$$\frac{1}{R^2}\frac{d}{dR}\left[R^2\left(\frac{p'_{\parallel}\gamma'}{\gamma_*^2} + \beta_* p_\perp^2\right)\right] = -g\frac{a_{\rm L}}{\mu}\frac{p_\perp^2 \Delta'^2 \gamma'}{\gamma_*^2} \tag{6.61}$$

$$\frac{1}{R^2}\frac{d}{dR}\left[R^2\left(\frac{p'^2_{\parallel}}{\gamma_*^2} + \frac{1}{2}(1+\beta_*^2)p_\perp^2\right)\right] = \frac{1}{\gamma_*^2}\frac{p_\perp^2}{R} - g\frac{a_{\rm L}}{\mu}\frac{p_\perp^2 \Delta'^2 p'_{\parallel}}{\gamma_*^2} \tag{6.62}$$

where

$$g = \frac{2}{3}\alpha_{\rm f}\frac{\hbar\omega'}{mc^2} \tag{6.63}$$

Here we consider only a circularly polarized wave so we omit phase averaging. The results of numerical integration of equations (6.61) and (6.62) for exemplary values of the parameters are shown in Fig. 6.4. It can be noticed that as the particles radiate, the energy is lost from the system overall; however, the particles gain from the wave fields more energy than they lose in radiation, and, consequently, they accelerate (Fig. 6.4b, $p_\perp \approx \gamma$ increases), whereas the wave slows down (Fig. 6.4d, β_* drops). The physical reason is the dephasing of $p_\perp$ and $\boldsymbol{E}$, induced by the presence of radiation drag. In a circularly polarized wave $p_\perp$ is everywhere orthogonal to the wave electric field provided no interaction with photons is present, but as soon as the radiation drag appears, $p_\perp$ starts lagging behind $\boldsymbol{E}$; the momentum and electric vectors are not orthogonal any more, which results in the particle acceleration at the expense of the wave energy. Moreover, also a Lorentz force is induced in the direction of the wave propagation. At the end of the day, the group velocity of the wave drops and the particles catch up with the wave. In the comoving frame both the particle and electromagnetic fluxes vanish at this point, so that it

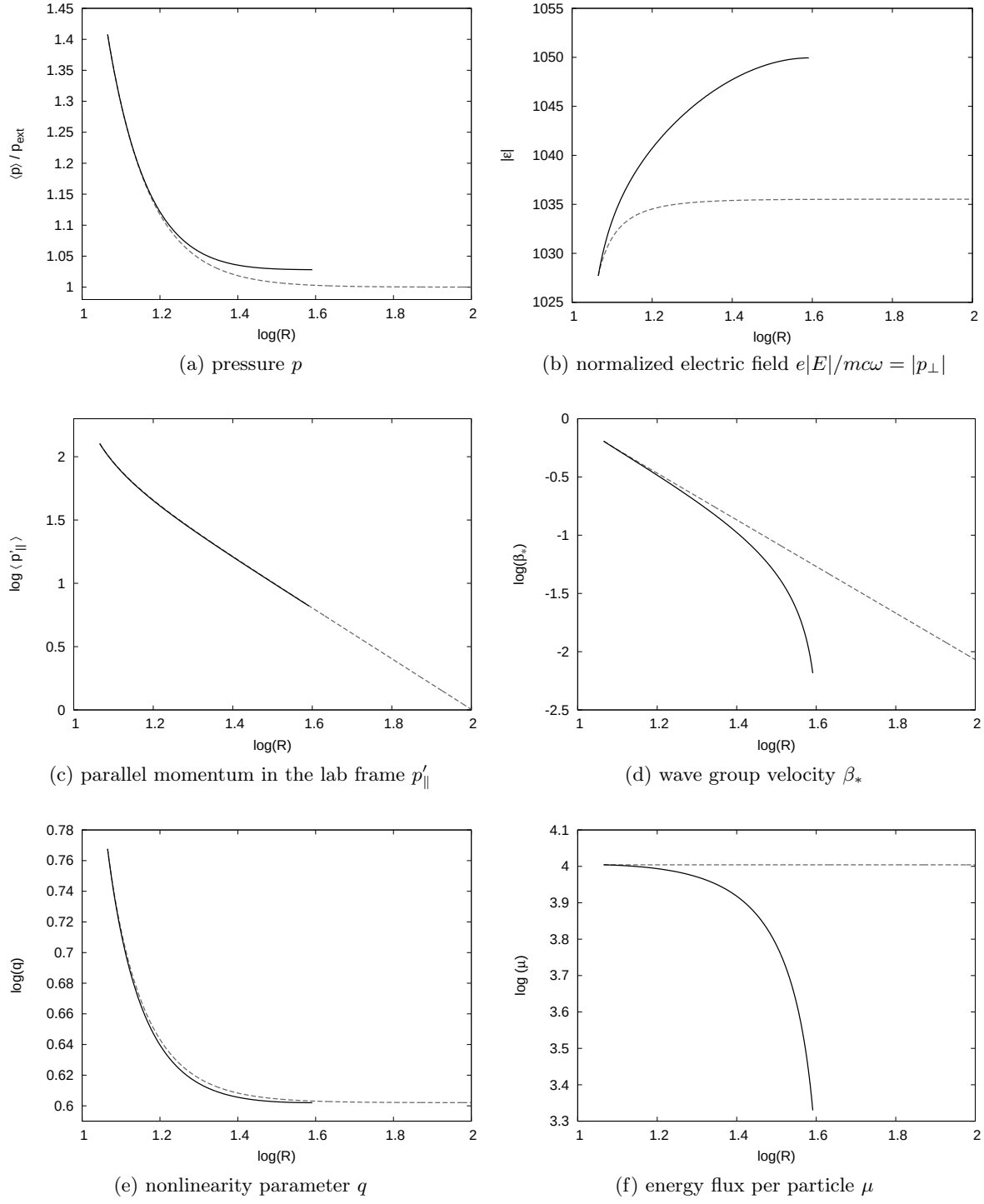

(a) pressure p

(b) normalized electric field $e|E|/mc\omega = |p_\perp|$

(c) parallel momentum in the lab frame $p'_\parallel$

(d) wave group velocity β_*

(e) nonlinearity parameter q

(f) energy flux per particle μ

Figure 6.4: Radial evolution of a circularly polarized strong wave undergoing strong radiation damping (solid lines). Dashed lines denote the solution without the radiation reaction. The integration is stopped at the point, where the particle streaming through the wave vanishes (i.e., where $\beta_* = p'_\parallel/\gamma'$). Exemplary values for the matching were taken to be $a_\mathrm{L} = 3.4 \times 10^{10}$, $\mu = 10100$, $\sigma = 100$, $\rho_\mathrm{ext} = 4.6 \times 10^7$ ($R_\mathrm{ext} = 13.8$), $g = 10^{-18}$.

can be regarded as a boundary (shock), where, due to the vanishing streaming, the instabilities in the outflow come into play.

The important remark is that in the no-streaming point the energy is equipartitioned between the particles and the fields. Since the wave in this point, $\gamma_* \approx 1$, and the particle energy flux is approximately $p'_\parallel \gamma'$. On the other hand, the Poynting flux is given by $p'_\parallel p_\perp^2/\gamma' \approx p'_\parallel \gamma'$, since $\beta_* = p'_\parallel/\gamma'$ and $p_\perp \approx \gamma'$. Thus, the final total energy flux is given by

$$\mu_{\rm f} \approx 2\frac{R^2 p_\perp^2 \beta_*}{\mu} \tag{6.64}$$

Since the parallel component of the particle velocity is equal to the wave speed, the relation

$$\frac{p'_\parallel}{\beta_*} = \gamma' \approx \frac{R^2 p_\perp^2 \beta_*}{\mu} \tag{6.65}$$

holds. These two equations can be combined to give

$$\mu_{\rm f} = 2p_{\perp\infty}\gamma_* \approx 2p_{\perp\infty} \tag{6.66}$$

Equation 6.66 shows that the energy flux that is left in the outflow does not depend on the initial energy flux μ. Hence, for a given $p_{\rm ext}$, the more energy is available, the more is also dissipated into the radiation field before the no-streaming point is reached. On the other hand, the higher the external pressure $p_{\rm ext}$, the larger is the wave amplitude, and the more important radiation drag becomes. In this case, however, the wave abruptly slows down, transferring energy to the accelerated particles, but the total energy is not efficiently dissipated by the system. Thus, in the strong radiation reaction regime, the conversion between the electromagnetic and kinetic energy occurs without significant energy losses, but the wave becomes unstable, and forms a shock quickly after the launch.

We can estimate the damping lengthscale $R_{\rm d}$ analytically. From (6.61), by integrating both sides over R,

$$\mu - \mu_{\rm f} = \frac{g a_{\rm L}}{\mu^2}\int_{R_0}^{R_{\rm d}} dR\, R^2\, p_\perp^2\, \Delta'^2 \gamma' \tag{6.67}$$

and approximating $p_\perp \approx p_{\perp\infty}$, $\Delta' \approx \gamma' \approx p_{\perp\infty}$, one obtains

$$R_{\rm d} \approx \left(R_0^3 + \frac{3\mu^2(\mu-\mu_{\rm f})}{g a_{\rm L}\, p_{\perp\infty}^5}\right)^{1/3} \tag{6.68}$$

$$= \left[R_0^3 + \frac{3R_{\rm ext}^5}{2^{5/2} g a_{\rm L}\mu^2}\left(1 - \frac{2\sqrt{2}}{R_{\rm ext}}\right)\right]^{1/3} \tag{6.69}$$

where R_0 and $p_{\perp\infty}$ are given by (6.43) and (6.36), respectively. In Fig. 6.5 we show the damping length as a function of $R_{\rm ext}$. We plot both the numerical results and the analytic estimation (6.69). The latter is valid only when $R_{\rm ext} \geq 2\sqrt{2}$, and it is a good approximation only when the external pressure is rather low.

Rewriting the damping length in wavelengths, we get

$$\rho_{\rm d} \approx \left[\rho_0^3 + \frac{3a_{\rm L}^2}{g p_{\perp\infty}^5}\left(1 - \frac{\mu_{\rm f}}{\mu}\right)\right]^{1/3} \tag{6.70}$$

It shows that $\rho_{\rm d}$ is only very weakly dependent on the initial mass loading μ, but it strongly depends on the external pressure – the higher $p_{\rm ext}$ is, the smaller the damping lengthscale becomes.

Since the shock location is given by the damping length in the radiation dominated regime, our results imply that in the pulsar systems one can distinguish between different scenarios of the formation of the termination shocks. For specified values of the magnetospheric and wind

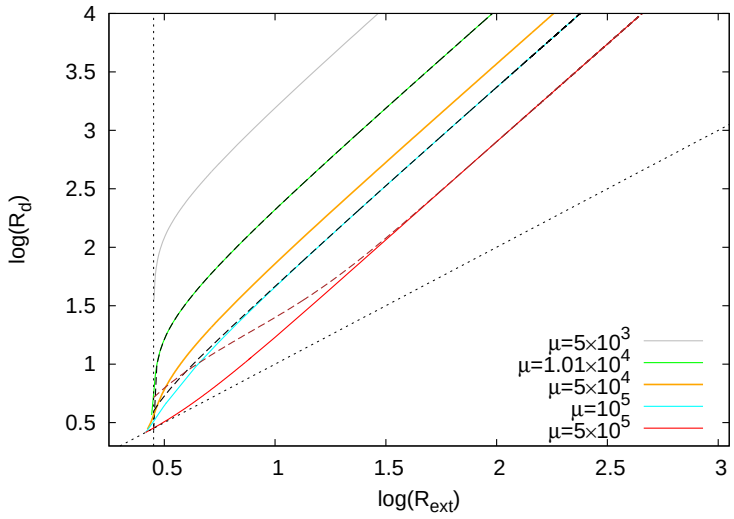

Figure 6.5: Damping length $R_{\rm d}$ of a strong wave as a function of the external pressure, characterized by the distance $R_{\rm ext}$ at which it would balance the ram pressure of an MHD wind. Solid curves show the numerical results (where R_d is taken as a point of vanishing streaming). Dashed curves show the analytical estimate (6.69) for three different values of μ. Clearly, the analytical approximation is not valid when the external pressure is high (i.e., $R_{\rm ext}$ is low) and the mass loading μ is large. Below the minimum value $R_{\rm ext} = 2\sqrt{2}$, denoted here by the vertical line, the analytical approximation is not valid. Parameters are chosen as those of the Crab: $a_{\rm L} = 3.4 \times 10^{10}$, $\sigma = 100$, $g = 1.19 \times 10^{-21}$.

parameters, the structure of the shock is determined only by the pressure conditions in the external medium:

(1) if the external pressure is very high $p_{\rm ext} > p_{\rm ram}(R_{\rm c})$, so that the conversion radius required by the external conditions falls below the critical radius, the superluminal mode cannot be launched and the shock is formed when the inner, MHD striped wind interacts with the surroundings,

(2) if the pressure is $p_{\rm ext} < p_{\rm ram}(R_{\rm c})$, the EM precursor can be launched; here, however, different cases may also occur:

- when the pressure is close to the maximal value, the radiation damping is efficient; in addition, if the mass loading μ is large enough to support the superluminal wave solution, the damping determines the shock location (this damping is followed by the instabilities in the outflow),
- the pressure is lower so that the radiation damping in the wave is ineffective; in this case the particle streaming decreases, e.g., due to the spherical expansion, until the instabilities set in and the shock is formed.

6.3.2 Application to binaries

For the Crab nebula the pressure at the termination shock of the pulsar wind was estimated by Kennel and Coroniti [90]. In their MHD model of a pulsar wind/nebula system, behind the shock it is given by $\sim L/(4\pi r_{\rm s}^2 c)$ and it falls with the distance, with the radial dependence determined by the value of σ. It was found that for small magnetization, close to the inner edge of the nebula, the pressure is approximately $\sim 10^{-8}$ dyn cm^{-2}. Following this analysis, we assume this value at the shock. In fact, it is very low, hence the effects of radiation reaction are negligible. In Fig. 6.5 it is shown how the damping lengthscale depends on $R_{\rm ext}$. For Crab $\rho_{\rm ext} \approx 10^9$, and dissipation is very inefficient for any reasonable value of μ. Estimating the dissipation length from (6.70),

one obtains a value much larger than the distance to the termination shock $\rho_{\rm d} \sim 2\times10^{11} \gg \rho_{\rm ext}$.

A different situation arises for the binaries, in which the wind of a massive companion star provides a high-pressure environment. If this pressure is sufficiently large, and also the mass loading is large, the EM wave can form a shock close to where it would be expected from the MHD wind. In Fig. 6.5 the red curve shows these solutions, for which $R_{\rm d} \approx R_{\rm ext}$ when the pressure is high. Such a non-MHD shock, characterized by its precursor, even though located close to the would-be MHD shock of the striped wind, has very different structure and properties, when compared to the standard MHD shocks: (1) upstream in the flow the electromagnetic energy is effectively transferred to the particles, (2) possibility it can be created only in some parts of the pulsar orbit, (3) it has radiative signatures that depend mostly on the external pressure.

To study these properties as an example we consider the binary system PSR B1259-63. The 48 ms pulsar moves around the massive companion Be-type star on a very eccentric orbit with a period 3.4 years [88]. The pulsar spin-down power was measured to be $L = 8\times10^{35}$ erg s^{-1} which gives

$$a_{\rm L} = 3.8\times10^{9} \tag{6.71}$$

From (6.63) one can also calculate the radiation damping coefficient as

$$g = 8.2\times10^{-22} \tag{6.72}$$

Most probably, there is no accretion onto the pulsar [192], hence μ should be dependent only on the magnetospheric conditions, staying constant along the orbit. The distance from the star to the shock $r_{\rm sh}$, and also $p_{\rm ext}$ (the pressure at the shock between the pulsar and stellar winds), in contrast to μ, are both expected to change with the pulsar position relative to the star. However, $p_{\rm ext}$, determined by the stellar wind, is not well constrained, and strongly depends on a model of the stellar wind. Typically, for Be-type stars, such a wind is modelled as two-component, with a fast, low-density outflow from the polar regions and a slow, high-density one from the equatorial disk [206]. Since the disk-like equatorial flow does not extend to large distances, only the polar flow is thought to be important for shocks located further from the star than the disc edge $r_{\rm sh} \geq 1.6\times10^{13}$ cm. The mass loss rate is of the order $\dot{M} \approx 10^{-8}{\rm M}_\odot$ yr^{-1} and the velocity of a radiatively driven polar wind is modelled as [206] (for discussion see also [192])

$$v_{\rm w}(r) = v_\infty\left(1-\frac{r_*}{r}\right) \tag{6.73}$$

with $v_\infty = 2\times10^{8}$ cm s^{-1}, $r_* = 8\times10^{11}$ cm – the asymptotic wind velocity and a stellar radius, respectively. Pressure at the shock is given by

$$p_{\rm ext} = \frac{\dot{M}v_{\rm w}(r_{\rm sh})}{4\pi r_{\rm sh}^2} \tag{6.74}$$

For estimation we can safely approximate $v_{\rm w} \approx v_\infty$ for $r_{\rm sh} \gg r_*$. Assuming that the shock is located halfway between the star and the pulsar, when a pulsar is in the apastron, we get a value of the order 2×10^{-3} dyn cm^{-2}.

In the periastron, the external pressure may be rather determined by a dense equatorial flow. In this case the mass loss rate is higher, of the order $\dot{M} \approx 10^{-7}{\rm M}_\odot$ yr^{-1} and the velocity and density distributions are modelled as [205]

$$v(r) = v_0\left(\frac{r}{r_*}\right)^{n-2}, \qquad \rho(r) = \rho_0\left(\frac{r}{r_*}\right)^{-n} \tag{6.75}$$

with $\rho_0 = \dot{M}/4\pi r_*^2 v_0$ g cm^{-3}, $v_0 = 10^{6}$ cm s^{-1} and $2 \leq n \leq 4$, depending on the star. The value $n = 2.4$ is indicated for some Be stars [205]. The pressure, given by

$$p(r_{\rm sh}) = \frac{\dot{M}v_0}{4\pi r_*^2}\left(\frac{r_{\rm sh}}{r_*}\right)^{n-4} \tag{6.76}$$

strongly depends on the assumed parameters, ranging between $0.05 - 0.5$ dyn cm^{-2}.

In a system PSR B1259-63, however, the stellar disk is highly inclined to the plane of the pulsar orbit and even in the periastron this is rather the polar flow that determines the external pressure. The disk is probably important only when the pulsar crosses it, twice on the orbit. In the following we assume that the stellar flow is polar, and the pressure at the shock varies along the orbit only due to change of the orbital separation. In particular, one can notice that close to the periastron, the external pressure may be too high to allow the EM waves to be launched. In the apastron, on the other hand, propagation of a shock precursor can be permitted. Thus, a possiblity arises that depending on the orbital distance to the companion star, different regimes of the pulsar wind shock formation are probed. Here our strategy will be to choose μ which can

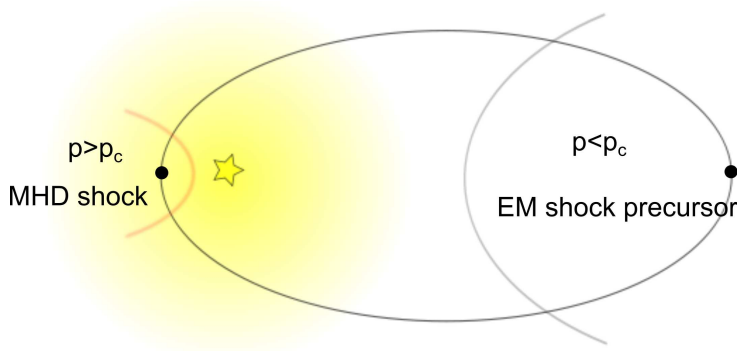

Figure 6.6: Sketch of the binary PSR B1259-63. Since the pulsar (black dot) is on a very eccentric orbit around the companion Be-star (yellow star), the external conditions provided by the stellar wind (yellow shading) change significantly over the period. Close to the periastron the pressure at the shock front (red curve) between the stellar and pulsar winds is higher than the critical value $p > p_c$, and the EM precursor cannot be launched. The shock is determined by the interaction of the stellar wind with the MHD striped wind. When the orbital separation increases, so that $p < p_c$, launching of a precursor becomes possible and non-MHD shock is formed.

support EM waves, matching even the highest estimated pressures. This case implies a testable prediction how the radiation losses $\mu_{\rm rad} = \mu - \mu_{\rm f}$ change during the orbital motion, if the shock is everywhere determined by the radiation reaction.

We examine the binary properties versus the orbital separation in several steps: (1) having chosen the MHD wind parameters, we calculate the EM wave parameters and integrate the evolution equations to obtain the wave dissipation length (i.e., the point where the streaming vanishes), which is smaller than the orbital separation. (2) In this point we calculate the pulsar wind pressure, which is assumed to be equal to the stellar wind pressure, given by

$$p_{\rm Be} = \frac{\Upsilon}{4\pi r_{\rm sh}^2} \tag{6.77}$$

where the outflow parameter $\Upsilon = \dot{M}_{-8} v_8$ [193, 192]. (3) Finally, we calculate the orbital separation by adding a shock distance from the pulsar (conversion radius + dissipation length) and a shock distance from the star (calculated from Eq. 6.77). Fig. 6.7 shows the resulting radiated energy per particle $\mu_{\rm rad}$, pressure at the shock $p_{\rm sh}$ and the dissipation length $r_{\rm d}$ versus the orbital distance d.

Very high energy emission in PSR B1259-63 is attributed to the inverse Compton scattering of soft stellar photons by energetic particles in the pulsar wind [98, 18]. The drag due to IC scattering can be treated in the same manner as the radiation reaction, and in the first order

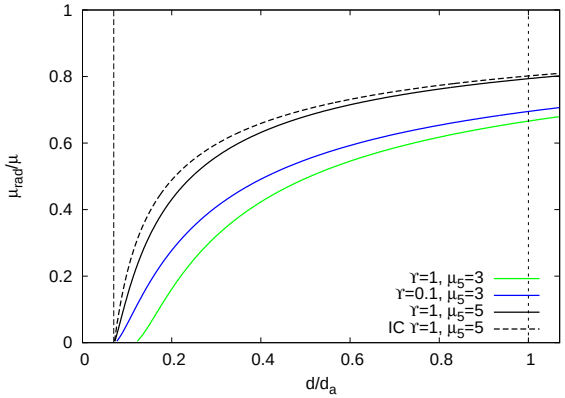

(a) radiated energy per particle

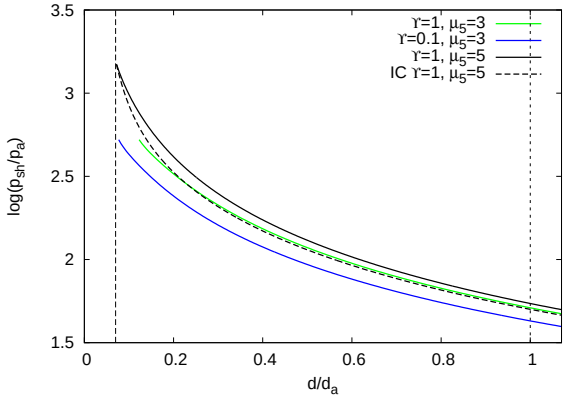

(b) pressure at the shock

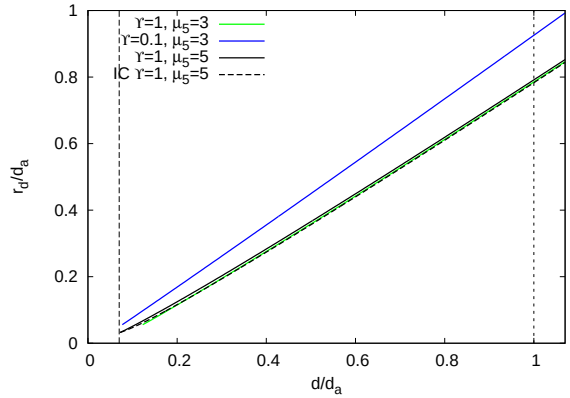

(c) distance from the pulsar to the shock

Figure 6.7: The radiated energy per particle $\mu_{\rm rad}$, the star wind pressure at the shock $p_{\rm sh}$ and the shock distance from the pulsar $r_{\rm d}$ (i.e., the damping length $r_{\rm d} = \rho_{\rm d} r_{\rm L}$) versus the orbital separation d. Distances are normalized to the orbital separation at the apastron $d_{\rm a} = 1.4 \times 10^{14}$ cm. The pressure is normalized to $p_{\rm a} \equiv L_{\rm sd}/4\pi c d_{\rm a}^2 = 1.08 \times 10^{-4}$ dyn cm^{-2} ($L_{\rm sd}$ is a pulsar spin-down luminosity). Vertical lines denote the apastron and periastron separation for this system. The dashed line is the result obtained when the IC energy losses are taken into account. $\mu = \mu_5 \times 10^5$, Υ denotes a model of the companion star's wind (the bigger the value, the denser the wind). We assumed $a_{\rm L} = 3.8 \times 10^9$, $\sigma = 100$ and $g = 8.2 \times 10^{-22}$.

one obtains the radial evolution of the total energy and momentum

$$\frac{1}{R^2}\frac{d}{dR}\left[R^2\left(\frac{p'_\parallel \gamma'}{\gamma_*^2} + \beta_* p_\perp^2\right)\right] = -\frac{4}{3}\frac{\sigma U}{mc^2}\frac{a_{\rm L} c}{\mu\omega'}\frac{\gamma'(\gamma'^2-1)}{\gamma_*^2} \tag{6.78}$$

$$\frac{1}{R^2}\frac{d}{dR}\left[R^2\left(\frac{p'^2_\parallel}{\gamma_*^2} + \frac{1}{2}(1+\beta_*^2)p_\perp^2\right)\right] = \frac{1}{\gamma_*^2}\frac{p_\perp^2}{R} - \frac{4}{3}\frac{\sigma U}{mc^2}\frac{a_{\rm L} c}{\mu\omega'}\frac{\gamma'^2 p'_\parallel}{\gamma_*^2} \tag{6.79}$$

The energy density in the photon field from the companion star of luminosity $L_* = 3.3 \times 10^{37}$ erg s^{-1} can be estimated as

$$U = \frac{L_*}{4\pi c d^2} \approx 0.9\left(\frac{d_{\rm p}}{d}\right)^2 \text{erg cm}^{-3} \tag{6.80}$$

where $d_{\rm p}$ is the orbital distance in the periastron. We can define the coefficient of the IC process

as

$$k = \frac{4}{3}\frac{\sigma U}{mc^2}\frac{a_{\rm L}c}{\omega'} = k_{\rm p}\left(\frac{d_{\rm p}}{d}\right)^2 \tag{6.81}$$

To estimate the IC effect, we work in the Thomson regime. Lorentz factors of the particles are the largest in the periastron, e.g., for $p_{\rm sh} \sim 0.1$ dyn cm^{-2}, $\gamma \sim 2\times10^5$. For the stellar temperature $T = 2.3\times10^4$ K, most photons appear with the energy $\epsilon = 2.7k_{\rm B}T/mc^2 \approx 10^{-5}$. Hence we get $\gamma\epsilon \sim 1$, which in fact is the threshold for the Klein-Nishina effects to become important. At larger distances, however, γ is lower and the Thomson limit safer. We can treat the calculation as the upper limit on the interaction.

Now we add both the radiation reaction and the IC drag forces on the flow and we calculate the shock position in analogy with the previous analysis, assuming that it is located at the point where the streaming in the flow vanishes. However, the photon energy density at the point, where the wave is launched, depends on the distance from this point to the star, which we do not know until we match the stellar and the pulsar wind pressures at the shock. To do it consistently we (i) choose k, (ii) integrate evolution equations, (iii) check if the location of the shock, and the flow pressure at the shock, satisfy the equation

$$d_{\rm p}\sqrt{\frac{k_{\rm p}}{k}} = r_{\rm d} - r_0 + \sqrt{\frac{\dot{M}v_{\rm w}}{4\pi p_{\rm sh}}} \tag{6.82}$$

where $r_{\rm d}$ is the distance from the the pulsar to the shock (i.e., the dissipation length), r_0 is the launching radius measured from the pulsar, (iv) if not, we repeat the procedure until we find a solution. The result is shown in Fig. 6.7.

Inverse Compton losses are the strongest not in the periastron but when the orbital separation is slightly larger $\sim (0.1-0.3)d_{\rm a} \sim (1.4-4.2)\times10^{13}$ cm. The shift of the radiation peak reflects the significance of the nonlinear inverse Compton (NIC) process in comparison to the external IC, similar as it is for the synchrotron/IC model discussed by Kirk et al. [98]. In a very highest pressure environment the former is dominant and very quickly leads to the wave slow-down and to the formation of the shock, without significant radiative losses from the precursor. Contribution from the scattering on the external photon field plays a role at larger orbital separations, when the photon energy density is still large, but the NIC process is less efficient. This effect can be even stronger when the full Klein-Nishina description is applied.

6.3.3 Implications for lightcurves

As the external pressure increases, the amount of the energy radiated in the precursor decreases (if μ is constant along the orbit). Since less energy is radiated, near the periastron the dissipation has to occur mainly at the shock itself, where the particles are accelerated, and therefore emit nonthermal radiation. Thus, in the parts of the orbit where the pressure is higher than in the other parts, but not too high so that the precursor still can be launched, one can expect an enhancement of the high energy emission from the shock.

In our model the emission is not only from the shock itself, where the flow is thermalized, but also from the shock precursor, as soon as it is launched. Since the radiation process is the NIC scattering in a strong wave, the spectrum will resemble that of the synchrotron photons. However, there is an additional effect that should be taken into account when modelling the emission. As the external pressure increases from apastron to periastron, photons radiated in the NIC process have higher energies. From Fig. 6.7 one can estimate the pressure at the shock in the apastron $\sim 10\,p_{\rm a}$ and the critical frequency of the radiated photons is $\Omega \approx \gamma^3\omega \approx 4\times10^{15}$ Hz. In the periastron it is higher, since $p \sim 700\,p_{\rm a}$ implies $\Omega \approx 10^{18}$ Hz. Thus, during the apastron passage one can expect a spatially extended optical/UV emission, which however may be masked by the emission from the luminous Be-star. Around the periastron the X-ray emission would

appear, but since the amount of the energy radiated by the precursor is suppressed in periastron (i.e., $\mu_{\rm rad} = \mu - \mu_{\rm f}$ has a minimum, because $\mu_{\rm f}$ has a maximum), it may be of lower intensity. the emission region would be rather compact, since the precursor layer between the wave launch and the shock is very thin. This emission in principle would be pulsed, but, on the other hand, may be smeared out during propagation.

In the periastron soft stellar photons can be upscattered in the IC process to energies $\gamma^2\epsilon \sim$ 100 GeV, and those emitted in the NIC process are in the X-ray band. If μ is smaller, say $\mu \sim 10^4$, the upscattered photons have energies of a few hundred MeV. Fermi data in > 100 MeV range in PSR B1259-63 show the flare emission 30-50 days after the periastron passage, see e.g. [191], and also after the stellar disk crossing. The flare is initiated quickly, with maximum 35 days after the periastron passage, but it drops very slowly afterwards. The flare emission is a significant fraction of the pulsar spindown power (the gamma-ray flare was not accompanied by any significant X-ray activity). Khangulyan et al. [95] proposed that the underlying process is Comptonization of the cold pulsar wind. When the pulsar crosses the stellar disk, its wind is early terminated, which suppresses the gamma-ray emission. After escape out of the disk, the pulsar wind increases its zone length towards the observer and the cooling length of the IC emission can be smaller than this zone length provided the sufficient photon density is present. In their model an additional source of the soft photons is needed, and it is the stellar disk itself. In our scenario the flare could be caused in the transition between the MHD and the non-MHD regime of the shock formation. 30 day after the periastron, during the flare, the binary members are $d \approx 3 \times 10^{13}$ cm apart – if this distance was equal to the critical radius $r_{\rm c}$, beyond which the EM wave precursor starts playing a role in determining the shock, it would give us $\mu = 2 \times 10^4$. This is consistent with no X-ray counterpart of the flare, because the precursor emission would be at $\Omega \sim 10^{15}$ Hz, the optical frequency where the starlight from the companion is much more luminous. This value of the mass loading implies multiplicities $\kappa \sim 10^5$, about order of magnitude smaller than that of the Crab.

In particular, this system can be compared to other binaries, like LS 5039 and LS I+61°303, which possibly also contain a young pulsar as a compact object [56]. In that case their mass loading μ may be similar in all three systems. The difference is that the two latter ones are more compact that PRS B1259-63:

	orbital separation [AU]	
system	periastron	apastron
PSR B1259-63	0.7	10
LS I+61°303	0.2	0.7
LS 5039	0.1	0.2

In our earlier calculations we assumed very high value of $\mu \sim$ few $\times 10^5$ that would allow the damping-dominated regime along the entire elongated orbit of PSR B1259-63. For this value we expect that LS 5039 is not able to support an EM precursor anywhere along he orbit, LS I+61°303 may be able to support it only close to the apastron, and PSR B1259-63 may have a non-MHD shock everywhere along the orbit. However, if μ is smaller, $\mu \approx 10^4$, an alternative possibility can be realized: in the apastron of LS I+61°303 the pressure is also too high, and only PSR B1259-63 can maintain the non-MHD shock around the apastron. More detailed analysis of lightcurves may help to distinguish between these scenarios.

6.3.4 Parametric instabilities

In our scenario, a flow is terminated when intrinsic instabilities set in. This can occur when the wave slows down due to radiation reaction or spherical expansion, and its group velocity $c\beta_*$ becomes close to the parallel component of particle velocity $v_\parallel$. As the wave slows down, in

the frame moving with $v_\parallel$ the wave frequency decreases until it reaches the plasma frequency. If large-amplitude waves are unstable against small perturbations, the parametric excitation of plasma oscillations can occur.

On the other hand, the discussed self-consistent waves are obtained as special solutions, in which particles and fields have a precisely set phasing. One may expect, therefore, that any perturbation of this equilibrium will destroy it [118]. Thus, the strong waves are likely to be unstable against small fluctuations. The stability analysis is crucial for an understanding of the formation of shocks, and is summarized in the next section.

Physical mechanism

The physics of parametric instabilities was explained first by Max [141]. A longitudinal wave, propagating through a nonlinear wave, produces the density perturbation δN that generates the perpendicular current $e\boldsymbol{v}_\perp \delta N$. This current is a source of a first order electromagnetic field (i.e., scattered electromagnetic mode), which, in turn, interferes with the field of the pump wave. Consequently, the ponderomotive force $\nabla(\boldsymbol{E} \cdot \delta\boldsymbol{E})$ is generated in the direction of the wave motion, and it reinforces the initial density perturbation. Thus, the feedback mechanism is a result of the coupling between transverse electromagnetic modes and longitudinal plasma oscillations, which occurs in the presence of a nonlinear wave in a plasma.

The parametric character of the instability can be understood most easily in the nonrelativistic limit, when a pump is a linear electromagnetic wave that causes electrons to oscillate with small amplitudes. In that case one linearizes the continuity equation and the equation of particle motion for small density and velocity perturbations. They can be combined to give an equation governing evolution of the density fluctuation. It has exactly the form of the Mathieu equation, describing parametrically driven oscillators [114, 113].

Wave stability

The stability of large-amplitude nonlinear waves against density perturbations, propagating in the direction of motion, was investigated in many papers. Max [141] studied transverse, circularly polarized waves in a cold unmagnetized electron-ion plasma, but the ions were treated nonrelativistically. The obtained dispersion relation was an eighth order polynomial in the perturbation frequency. Romeiras [178] extended this work by treating the ion motion relativistically, which also allowed him to discuss the wave stability in an electron-positron plasma. In this case, the dispersion relation decouples into a stable longitudinal second order branch, and a sixth order polynomial, describing transverse modes. When the streaming vanishes, these modes were shown to be unstable for every wave number in the limit of large phase velocities. The instability growth rate is as large as the wave frequency. Numerical calculations show, however, that the relativistic streaming can stabilize a wave. Analytical estimates were carried out by Lee & Lerche [118]. They found that, in a general case, the wave is unstable against short wavelength perturbations. However, the small-wavelength fluctuations are expected to be Landau-damped. Instead, long wavelength perturbations can play a role. In this case, Lee & Lerche found that the roots of the dispersion relation give an oscillatory behavior if

$$p_\parallel^2 > 2\gamma p_\perp - p_\perp^2 \tag{6.83}$$

i.e., when the streaming of the particles through the wave is sufficiently large. The wave stabilization by streaming was also shown in the PIC simulations [184]. This study showed that the launching of a circularly polarized wave into a relativistically streaming, cold pair plasma, permits its propagation without the disruption by instabilities, up to the shock, set up in simulations at a fixed position. The dissipation of the Poynting flux into the thermal motion was observed just in the shock precursor region, where the wave interaction with the particles is strongest.

In isolated pulsars, such a strong wave is launched with a small amplitude and high velocity, so that, initially, the streaming is large. A different situation arises in binary systems, where the external conditions require the waves that have large amplitudes, small velocities, and small particle streaming. In this case, instabilities are likely to set in close to the launching site, because (6.83) may not be satisfied. Therefore, in binary systems, even though a superluminal solution may be allowed by the pressure conditions, it may be destroyed immediately after launching, and the shock would be located very close to the conversion radius. However, there are several possible stabilizing mechanisms that could prevent the quick disruption of the strong wave. Firstly, electromagnetic waves in plasmas can be stabilized against longitudinal perturbations by the presence of a magnetic field [16]. Secondly, in a finite temperature plasma, longitudinal perturbations can be easily damped. One may expect that the instabilities are an artifact of the cold plasma assumption. Lastly, determining of the stability of nonlinear waves requires a fully nonlinear consideration as the perturbation grows into a nonlinear regime. As shown in numerical calculations [86] there might exist a saturation threshold for the instabilities.

The stability of linearly polarized waves in the presence of a magnetic field perpendicular to the direction of motion was studied by Asseo et al. [16]. They found that the magnetic field has a stabilizing property for this mode. This situation is of interest for pulsars, because in a striped wind, the nonvanishing phase averaged magnetic field is perpendicular to the direction of the wave motion. Therefore, even if in the equatorial plane the waves are unstable and the shock forms just after the wave has been launched, in higher latitudes it may form considerably further, when the wave slows down due to spherical expansion or radiation reaction. For completeness we also mention that the case of circularly polarized waves and a magnetic field in the direction of motion was investigated in [120]. They concluded that in a general case the inclusion of the magnetic field does not stabilize this mode. However, in the most interesting case of nonvanishing streaming and the magnetic field both included, the instability growth rate can be substantially decreased.

As we mentioned, a self-consistent solution in a cold plasma is obtained by a precise phasing between particles and fields. In a finite temperature the spread in particle momenta relaxes this phasing and, therefore, the system may be more tolerant of the perturbations. Clemmow [43] and Lee & Lerche [119] constructed a strong, self-consistent wave solution in a warm plasma. Lee & Lerche [121] added a magnetic field, and investigated the stability of the solution against the same kind of perturbations as previously. Their analysis was restricted to a nonrelativistic plasma $p_\perp \ll mc$. In particular, the plasma was cold in the direction of the wave propagation and, since this distribution is anisotropic and may be intrinsically unstable, they focused on the modes that have the vanishing growth rate when the wave amplitude goes to zero. They concluded that the spread in the particle distribution does not affect the instability growth rate. In the application we discuss here, the perpendicular momentum is highly relativistic, but up to date no calculations have been published for this case.

All of the outlined studies were based on the perturbation technique, and linearization of the perturbed two-fluid and Maxwell equations. When the perturbation grows into a nonlinear regime a fully nonlinear stability analysis is needed, however. Such a nonlinear analysis, in the case of a circularly polarized, strong wave in a magnetized plasma, was carried out in [189, 190]. Their numerical analysis showed the sharpening of a perturbing density wave, leading to a shock-like structure as the perturbation evolves to a nonlinear regime. The fate of instabilities depends in this case on the relative timescale of the evolution of the excited waves into a nonlinear regime, and a timescale for their spatial diffusion out of the system. Somewhat earlier, the need for such a fully nonlinear investigation was pointed out by Jancarik & Tsytovich [86], who investigated a subluminal electrostatic mode, and found that the monochromatic perturbations grow in the beginning, but saturate and decay before they would reach a high level. Stochastic initial perturbations were shown to be slightly damped.

One more question can be posed, concerning the dependence of the wave stability on the

wave polarization. The case of linearly polarized waves was investigated numerically by Leboeuf et al. [117]. First, they investigated a sinusoidal wave and perturbed the particle momenta in the direction of the wave electric field, finding that (1) if the wave has the frequency well above the cut-off, the waveform changes little; (2) if the frequency is close to the cut-off frequency, the waveform steepens (more energy is transfered to the particles as the frequency gets closer to the cut-off frequency). In both cases, the significant parallel momenta are gained by the particles. As the wave steepens, the energy is dissipated, and a hot plasma with large particle velocities in the longitudinal direction is generated. Density spikes initially appear at the maxima and minima of the wave magnetic field, but they propagate with the speed smaller than the wave group speed. This is the formation of a longitudinal density wave. In the case of a self-consistent sawtooth wave, the energy exchange between the fields and the particles reveals the oscillatory behavior. Also in this case a significant gain in the parallel momenta was observed. Independent of the initial waveform then, the final stationary state is a very hot plasma in the direction of a wave propagation, with twice as many peaks in the density as in the fields. As the wave shape steepens, there is a tendency towards the equipartition of the electromagnetic and particle fluxes.

6.4 Summary and conclusions

We extended a model of Kirk [97] and Arka & Kirk [10], in which an MHD striped wind converts into a strong electromagnetic wave at some distance to the termination shock. This new mode can propagate only beyond a critical radius (in a sufficiently underdense plasma), and can be viewed as a shock precursor. It transfers the energy from the fields to the particles, and thus provides a solution to the magnetization problem in pulsar winds.

In particular, we investigated its radial propagation, and we showed that one can find a unique, self-consistent solution matching asymptotically to the external pressure, defined by the surroundings. This procedure can be applicable to the isolated pulsars, whose winds form shocks at large distances. We conclude that the conversion process does not occur spontaneously, but rather as an effect of the external conditions.

This picture may change when the interaction of particles and photons is no longer a negligible effect. Thus, we investigated the wave evolution when the nonlinear inverse Compton, and/or external Compton processes contribute. Both these effects, and also the radial expansion cause the wave to slow down, and decrease the streaming of the particles through the wave until the parametric instabilities can set in. We suggest that this underlies the formation of a shock.

We identified two regimes for the conditions at shocks:

- one with high external pressures, which require an EM wave to be launched in a region where it cannot propagate; thus, in this regime, no electromagnetic precursor can exist. A shock is possibly formed by the interactions of the inner, MHD striped wind with the external medium; the energy dissipation mechanism which has been proposed is that of reconnection [134], when the stripes of opposite polarity are compressed at the shock,
- one with lower external pressures, in which the superluminal wave might be generated in the shock precursor, damped and merged to the surroundings; the possible damping mechanisms include the nonlinear IC process, IC scattering on the external photon field, and wavebreaking parametric instabilities in the outflow.

The winds from isolated pulsars belong to the second category. Pulsars in binary systems, on the other hand, may be embedded in high pressure winds of companion stars, and a regime of the shock conditions can change with the orbital phase. An example is the binary PSR B1259-63. If the regime switch occurs 30 days after periastron, one can expect IC emission from the shock precursor in the range of a few hundred MeV, consistent with the flare observed by Fermi-LAT. If this is true, mass loading in the magnetosphere is constrained to a very moderate value, consistent with current pulsar models. At the same time, one can expect a twin, optical flare

due to the nonlinear inverse Compton mechanism, but its emission may be hidden beneath that of the much more luminous companion star.

Summary

Highly magnetized, relativistic outflows, despite years of investigation, remain mysterious in many aspects. One of the outstanding issues is an understanding of how the energy that is extracted electromagnetically from a rotating compact object, can be transferred from the fields to the plasma particles. Observations show that it can happen very abruptly, at the highest energies, and can occur on the very short timescales. These properties are hard to accommodate within the standard models of Poynting-flux dominated winds.

The outflow from black holes is typically characterized by collimated jets, while the wind of obliquely rotating pulsars form a corrugated current sheet that separates stripes of alternating magnetic field. Close to the central object, the outflow is thought to be dense, but as it propagates outwards, the density drops and the field can no longer be regarded as stationarily frozen-in. The ideal MHD approximation breaks down, and a more sophisticated treatment is necessary. The breakdown follows from the increasing importance of the particle inertia in a charge-starved plasma, and consequently, the plasma conductivity becomes affected by the relativistic drift-speed of the plasma species. The simplest model that can account for these effects is that of two cold fluids, coupled to the electromagnetic fields. The system is solved using a short-wavelength perturbation analysis, which in the lowest order gives an exact solution for the large-amplitude plane waves, and in the first order describes their slow radial evolution. In the following we summarize the main conclusions of this work.

Blazar jets

In unconfined, initially dense outflows, of particular interest are the waves of subluminal phase velocity, which, at least close to their launch, resemble more closely MHD waves than electromagnetic. In blazars, we suggested that such a wave is launched from the polar regions of a rotating black hole and propagates radially in the direction of a jet. We investigated a special solution: a large-amplitude circularly polarized, Alfvén-like mode, characterized by a magnetic shear – in the comoving frame it has only a static magnetic field that rotates one full revolution per wavelength, with the magnetic vector everywhere parallel to the direction of the current. The particles move radially in resonance with this wave. The radial evolution depends on two parameters that specify the supermagnetosonic jet at launch: the dimensionless luminosity a_0 and the outflow magnetization σ_0 (i.e., the ratio of the Poynting flux to the particle energy flux) or, alternatively, the energy per particle μ carried by the wave.

Although the wave can propagate in a high density plasma, its evolution changes dramatically when the plasma becomes rarefied, i.e., a coasting, constant velocity outflow starts to accelerate when the particle inertia becomes an important contribution to the energy-momentum flux. This occurs at the distance $r \approx (a_0/\sigma_0)(c/\omega)$. For the parameters, inferred for the source PKS 2155-304, this takes place on parsec scales. Pre-existing high-energy particle emission is expected to be modulated with the wave frequency, and we showed that these fluctuations are not smeared out by the difference in the light-travel time to the observer provided the pair loading in the magnetosphere is sufficiently low. The model can provide an explanation of the extremely fast variability in the TeV band, exhibited by some blazars.

Pulsar winds

Pulsar winds, as opposed to blazar jets, are confined flows, terminated at roughly standing shocks. Their magnetization is thought to be lower than that of the jets, because the pulsar outflows have a larger pair multiplicity. Thus, before charge starvation affects the MHD wave, other modes available in underdense plasmas may take over. In particular, beyond a certain critical radius, the propagation of a large-amplitude electromagnetic wave becomes possible, and an MHD pulsar wind can convert to this wave before reaching the termination shock. In this model, the electromagnetic wave is a shock precursor, which efficiently transfers the electromagnetic energy to the particles, providing a possible solution to the magnetization problem in pulsar winds.

We showed that the mode conversion is driven by the boundary conditions, imposed by an external medium. These conditions, together with the MHD wind parameters, specify the new mode uniquely. Thus, a self-consistent solution matching asymptotically to the pressure of the surroundings can be found, and we discussed its evolution when the nonlinear inverse Compton process (i.e., radiation reaction of the particles accelerated in the wave fields) becomes important. In particular, we investigated the role this mechanism can play in the formation of pulsar wind termination shocks.

Two different regimes of shocks were identified: the MHD one, when the external pressure is so high that the required conversion radius for an electromagnetic wave falls below the critical radius; in this case the shock is determined by the direct interaction of the striped wind with the surroundings. The second one is that of lower external pressures, when the electromagnetic precursor can be launched beyond the critical radius, and subsequently slowed down by the radiation reaction process is efficient, or the radial expansion of the flow. The shock forms when the parametric instabilities set in, as a result of low streaming in the wave.

In isolated pulsars the radiation reaction is inefficient, because they are confined by the low-pressure environment, which requires the electromagnetic waves to have smaller amplitudes at launch. In the binary PSR B1259-63 a young pulsar is immersed in the wind of its companion star, and, depending on the orbital phase, both shock regimes can be probed. In particular, a switch between the regimes may manifest itself via the enhanced emission from both the nonlinear inverse Compton and the external Compton processes. If the regime change occurs when the orbital separation is that of 30 days after the periastron, one can expect the emission at few hundred MeV, consistent with the flare observed by Fermi-LAT. This would constrain mass loading in the magnetosphere at a very moderate value, consistent with pulsar models.

Propagation of large-amplitude waves in Poynting-flux dominated outflows has received very little attention in the literature, and only in the limited cases, due to the complexity of the underlying physics. These modes, however, can be an important ingredient in models of relativistic flows, because they are capable of describing charge-starved, highly-magnetized systems, for which standard approaches do not apply. Thus, nonlinear waves prove to give new insight into these astrophysical phenomena, and a deeper understanding of the mechanisms that govern the energy transfer between the electromagnetic fields and the plasma particles.

Bibliography

[1] A. A. Abdo et al. Gamma-Ray Flares from the Crab Nebula. *Science*, 331:739–, February 2011.

[2] M. A. Abramowicz, B. Carter, and J. P. Lasota. Optical reference geometry for stationary and static dynamics. *General Relativity and Gravitation*, 20:1173–1183, November 1988.

[3] F. Aharonian et al. An Exceptional Very High Energy Gamma-Ray Flare of PKS 2155-304. ApJ, 664:L71–L74, August 2007.

[4] A. Akhiezer and R. Polovin. *Sov. Phys. JETP*, 3:696, 1956.

[5] J. Albert et al. Variable Very High Energy γ-Ray Emission from Markarian 501. ApJ, 669:862–883, November 2007.

[6] J. Aleksić et al. MAGIC Discovery of Very High Energy Emission from the FSRQ PKS 1222+21. ApJ, 730:L8, March 2011.

[7] J. Aleksić et al. Observations of the Crab Pulsar between 25 and 100 GeV with the MAGIC I Telescope. ApJ, 742:43, November 2011.

[8] E. Aliu et al. Observation of Pulsed γ-Rays Above 25 GeV from the Crab Pulsar with MAGIC. *Science*, 322:1221–, November 2008.

[9] E. Aliu et al. Detection of Pulsed Gamma Rays Above 100 GeV from the Crab Pulsar. *Science*, 334:69–, October 2011.

[10] I. Arka and J. G. Kirk. Superluminal Waves in Pulsar Winds. ApJ, 745:108, February 2012.

[11] P. J. Armitage and P. Natarajan. The Blandford-Znajek Mechanism and the Emission from Isolated Accreting Black Holes. ApJ, 523:L7–L10, September 1999.

[12] R. Arnowitt, S. Deser, and C. W. Misner. *in Gravitation: An Introduction to Current Research (L. Witten, Ed.).* 1962.

[13] J. Arons. Pair creation above pulsar polar caps - Geometrical structure and energetics of slot gaps. ApJ, 266:215–241, March 1983.

[14] E. Asseo. Pair plasma in pulsar magnetospheres. *Plasma Physics and Controlled Fusion*, 45:853–867, June 2003.

[15] E. Asseo, C. F. Kennel, and R. Pellat. Synchro-Compton radiation damping of relativistically strong linearly polarized plasma waves. A&A, 65:401–408, May 1978.

[16] E. Asseo, X. Llobet, and G. Schmidt. Instability of large-amplitude electromagnetic waves in plasmas. Phys. Rev. A, 22:1293, September 1980.

[17] E. Asseo, R. Pellat, and X. Llobet. Spherical propagation of large amplitude pulsar waves. A&A, 139:417–425, October 1984.

[18] L. Ball and J. G. Kirk. Probing pulsar winds using inverse compton scattering. *Astroparticle Physics*, 12:335–349, January 2000.

[19] M. V. Barkov, F. A. Aharonian, S. V. Bogovalov, S. R. Kelner, and D. Khangulyan. Rapid TeV Variability in Blazars as a Result of Jet-Star Interaction. ApJ, 749:119, April 2012.

[20] J. J. Barnard and J. Arons. Pair production and pulsar cutoff in magnetized neutron stars with nondipolar magnetic geometry. ApJ, 254:713–734, March 1982.

[21] W. Becker. X-Ray Emission from Pulsars and Neutron Stars. In W. Becker, editor, *Astrophysics and Space Science Library*, volume 357 of *Astrophysics and Space Science Library*, page 91, 2009.

[22] W. Bednarek. On the origin of sub-TeV gamma-ray pulsed emission from rotating neutron stars. MNRAS, 424:2079–2085, August 2012.

[23] M. C. Begelman, A. C. Fabian, and M. J. Rees. Implications of very rapid TeV variability in blazars. MNRAS, 384:L19–L23, February 2008.

[24] P. N. Best and T. M. Heckman. On the fundamental dichotomy in the local radio-AGN population: accretion, evolution and host galaxy properties. MNRAS, 421:1569–1582, April 2012.

[25] M. F. Bietenholz, J. J. Hester, D. A. Frail, and N. Bartel. The Crab Nebula's Wisps in Radio and Optical. ApJ, 615:794–804, November 2004.

[26] D. Bini, P. Carini, and R. T. Jantzen. The Intrinsic Derivative and Centrifugal Forces in General Relativity: I.. Theoretical Foundations. *International Journal of Modern Physics D*, 6:1–38, 1997.

[27] D. Bini, P. Carini, and R. T. Jantzen. The Intrinsic Derivative and Centrifugal Forces in General Relativity:. II. Applications to Circular Orbits in Some Familiar Stationary Axisymmetric Spacetimes. *International Journal of Modern Physics D*, 6:143–198, 1997.

[28] J. Bičák and L. Dvořák. Stationary electromagnetic fields around black holes. II. General solutions and the fields of some special sources near a Kerr black hole. *General Relativity and Gravitation*, 7:959–983, December 1976.

[29] R. D. Blandford. Accretion disc electrodynamics - A model for double radio sources. MNRAS, 176:465–481, September 1976.

[30] R. D. Blandford. Physical processes in active galactic nuclei. In R. D. Blandford, H. Netzer, L. Woltjer, T. J.-L. Courvoisier, and M. Mayor, editors, *Active Galactic Nuclei*, pages 161–275, 1990.

[31] R. D. Blandford and D. G. Payne. Hydromagnetic flows from accretion discs and the production of radio jets. MNRAS, 199:883–903, June 1982.

[32] R. D. Blandford and R. L. Znajek. Electromagnetic extraction of energy from Kerr black holes. MNRAS, 179:433–456, May 1977.

[33] S. V. Bogovalov. On the physics of cold MHD winds from oblique rotators. A&A, 349:1017–1026, September 1999.

[34] E. Boldt and P. Ghosh. Cosmic rays from remnants of quasars? MNRAS, 307:491–494, August 1999.

[35] V. B. Braginskii, C. M. Caves, and K. S. Thorne. Laboratory experiments to test relativistic gravity. Phys. Rev. D, 15:2047–2068, April 1977.

[36] R. Buckley. Pulsar magnetospheres with arbitrary geometry in the force-free approximation. MNRAS, 180:125–140, July 1977.

[37] R. Buehler et al. Gamma-Ray Activity in the Crab Nebula: The Exceptional Flare of 2011 April. ApJ, 749:26, April 2012.

[38] M. Camenzind. *Compact objects in astrophysics : white dwarfs, neutron stars, and black holes*. 2007.

[39] A. Cavaliere and V. D'Elia. The Blazar Main Sequence. ApJ, 571:226–233, May 2002.

[40] A. F. Cheng and M. A. Ruderman. Bunching mechanism for coherent curvature radiation in pulsar magnetospheres. ApJ, 212:800–806, March 1977.

[41] K. S. Cheng, C. Ho, and M. Ruderman. Energetic radiation from rapidly spinning pulsars. I - Outer magnetosphere gaps. II - VELA and Crab. ApJ, 300:500–539, January 1986.

[42] P. C. Clemmow. Nonlinear waves in a cold plasma by Lorentz transformation. *Journal of Plasma Physics*, 12:297–317, October 1974.

[43] P. C. Clemmow. Nonlinear waves in a hot plasma by Lorentz transformation. *Journal of Plasma Physics*, 13:231, April 1975.

[44] J. M. Cohen and R. M. Wald. Note on the Angular Momentum and Mass of Gravitational Geons. *Journal of Mathematical Physics*, 13:543–545, April 1972.

[45] I. Contopoulos and A. Spitkovsky. Revised Pulsar Spin-down. ApJ, 643:1139–1145, June 2006.

[46] J. Contopoulos. A Simple Type of Magnetically Driven Jets: an Astrophysical Plasma Gun. ApJ, 450:616, September 1995.

[47] J. Contopoulos and R. V. E. Lovelace. Magnetically driven jets and winds: Exact solutions. ApJ, 429:139–152, July 1994.

[48] F. V. Coroniti. Magnetically striped relativistic magnetohydrodynamic winds - The Crab Nebula revisited. ApJ, 349:538–545, February 1990.

[49] J. K. Daugherty and A. K. Harding. Electromagnetic cascades in pulsars. ApJ, 252:337–347, January 1982.

[50] J. K. Daugherty and A. K. Harding. Comptonization of thermal photons by relativistic electron beams. ApJ, 336:861–874, January 1989.

[51] J. K. Daugherty and A. K. Harding. Polar CAP models of gamma-ray pulsars: Emision from single poles of nearly aligned rotators. ApJ, 429:325–330, July 1994.

[52] O. C. de Jager. Lower Limits on Pulsar Pair Production Multiplicities from H.E.S.S. Observations of Pulsar Wind Nebulae. ApJ, 658:1177–1182, April 2007.

[53] B. S. Dewitt and R. W. Brehme. Radiation damping in a gravitational field. *Annals of Physics*, 9:220–259, February 1960.

[54] A. Di Piazza, C. Müller, K. Z. Hatsagortsyan, and C. H. Keitel. Extremely high-intensity laser interactions with fundamental quantum systems. *ArXiv e-prints*, November 2011.

[55] J. F. Drake, P. K. Kaw, Y. C. Lee, G. Schmid, C. S. Liu, and M. N. Rosenbluth. Parametric instabilities of electromagnetic waves in plasmas. *Physics of Fluids*, 17:778–785, April 1974.

[56] G. Dubus. Gamma-ray binaries: pulsars in disguise? A&A, 456:801–817, September 2006.

[57] J. Dyks and B. Rudak. Two-Pole Caustic Model for High-Energy Light Curves of Pulsars. ApJ, 598:1201–1206, December 2003.

[58] A. Ferrari. Modeling Extragalactic Jets. ARA&A, 36:539–598, 1998.

[59] B. Finkbeiner, H. Herold, T. Ertl, and H. Ruder. Effects of radiation damping on particle motion in pulsar vacuum fields. A&A, 225:479–487, November 1989.

[60] J. A. Gaidos et al. Extremely rapid bursts of TeV photons from the active galaxy Markarian 421. Nature, 383:319–320, September 1996.

[61] Y. A. Gallant and R. J. Tuffs. Infrared Observations of the Crab Nebula. In M. Kramer, N. Wex, and R. Wielebinski, editors, *IAU Colloq. 177: Pulsar Astronomy - 2000 and Beyond*, volume 202 of *Astronomical Society of the Pacific Conference Series*, page 503, 2000.

[62] Y. A. Gallant and R. J. Tuffs. Infrared Observations of the Crab Nebula. In P. O. Slane and B. M. Gaensler, editors, *Neutron Stars in Supernova Remnants*, volume 271 of *Astronomical Society of the Pacific Conference Series*, page 161, 2002.

[63] M. Georganopoulos and D. Kazanas. Decelerating Flows in TeV Blazars: A Resolution to the BL Lacertae-FR I Unification Problem. ApJ, 594:L27–L30, September 2003.

[64] G. Ghisellini and P. Madau. On the origin of the gamma-ray emission in blazars. MNRAS, 280:67–76, May 1996.

[65] G. Ghisellini and F. Tavecchio. Rapid variability in TeV blazars: the case of PKS2155-304. MNRAS, 386:L28–L32, May 2008.

[66] G. Ghisellini, F. Tavecchio, G. Bodo, and A. Celotti. TeV variability in blazars: how fast can it be? MNRAS, 393:L16–L20, February 2009.

[67] P. Ghosh and M. A. Abramowicz. Electromagnetic extraction of rotational energy from disc-fed black holes - The strength of the Blandford-Znajek process. MNRAS, 292:887, December 1997.

[68] D. Giannios, D. A. Uzdensky, and M. C. Begelman. Fast TeV variability in blazars: jets in a jet. MNRAS, 395:L29–L33, May 2009.

[69] J. Gil and D. Mitra. Vacuum Gaps in Pulsars and PSR J2144-3933. ApJ, 550:383–391, March 2001.

[70] T. Gold. Rotating Neutron Stars and the Nature of Pulsars. Nature, 221:25–27, January 1969.

[71] P. Goldreich and W. H. Julian. Pulsar Electrodynamics. ApJ, 157:869, August 1969.

[72] O. V. Gotchev, P. Y. Chang, J. P. Knauer, D. D. Meyerhofer, O. Polomarov, J. Frenje, C. K. Li, M. J.-E. Manuel, R. D. Petrasso, J. R. Rygg, F. H. Séguin, and R. Betti. Laser-Driven Magnetic-Flux Compression in High-Energy-Density Plasmas. *Physical Review Letters*, 103(21):215004, November 2009.

[73] E. Gourgoulhon, editor. *3+1 Formalism in General Relativity*, volume 846 of *Lecture Notes in Physics, Berlin Springer Verlag*, 2012.

[74] J. Granot, S. S. Komissarov, and A. Spitkovsky. Impulsive acceleration of strongly magnetized relativistic flows. MNRAS, 411:1323–1353, February 2011.

[75] A. Gruzinov. Stability in Force-Free Electrodynamics. *ArXiv Astrophysics e-prints*, February 1999.

[76] J. E. Gunn and J. P. Ostriker. Magnetic Dipole Radiation from Pulsars. Nature, 221:454–456, February 1969.

[77] J. E. Gunn and J. P. Ostriker. On the Motion and Radiation of Charged Particles in Strong Electromagnetic Waves. I. Motion in Plane and Spherical Waves. ApJ, 165:523, May 1971.

[78] A. K. Harding. Physics in strong magnetic fields near neutron stars. *Science*, 251:1033–1038, March 1991.

[79] A. K. Harding. Physical Processes in Strong Magnetic Fields of Neutron Stars. In G. Cusumano, E. Massaro, and T. Mineo, editors, *Pulsars, AXPs and SGRs Observed with BeppoSAX and Other Observatories*, pages 127–138, July 2003.

[80] A. K. Harding. High-energy Emission from the Polar Cap and Slot Gap. In W. Becker, editor, *Astrophysics and Space Science Library*, volume 357 of *Astrophysics and Space Science Library*, page 521, 2009.

[81] A. K. Harding, A. G. Muslimov, and B. Zhang. Regimes of Pulsar Pair Formation and Particle Energetics. ApJ, 576:366–375, September 2002.

[82] S. Heinz and M. C. Begelman. Jet Acceleration by Tangled Magnetic Fields. ApJ, 535:104–117, May 2000.

[83] J. A. Hibschman and J. Arons. Pair Production Multiplicities in Rotation-powered Pulsars. ApJ, 560:871–884, October 2001.

[84] J. M. Hobbs. A vierbein formalism of radiation damping. *Annals of Physics*, 47:141–165, March 1968.

[85] N. J. Holloway. Pulsars-p-n junctions in pulsar magnetospheres. *Nature Physical Science*, 246:6, November 1973.

[86] J. Jancarik and V.N. Tsytovich. Stability of large-amplitude relativistic non-linear plasma waves. *Nuclear Fusion*, 13(6):807, 1973.

[87] R. T. Jantzen, P. Carini, and D. Bini. The many faces of gravitoelectromagnetism. *Annals of Physics*, 215:1–50, April 1992.

[88] S. Johnston, R. N. Manchester, A. G. Lyne, L. Nicastro, and J. Spyromilio. Radio and Optical Observations of the PSR:B1259-63 / SS:2883 Be-Star Binary System. MNRAS, 268:430, May 1994.

[89] B.-I. Jun. Interaction of the Pulsar-Driven Wind with Supernova Ejecta. In D. A. Clarke and M. J. West, editors, *Computational Astrophysics; 12th Kingston Meeting on Theoretical Astrophysics*, volume 123 of *Astronomical Society of the Pacific Conference Series*, page 94, 1997.

[90] C. F. Kennel and F. V. Coroniti. Confinement of the Crab pulsar's wind by its supernova remnant. ApJ, 283:694–709, August 1984.

[91] C. F. Kennel and F. V. Coroniti. Magnetohydrodynamic model of Crab nebula radiation. ApJ, 283:710–730, August 1984.

[92] C. F. Kennel, F. S. Fujimura, and R. Pellat. Pulsar magnetospheres. Space Sci. Rev., 24:407–436, December 1979.

[93] C. F. Kennel and R. Pellat. Relativistic nonlinear plasma waves in a magnetic field. *Journal of Plasma Physics*, 15:335–355, June 1976.

[94] R. P. Kerr. Gravitational Field of a Spinning Mass as an Example of Algebraically Special Metrics. *Physical Review Letters*, 11:237–238, September 1963.

[95] D. Khangulyan, F. A. Aharonian, S. V. Bogovalov, and M. Ribó. Post-periastron Gamma-Ray Flare from PSR B1259-63/LS 2883 as a Result of Comptonization of the Cold Pulsar Wind. ApJ, 752:L17, June 2012.

[96] R. Khanna. On the magnetohydrodynamic description of a two-component plasma in the Kerr metric. MNRAS, 294:673, March 1998.

[97] J. G. Kirk. Waves in pulsar winds. *Plasma Physics and Controlled Fusion*, 52(12):124029, December 2010.

[98] J. G. Kirk, L. Ball, and O. Skjaeraasen. Inverse Compton emission of TeV gamma rays from PSR B1259-63. *Astroparticle Physics*, 10:31–45, January 1999.

[99] J. G. Kirk and P. Duffy. TOPICAL REVIEW: Particle acceleration and relativistic shocks. *Journal of Physics G Nuclear Physics*, 25:163, August 1999.

[100] J. G. Kirk, Y. Lyubarsky, and J. Petri. The Theory of Pulsar Winds and Nebulae. In W. Becker, editor, *Astrophysics and Space Science Library*, volume 357 of *Astrophysics and Space Science Library*, page 421, 2009.

[101] J. G. Kirk and I. Mochol. Charge-starved, Relativistic Jets and Blazar Variability. ApJ, 729:104, March 2011.

[102] S. Koide. Magnetic extraction of black hole rotational energy: Method and results of general relativistic magnetohydrodynamic simulations in Kerr space-time. Phys. Rev. D, 67(10):104010, May 2003.

[103] S. Koide. Generalized Relativistic Magnetohydrodynamic Equations for Pair and Electron-Ion Plasmas. ApJ, 696:2220–2233, May 2009.

[104] S. Koide, K. Shibata, and T. Kudoh. General Relativistic Magnetohydrodynamic Simulations of Jets from Black Hole Accretions Disks: Two-Component Jets Driven by Nonsteady Accretion of Magnetized Disks. ApJ, 495:L63, March 1998.

[105] S. Koide, K. Shibata, T. Kudoh, and D. L. Meier. Extraction of Black Hole Rotational Energy by a Magnetic Field and the Formation of Relativistic Jets. *Science*, 295:1688–1691, March 2002.

[106] S. S. Komissarov. Electrodynamics of black hole magnetospheres. MNRAS, 350:427–448, May 2004.

[107] S. S. Komissarov. Observations of the Blandford-Znajek process and the magnetohydrodynamic Penrose process in computer simulations of black hole magnetospheres. MNRAS, 359:801–808, May 2005.

[108] S. S. Komissarov. Blandford-Znajek Mechanism versus Penrose Process. *Journal of Korean Physical Society*, 54:2503, June 2009.

[109] S. S. Komissarov. Magnetic acceleration of relativistic jets. Mem. Soc. Astron. Italiana, 82:95, 2011.

[110] S. S. Komissarov and Y. E. Lyubarsky. Synchrotron nebulae created by anisotropic magnetized pulsar winds. MNRAS, 349:779–792, April 2004.

[111] J. Krause-Polstorff and F. C. Michel. Electrosphere of an aligned magnetized neutron star. MNRAS, 213:43P–49P, March 1985.

[112] J. Krause-Polstorff and F. C. Michel. Pulsar space charging. A&A, 144:72–80, March 1985.

[113] W. L. Kruer, editor. *The physics of laser plasma interactions*, volume 73, 1988.

[114] W. L. Kruer, P. K. Kaw, J. M. Dawson, and C. Oberman. Anomalous High-Frequency Resistivity and Heating of a Plasma. *Physical Review Letters*, 24:987–990, May 1970.

[115] L. D. Landau and E. M. Lifshitz. *The classical theory of fields*. 1975.

[116] J. D. Landstreet. Search for Optical Circular Polarization in the Crab Nebula. Nature, 230:103, March 1971.

[117] J. N. Leboeuf, M. Ashour-Abdalla, T. Tajima, C. F. Kennel, F. V. Coroniti, and J. M. Dawson. Ultrarelativistic waves in overdense electron-positron plasmas. Phys. Rev. A, 25:1023–1039, February 1982.

[118] M. A. Lee and I. Lerche. On the stability of self-consistent large amplitude waves in a cold plasma. I - Transverse circularly polarized waves in the absence of a large scale magnetic field. *Journal of Plasma Physics*, 20:313–328, December 1978.

[119] M. A. Lee and I. Lerche. On self-consistent waves and their stability in warm plasma. I - Construction of the self-consistent waves. *Journal of Plasma Physics*, 21:141–149, February 1979.

[120] M. A. Lee and I. Lerche. On the stability of self-consistent large-amplitude waves in a cold plasma. Part 3. Transverse circularly polarized waves in the presence of a large-scale magnetic field. *Journal of Plasma Physics*, 21:43, December 1979.

[121] M. A. Lee and I. Lerche. On self-consistent waves and their stability in warm plasmas. II - Instability of circularly polarized waves both in the presence and the absence of an ambient magnetic field. *Journal of Plasma Physics*, 24:89–102, August 1980.

[122] A. Levinson. Particle Acceleration and Curvature TeV Emission by Rotating, Supermassive Black Holes. *Physical Review Letters*, 85:912–915, July 2000.

[123] A. Levinson. On the Origin of Rapid Flares in TeV Blazars. ApJ, 671:L29–L32, December 2007.

[124] A. Levinson. Interaction of a Magnetized Shell with an Ambient Medium: Limits on Impulsive Magnetic Acceleration. ApJ, 720:1490–1499, September 2010.

[125] A. Levinson. Relativistic jets at high energies. 2010.

[126] A. Levinson, D. Melrose, A. Judge, and Q. Luo. Large-Amplitude, Pair-creating Oscillations in Pulsar and Black Hole Magnetospheres. ApJ, 631:456–465, September 2005.

[127] Z.-Y. Li, T. Chiueh, and M. C. Begelman. Electromagnetically driven relativistic jets - A class of self-similar solutions. ApJ, 394:459–471, August 1992.

[128] M. L. Lister, M. H. Cohen, D. C. Homan, M. Kadler, K. I. Kellermann, Y. Y. Kovalev, E. Ros, T. Savolainen, and J. A. Zensus. MOJAVE: Monitoring of Jets in Active Galactic Nuclei with VLBA Experiments. VI. Kinematics Analysis of a Complete Sample of Blazar Jets. AJ, 138:1874–1892, December 2009.

[129] M. A. Livingstone, V. M. Kaspi, F. P. Gavriil, R. N. Manchester, E. V. G. Gotthelf, and L. Kuiper. New phase-coherent measurements of pulsar braking indices. Ap&SS, 308:317–323, April 2007.

[130] M. Livio. The Formation Of Astrophysical Jets. In D. T. Wickramasinghe, G. V. Bicknell, and L. Ferrario, editors, *IAU Colloq. 163: Accretion Phenomena and Related Outflows*, volume 121 of *Astronomical Society of the Pacific Conference Series*, page 845, 1997.

[131] R. V. E. Lovelace. Dynamo model of double radio sources. Nature, 262:649–652, August 1976.

[132] Y. Lyubarsky. Asymptotic Structure of Poynting-Dominated Jets. ApJ, 698:1570–1589, June 2009.

[133] Y. Lyubarsky and J. G. Kirk. Reconnection in a Striped Pulsar Wind. ApJ, 547:437–448, January 2001.

[134] Y. E. Lyubarsky. The termination shock in a striped pulsar wind. MNRAS, 345:153–160, October 2003.

[135] Y. E. Lyubarsky. Transformation of the Poynting flux into kinetic energy in relativistic jets. MNRAS, 402:353–361, February 2010.

[136] M. Lyutikov and M. Lister. Resolving Doppler-factor Crisis in Active Galactic Nuclei: Non-steady Magnetized Outflows. ApJ, 722:197–203, October 2010.

[137] D. MacDonald and K. S. Thorne. Black-hole electrodynamics - an absolute-space/universal-time formulation. MNRAS, 198:345–382, January 1982.

[138] J. Magorrian, S. Tremaine, D. Richstone, R. Bender, G. Bower, A. Dressler, S. M. Faber, K. Gebhardt, R. Green, C. Grillmair, J. Kormendy, and T. Lauer. The Demography of Massive Dark Objects in Galaxy Centers. AJ, 115:2285–2305, June 1998.

[139] L. Maraschi, M. Colpi, G. Ghisellini, A. Perego, and F. Tavecchio. On the role of black hole spin and accretion in powering relativistic jets in AGN. *Journal of Physics Conference Series*, 355(1):012016, March 2012.

[140] C. Max and F. Perkins. Strong Electromagnetic Waves in Overdense Plasmas. *Physical Review Letters*, 27:1342–1345, November 1971.

[141] C. E. Max. Parametric instability of a relativistically strong electromagnetic wave. *Physics of Fluids*, 16:1480–1489, 1973.

[142] C. E. Max. Steady-state solutions for relativistically strong electromagnetic waves in plasmas. *Physics of Fluids*, 16:1277–1288, 1973.

[143] J. C. McKinney and R. D. Blandford. Stability of relativistic jets from rotating, accreting black holes via fully three-dimensional magnetohydrodynamic simulations. MNRAS, 394:L126–L130, March 2009.

[144] J. C. McKinney and C. F. Gammie. A Measurement of the Electromagnetic Luminosity of a Kerr Black Hole. ApJ, 611:977–995, August 2004.

[145] Z. Medin and D. Lai. Pair cascades in the magnetospheres of strongly magnetized neutron stars. MNRAS, 406:1379–1404, August 2010.

[146] A. Melatos and D. B. Melrose. Energy transport in a rotation-modulated pulsar wind. MNRAS, 279:1168–1190, April 1996.

[147] D. B. Melrose and R. Yuen. Obliquely Rotating Pulsars: Screening of the Inductive Electric Field. ApJ, 745:169, February 2012.

[148] F. C. Michel. Relativistic Stellar-Wind Torques. ApJ, 158:727, November 1969.

[149] F. C. Michel. Rotating Magnetosphere: a Simple Relativistic Model. ApJ, 180:207–226, February 1973.

[150] F. C. Michel. Rotating Magnetospheres: an Exact 3-D Solution. ApJ, 180:L133, March 1973.

[151] F. C. Michel. Magnetic structure of pulsar winds. ApJ, 431:397–401, August 1994.

[152] C. W. Misner, K. S. Thorne, and J. A. Wheeler. *Gravitation*. 1973.

[153] M. Mościbrodzka, C. F. Gammie, J. C. Dolence, and H. Shiokawa. Pair Production in Low-luminosity Galactic Nuclei. ApJ, 735:9, July 2011.

[154] E. J. Mueller. Strong Staggered Flux Lattices for Cold Atoms. *Physcs Online Journal*, 4:107, December 2011.

[155] R. Narayan and T. Piran. Variability in blazars: clues from PKS 2155-304. MNRAS, 420:604–612, February 2012.

[156] A. Y. Neronov, D. V. Semikoz, and I. I. Tkachev. Ultra-high energy cosmic ray production in the polar cap regions of black hole magnetospheres. *New Journal of Physics*, 11(6):065015, June 2009.

[157] I. Okamoto. Electromagnetic Extraction of Energy from Kerr Black Holes. PASJ, 58:1047–1071, December 2006.

[158] F. Pacini. Energy Emission from a Neutron Star. Nature, 216:567–568, November 1967.

[159] F. Pacini and M. Salvati. On the Evolution of Supernova Remnants. Evolution of the Magnetic Field, Particles, Content, and Luminosity. ApJ, 186:249–266, November 1973.

[160] T. Padmanabhan. Inverse Compton Scattering - Revisited. *Journal of Astrophysics and Astronomy*, 18:87, March 1997.

[161] D. N. Page. Maximal acceleration is non-rotating. *Classical and Quantum Gravity*, 15:1669–1719, June 1998.

[162] G. Pedaletti, S. J. Wagner, and F. M. Rieger. Very High Energy γ-ray Emission from Passive Supermassive Black Holes: Constraints for NGC 1399. ApJ, 738:142, September 2011.

[163] R. Penrose. Gravitational Collapse: the Role of General Relativity. *Nuovo Cimento Rivista Serie*, 1:252, 1969.

[164] J. Pétri. High-energy pulses and phase-resolved spectra by inverse Compton emission in the pulsar striped wind. Application to Geminga. A&A, 503:13–18, August 2009.

[165] J. Pétri. A unified polar cap/striped wind model for pulsed radio and gamma-ray emission in pulsars. MNRAS, 412:1870–1880, April 2011.

[166] E. S. Phinney. Acceleration of a Relativistic Plasma by Radiation Pressure. MNRAS, 198:1109, March 1982.

[167] E. Poisson. TOPICAL REVIEW: Radiation reaction of point particles in curved spacetime. *Classical and Quantum Gravity*, 21:153, August 2004.

[168] O. Porth and C. Fendt. Acceleration and Collimation of Relativistic Magnetohydrodynamic Disk Winds. ApJ, 709:1100–1118, February 2010.

[169] B. Punsly. *Black hole gravitohydromagnetics*. 2001.

[170] B. Punsly and F. V. Coroniti. Relativistic winds from pulsar and black hole magnetospheres. ApJ, 350:518–535, February 1990.

[171] A. B. Pushkarev, Y. Y. Kovalev, M. L. Lister, and T. Savolainen. Jet opening angles and gamma-ray brightness of AGN. A&A, 507:L33–L36, November 2009.

[172] V. Radhakrishnan and D. J. Cooke. Magnetic Poles and the Polarization Structure of Pulsar Radiation. Astrophys. Lett., 3:225, 1969.

[173] M. J. Rees. The Non-Thermal Continuum from the Crab Nebula: the 'Synchro-Compton' Interpretation. In R. D. Davies and F. Graham-Smith, editors, *The Crab Nebula*, volume 46 of *IAU Symposium*, page 407, 1971.

[174] M. J. Rees and J. E. Gunn. The origin of the magnetic field and relativistic particles in the Crab Nebula. MNRAS, 167:1–12, April 1974.

[175] C. S. Reynolds and M. A. Nowak. Fluorescent iron lines as a probe of astrophysical black hole systems. Phys. Rep., 377:389–466, April 2003.

[176] F. M. Rieger and F. Aharonian. Probing the central black hole in M87 with gamma-rays. *ArXiv e-prints*, August 2012.

[177] F. M. Rieger and F. Volpe. Short-term VHE variability in blazars: PKS 2155-304. A&A, 520:A23, September 2010.

[178] F. J. Romeiras. Stability of relativistic transverse cold plasma waves. I - Circularly polarized waves. *Journal of Plasma Physics*, 20:479–501, December 1978.

[179] M. A. Ruderman and P. G. Sutherland. Theory of pulsars - Polar caps, sparks, and coherent microwave radiation. ApJ, 196:51–72, February 1975.

[180] E. T. Scharlemann and R. V. Wagoner. Aligned Rotating Magnetospheres. General Analysis. ApJ, 182:951–960, June 1973.

[181] R. Schödel, T. Ott, R. Genzel, R. Hofmann, M. Lehnert, A. Eckart, N. Mouawad, T. Alexander, M. J. Reid, R. Lenzen, M. Hartung, F. Lacombe, D. Rouan, E. Gendron, G. Rousset, A.-M. Lagrange, W. Brandner, N. Ageorges, C. Lidman, A. F. M. Moorwood, J. Spyromilio, N. Hubin, and K. M. Menten. A star in a 15.2-year orbit around the supermassive black hole at the centre of the Milky Way. Nature, 419:694–696, October 2002.

[182] S. Shibata, J. Miyazaki, and F. Takahara. On the electric field screening by electron-positron pairs in a pulsar magnetosphere. MNRAS, 295:L53–L58, April 1998.

[183] M. Sikora, Ł. Stawarz, and J.-P. Lasota. Radio Loudness of Active Galactic Nuclei: Observational Facts and Theoretical Implications. ApJ, 658:815–828, April 2007.

[184] O. Skjæraasen, A. Melatos, and A. Spitkovsky. Particle-in-Cell Simulations of a Nonlinear Transverse Electromagnetic Wave in a Pulsar Wind Termination Shock. ApJ, 634:542–546, November 2005.

[185] H. Sol, G. Pelletier, and E. Asseo. Two-flow model for extragalactic radio jets. MNRAS, 237:411–429, March 1989.

[186] L. Stawarz. Multifrequency Radiation of Extragalactic Large-Scale Jets. *Chinese Journal of Astronomy and Astrophysics Supplement*, 3:383–403, December 2003.

[187] P. A. Sturrock. A Model of Pulsars. ApJ, 164:529, March 1971.

[188] P. Subramanian, A. Shukla, and P. A. Becker. TeV blazar variability: the firehose instability? MNRAS, 423:1707–1710, June 2012.

[189] G. S. S. Sweeney and P. Stewart. Magneto-parametric instabilities in the Crab nebula. A&A, 41:431–436, July 1975.

[190] G. S. S. Sweeney and P. Stewart. Magneto-parametric instabilities in the Crab Nebula. II. A&A, 66:139–153, May 1978.

[191] P. H. T. Tam, R. H. H. Huang, J. Takata, C. Y. Hui, A. K. H. Kong, and K. S. Cheng. Discovery of GeV γ-ray Emission from PSR B1259-63/LS 2883. ApJ, 736:L10, July 2011.

[192] M. Tavani and J. Arons. Theory of High-Energy Emission from the Pulsar/Be Star System PSR 1259-63. I. Radiation Mechanisms and Interaction Geometry. ApJ, 477:439, March 1997.

[193] M. Tavani, J. Arons, and V. M. Kaspi. Regimes of high-energy shock emission from the Be star/pulsar system PSR 1259-63. ApJ, 433:L37–L40, September 1994.

[194] M. Tavani et al. Discovery of Powerful Gamma-Ray Flares from the Crab Nebula. *Science*.

[195] P. D. Thacker, F. C. Michel, and I. A. Smith. Instability of the Goldreich-Julian Model for a Pulsar Magnetosphere. In R. J. Dufour and S. Torres-Peimbert, editors, *Revista Mexicana de Astronomia y Astrofisica Conference Series*, volume 7 of *Revista Mexicana de Astronomia y Astrofisica Conference Series*, page 211, March 1998.

[196] K. S. Thorne. Disk-Accretion onto a Black Hole. II. Evolution of the Hole. ApJ, 191:507–520, July 1974.

[197] K. S. Thorne, R. H. Price, and D. A. MacDonald. *Black holes: The membrane paradigm*. 1986.

[198] A. N. Timokhin. Time-dependent pair cascades in magnetospheres of neutron stars - I. Dynamics of the polar cap cascade with no particle supply from the neutron star surface. MNRAS, 408:2092–2114, November 2010.

[199] A. N. Timokhin and J. Arons. Current Flow and Pair Creation at Low Altitude in Rotation Powered Pulsars' Force-Free Magnetospheres: Space-Charge Limited Flow. *ArXiv e-prints*, June 2012.

[200] V. V. Usov. Wave zone structure of NP 0532 and infrared radiation excess of Crab Nebula. Ap&SS, 32:375–377, February 1975.

[201] S. Vincent and S. Lebohec. Monte Carlo simulation of electromagnetic cascades in black hole magnetosphere. MNRAS, 409:1183–1194, December 2010.

[202] S. J. Wagner. Multiwavelength properties of Blazars. In F. A. Aharonian and H. J. Völk, editors, *American Institute of Physics Conference Series*, volume 558 of *American Institute of Physics Conference Series*, pages 358–369, April 2001.

[203] R. M. Wald. Black hole in a uniform magnetic field. Phys. Rev. D, 10:1680–1685, September 1974.

[204] R. M. Wald. *General relativity*. 1984.

[205] L. B. F. M. Waters. The density structure of discs around Be stars derived from IRAS observations. A&A, 162:121–139, July 1986.

[206] L. B. F. M. Waters, E. P. J. van den Heuvel, A. R. Taylor, G. M. H. J. Habets, and P. Persi. Evidence for low-velocity winds in Be/X-ray binaries. A&A, 198:200–210, June 1988.

[207] A. S. Wilson and E. J. M. Colbert. The difference between radio-loud and radio-quiet active galaxies. ApJ, 438:62–71, January 1995.

[208] R. X. Xu and G. J. Qiao. Pulsar Braking Index: A Test of Emission Models? ApJ, 561:L85–L88, November 2001.

Acknowledgements

...And the final chapter:). The most difficult one to write, because words are not sufficient to express my gratitude. My thesis wouldn't be possible without many people. THANK YOU!

Dear John, you were a great teacher to learn from, and I cannot thank you enough for those three years! For your close collaboration, your guidance, endless support, advice – not only in strictly scientific problems:). For *always* having time for me. For sharing with me your deep insight and broad knowledge of Physics, for giving me opportunities to widen my horizons beyond the project. For lots of enlightening discussions, and lots of nonscientific conversations. For never complaining about my English. Wholehearted *thank you*.

I would like to warmly thank Prof. Matthias Bartelmann and Prof. Stefan Wagner, for serving on my thesis committee during my studies, and on my final examination committee in the end. Lots and lots of thanks, Matthias, for being the second referee!

I'm also grateful to Prof. Karlheinz Meier, for his kind agreement to be my examiner.

And I couldn't forget to thank Prof. Michał Ostrowski, for his contagious enthusiasm for science and encouragement, whenever we had an occasion to talk.

Lots of thanks to Brian Reville, for help with the English, for encouragement, advice, and friendship. Wiesz, dzięki!

Warm thanks to *all* my friends and colleagues from the Institute. Especially, to: Giovanni (for *how is it going*), Christian (for being my fellow thesis writer, and for *help* with the German abstract), Ioanna (for every-morning coffee, and every-thing else), Ervin (for theoretical-physicists' mutual understanding), Ellen (for explaining me mysteries of bureaucracy), Frank, Marie-Helene, Prof. Kelner (for their unconditional kindness), Gabi Weese (for her friendliness, keeping-all-together, and amazing cakes!), and all my neutino, higgs, and dark-matter-friends, Philipp, Alex×2, Tibor, Martin, Julian, Ker Sham, Juri. It was great to be a part of the MPIK-team.

Lots and lots of warm thanks to Jenni, Dejen, Jessi, Gabriel, Sandhya, Dhatri, Johannes, Vanessa, Natalia – my flatmates and neighbors, who made my last three years so enjoyable and unforgettable. Thanks for sharing not only the apartment, but also everyday life, and weekend chilling out. Vielen dank, multumesc!

Lots of warm thanks I owe also the Polish@EMBL group, for our Friday highlights :), EMBL summer parties, and time spent together. Special thanks to Ola & Laurent, Ania, Jacek, Ewelina.

I couldn't forget about my fellow students from the IMPRS generation, especially Gustavo & Pilar (!), Meiert, Raoul, Ellen & Rene, Jochen, Favi. Many thanks to Christian, for his commitment to IMPRS, help, and organizing IMPRS get-together.

Thanks to my fellow students from Kraków, who also decided to do their PhD abroad: Kasia Rejzner, Tomek Rembiasz, Wojtek Idec. Thanks for the nice time we had together in Germany (and Stockholm:), too.

And, of course, the greatest thanks to my family. My studies wouldn't be possible without the support, belief and encouragement, given by my parents, Jadwiga and Bogusław. I am indebted

for always having a cure for my doubts, and telling me that we can do (almost) everything (tak Mamo, wiem, że tylko jednej rzeczy się nie da:).

Equally much I thank my sister Gosia, for chats which are always a "prozac", for being more than the best friend to always rely on, for discussing Physics, for keeping me thinking.

Specjalne, ogromne podziękowania dla babci Jany i cioci Marysi, za to, że zawsze są ze mną.

Thanks to my dear friends who are in Poland, or abroad, but always there for me, and who still haven't forgotten me, even though I write very little: Mery & Stahó, Natalia, Kasia (with Adam and Małgosia), Jadzia, Michał.

It's thanks to, and for you.